The role of nano- to millimetre sized crystals on the dynamic evolution of shallow silica-rich magma: Implications for volcanic eruptions

Francisco Cáceres Acevedo

München, 2020

The role of nano- to millimetre sized crystals on the dynamic evolution of shallow silica-rich magma: Implications for volcanic eruptions

Francisco Cáceres Acevedo

Dissertation zur Erlangung des
Doktorgrades an der Fakultät für Geowissenschaften
der Ludwig-Maximilians-Universität
München

vorgelegt von
Francisco Cáceres Acevedo
aus Santiago, Chile

München, den 04.03.2020

Erstgutachterin: PD Dr. Bettina Scheu
Zweitgutachter: Prof. Dr. Donald B. Dingwell
Tag der mündlichen Prüfung: 29.07.2020

To my father, who sadly could not see the end of this adventure.

And to my mother, who is simply the strongest woman on Earth.

Zusammenfassung

Vulkanausbrüche zählen zu den größten Bedrohungen für Bevölkerung, Infrastruktur und Wirtschaft auf der Erde. Sie werden durch die Entstehung, die Speicherung und den Transport von Magma zur Oberfläche beeinflusst. Es gibt eine große Bandbreite von Ausbruchstypen, von heftig explosiv bis schwach effusiv. Explosive Ausbrüche können hohe Mengen an Asche in die Atmosphäre abgeben, während effusive Ausbrüche Lavaströme erzeugen. Die damit verbundenen Gefahren können daher je nach Ausbruchstyp variieren.

Die Druckentlastung die Magmen beim Aufstieg in flachere Bereiche der Erdkruste erfahren, führt zur Entgasung und damit zu einem Anstieg der Schmelzviskosität. Außerdem bilden sich Kristallisationskeime und Kristalle beginnen zu wachsen. Das Zusammenspiel aus Entgasungsdynamik und den physikalischen Eigenschaften des Magmas entscheidet über den Stil des Vulkanausbruchs. Ob ein Ausbruch effusiven oder explosiven abläuft, hängt in erster Linie davon ab, ob die entgasten Volatile zur Oberfläche aufsteigen können, oder im aufsteigenden Magma gefangen bleiben. Das Wachstum der Blasen wird durch Diffusion und Gasexpansion im Zuge der Druckentlastung beim Aufstieg gefördert. Die Viskosität des Magmas behindert die Ausdehnung der Blasen. Wenn die Blasen wachsen, kann dies den Aufstieg des Magmas zur Oberfläche beschleunigen und dadurch erheblichen Überdruck in den Blasen aufbauen. Dieser Überdruck kann zur Fragmentation des Magmas führen. Im Gegensatz dazu können sich die Blasen verbinden und ein Netzwerk bilden. Dadurch wird die Entgasung erleichtert, der Gasüberdruck wird verringert und der Aufstieg des Magmas verlangsamt. Es ist bekannt, dass sowohl Phäno- als auch Mikrokristalle eine heterogene Blasenentstehung fördern und somit den Entgasungsvorgang erleichtern. Der Einfluss von Nanokristallen auf die Entgasung ist bis jetzt unerforscht.

Die physikalischen Eigenschaften eines Magmas werden hauptsächlich durch die chemische Struktur der silikatischen Schmelzkomponente und dem Vorhandensein von festen Phasen gesteuert. Die daraus resultierende Viskosität des Magmas ist ein Hauptfaktor, der bestimmt, ob es zu einem effusiven oder explosiven Ausbruch kommt. Die Viskosität beeinflusst, ob Blasen aus gelösten Volatilen im Magma verbleiben oder aufsteigen, und ob sich Blasen weiter ausdehnen können. Die Magma-Viskosität hängt von der Viskosität der silikatischen Schmelzphase und der Menge an Kristallen ab. Die Viskosität der Schmelze wird beispielsweise stark vom Wassergehalt, dem Eisengehalt und dem Oxidationszustand beeinflusst. Kristallwachstum erhöht die Partikelfracht in der Schmelze und führt zu einer

Erhöhung der Viskosität. Die Auswirkungen der Nano-Kristallisation auf die Magmen-Rheologie wurden bisher allerdings nur oberflächlich untersucht.

Silikatreiche Magmen werden normalerweise flach in der Erdkruste gespeichert. Sie sind in der Lage hochexplosive Eruptionen hervorzubringen, die in der Regel mit Lavaströmen und dem Wachstum von Lavadomen einhergehen. Diese Magmen sind gewöhnlich hochviskos mit einem hohen Wasseranteil und haben somit das Potenzial explosiv auszubrechen. Andere Studien haben gezeigt, dass flache (~2 km tiefe) rhyolitische Magmareservoirs eine potentielle Gefahr darstellen können. Die Bedingungen, die notwendig sind, um aus diesen Magmen entweder einen explosiven oder effusiven Ausbruch zu erzeugen, sind jedoch nach wie vor unklar.

In dieser Arbeit habe ich mehrere Experimente durchgeführt, um (1) den Einfluss von Nanokristallen auf Nukleation und Wachstum von Gasblasen zu testen, (2) den Einfluss von Abkühlung auf die Fe-Ti-Oxid-Nanokristallbildung und die Struktur der silikatischen Schmelze zu untersuchen, (3) die Rolle von Kristallart und Größe bei der Entgasung von flachen rhyolitischen Magmen zu beleuchten und (4) die Blasenbildung und Fragmentation bei langsamer Druckentlastung in flachen rhyolitischen Magmen zu analysieren.

Zunächst habe ich Experimente zur Blasenbildung in einem optischen Dilatometer durchgeführt, dabei habe ich rhyolitische Magmen mit und ohne Nanokristalle verwendet. Ich habe herausgefunden, dass Nanokristalle die Menge an Blasen und deren Expansionsraten in einem entgasenden sauren Magma erhöhen können. Außerdem habe ich mir die Blasenanzahl in natürlichen Proben von explosiven Ausbrüchen angeschaut. Hier lässt sich der selbe Zusammenhang erkennen: Eine hohe Anzahl an Blasen und das Vorkommen von magmatischen Nanokristallen. Desweiteren habe ich ein mathematisches Magma-Aufstiegsmodells genutzt um zu zeigen, dass das Vorhandensein von Nanokristallen die Blasenanzahl in einer Weise beeinflussen kann, dass es zu einem explosiven Ausbruch kommen kann, obwohl die gewählten Rahmenbedingungen ohne Nanokristalle zu einem effusiven Ausbruch führen würden.

Im nächsten Teil meiner Arbeite habe ich untersucht wie sich die Struktur einer Schmelze verändert, wenn in einem kristallfreien Magma das Wachstum von Nanokristallen einsetzt. Dazu wurden Abkühlungsexperimente mit kontrollierten Abkühlraten in einem optischen Dilatometer durchgeführt. Die Ergebnisse zeigen, dass die Bildung von Nanokristallen mit einer Zunahme der Schmelzpolymerisation einhergeht. Diese Experimente unter oxidierenden Bedingungen und langsamer Abkühlungsraten geben einen Einblick in die Bildung von Fe-Ti-Oxid-Nanokristallen sowie in die strukturelle Veränderungen von

silikatischen Schmelzen, die in dieser Form auch in den entsprechenden natürlichen vulkanischen Systemen vorkommen. Außerdem wurde gezeigt, dass sowohl der höhere Grad der Schmelzpolymerisation als auch die höhere Kristallfracht aufgrund der Bildung von Nanokristallen zu einer Erhöhung der Viskosität in Fe-reichen Rhyoliten führt. Zusammen mit der daraus resultierenden hohen Blasenanzahl und deren hohen Wachstumsraten, haben Nanokristalle das Potenzial, flache entgasende Magmen von einem effusiven in ein explosives Ausbruchsregime zu verlagern.

Im dritten Teil meiner Arbeit habe ich Experimente durchgeführt, bei denen die Blasenbildung durch Aufheizen der Probe herbeigeführt wurde. Dazu habe ich wasserarme und blasenfreie natürliche Rhyolitproben genutzt. Die Ergebnisse zeigen, dass die Kristallanzahl von Mikrokristallen, besonders bei Fe-Ti-Oxiden, einen starken Einfluss auf die Blasenanzahl hat. Im Gegensatz dazu, haben Phänokristalle oder andere mikrokristalline Mineralphasen einen geringeren Einfluss auf die heterogene Blasen-Keimbildung. In niedrigkristallinen Magmen wird die Koaleszenz und Konnektivität der Blasen durch Phänokristalle stärker und früher beeinflusst als durch Mikrokristalle. Proben mit Phänokristallen haben eine deutlich höhere Blasenkoaleszenz und Blasenkonnektivität ausgebildet als phänokristallfreie rhyolitische Magmen. Die Ergebnisse, die ich in dieser Arbeit vorstelle, helfen ein Verständnis zu entwickeln, welche Rolle die vorhandenen Kristallphasen vor und während dem Ausbruch bei der Entgasung des aufsteigenden Magmas spielen.

Im letzten Teil ermögliche ich einen ersten Einblick in die Blasenentstehung in flachen rhyolitischen Magmen. Die Besonderheit daran, sind die langsamen Dekompressionsraten. Diese Bedingungen habe ich experimentell nachgestellt, indem eine rehydrierte rhyolitische Schmelze in einem unter Gasüberdruck stehendem heißen Autoklaven einer langsamen Druckentlastung ausgesetzt wurde. Zum ersten Mal wurde dabei gezeigt, dass es auch bei langsamen Dekompressionsraten zu einer magmatischen Fragmentation kommen kann. Dekompressionsraten stehen in direktem Zusammenhang zur Ungleichgewichtsentgasung, die wiederum eine Fragmentation begünstigt. Die Ergebnisse zeigen auch, dass die Wasseranteile und Temperaturen, die in natürlichen, flachen und sauren Magmen zu erwarten sind, beim Aufstieg zur Oberfläche zu einem starken Blasenwachstum führen können. Außerdem wurden während dem Blasenwachstum eine gleichzeitige Zunahme der Nanokristallbildung beobachtet. Das hat wiederum Einfluss auf die Magma-Viskosität und damit auch auf die Fragmentation. Diese Ergebnisse geben einen Einblick in das Potential für explosive Ausbrüche von flachen rhyolitischen Magmen, wie beispielsweise im Vulkanfeld Laguna del Maule in Chile und am Vulkan Krafla in Island.

Abstract

Volcanic eruptions pose some of the greatest threats to population, infrastructure and economies in the Earth system. They are modulated by the generation, storage and transport of magma towards the surface. Eruptions span a highly variable range of styles from violent explosions and the generation of volcanic ash, to the relatively quiescent effusion of lava, also ranging a great diversity of hazards related.

Magmas ascending to shallow levels are subjected to decompression that leads to volatile loss and melt viscosity increase, as well as the nucleation and growth of crystals. Then, the degassing dynamics of a magma and its physical properties exert a crucial control on the eruptive style of a volcano. Whether an eruption will develop in an effusive or explosive eruptive style depends dominantly on whether exsolved volatiles will efficiently escape or remain trapped in the ascending magma respectively. Bubbles of exsolved volatiles can nucleate and grow isolated via volatile diffusion and gas expansion caused by ascent-driven decompression, limited by the viscous resistance of the hosting material. This expansion may accelerate the magma towards the surface and build-up significant gas overpressure that can result in magma fragmentation. On the other hand, bubbles may coalesce and form connected porous networks that promote gas escape to the exterior, reducing gas overpressure and slowing magma ascent. Both phenocrysts and microlites are known to cause heterogeneous bubble nucleation and to facilitate bubble coalescence in degassing magmas. Yet the influence of nanolites on bubble-hosted degassing processes remains wholly uninvestigated.

The physical properties of a magma are mainly controlled by the chemical structure of its silicate melt phase and the physical presence of suspended phases. Of these, it is magma viscosity which is often a dominant factor determining whether a magma will erupt effusively or explosively. Viscosity determines, for instance, whether bubbles of exsolved volatiles will remain coupled or decoupled in the magma and their expansion, affecting the degassing dynamics. Magma viscosity depends on the viscosity of the silicate melt phase, as well as the crystal load. The viscosity of the melt, for instance, greatly depends on its water concentration, iron content and oxidation state, while magma crystallisation increases viscosity by increasing the load of suspended phases and generating changes in the chemical structure of the melt. Yet the effects of nanolite crystallisation on magma rheology have only been investigated to day in a reconnaissance manner.

Silica-rich magmas are commonly stored at shallow levels. They have produced highly explosive eruptions that are usually accompanied with effusion of lava flows and domes. These magmas are commonly highly viscous and contain enough water concentration to produce explosivity. Studies have found rhyolitic magma reservoirs stored as shallow as ~2 km depth that may pose potential hazards. However, the conditions necessary in order to generate either an explosive or effusive eruption from these magmas remains unclear.

In this thesis, I conducted several experimental approaches in order to (1) test the influence of nanolites on gas bubble nucleation and growth dynamics, (2) better constrain the influence of cooling on Fe-Ti oxide nanolite crystallisation and silicate melt structure, (3) shed light on the role of the nature and size of crystals on degassing of shallow rhyolitic magma, and (4) explore vesiculation and fragmentation occurring in shallow rhyolitic magma due to slow decompression.

First, I conducted vesiculation experiments in an optical dilatometer using both a nanolite-bearing and a nanolite-free rhyolitic magma. I documented how nanolites can increase the bubble number density and expansion rate in a degassing silicic magma. Then, I inspected a compilation of bubble number densities from natural volcanic rocks from explosive eruptions and inferred that some very high naturally-occurring bubble number densities could be associated with the presence of magmatic nanolites. Finally, applying a numerical magma ascent model I show that for reasonable starting conditions for silicic eruptions, an increase in the resulting bubble number density associated with nanolites could push an eruption that would otherwise be effusive into the conditions required for explosive behaviour.

Secondly, I investigated the melt structural changes during the transition from a crystal-free melt to a nanolite-bearing magma, as well as the process of nanolite crystallisation. This was done performing magma cooling experiments at highly controlled rates in an optical dilatometer. The results show that nanolites start forming concomitant with an increase in melt polymerisation. These experiments at oxidising conditions and slow cooling rate provide insights into the formation of Fe-Ti oxide nanolites and structural changes of silicate melts that can also be observed and are expected in equivalent natural volcanic systems. I showed that both the higher degree of melt polymerisation and the higher load of crystals due to the formation of nanolites in Fe-rich rhyolites are likely to cause increases in the magma viscosity. Taken together with the resultant high bubble number density and growth rate that nanolites may promote in degassing magmas, these effects may have the potential to shift shallow magmas from an effusive eruption style into conditions favourable for an explosive eruption.

Third, I performed heating induced vesiculation experiments in a multiphase, low-water concentration and bubble-free natural rhyolite. The results indicate that crystal number density of microlites, specifically Fe-Ti oxides, exerts a dominant control on the bubble number density while the role of phenocrysts or other microlite mineral phases on heterogeneous nucleation are more limited. On the other hand, phenocrysts enhance bubble coalescence and connectivity more and earlier than microlites in low-crystalline magmas. When compared to bubble textures produced in a phenocryst-free rhyolitic magma, the magma with phenocrysts noticeably produced greater bubble coalescence and connectivity. These findings help to better understand the role that pre- and syn-eruptive crystalline phases may play in the degassing process during magma ascent towards the surface.

Finally, I give first insights into the vesiculation process of shallow rhyolitic magma subjected to slow decompression. I conducted slow decompression experiments using a gas-pressurised hot autoclave and a re-hydrated rhyolitic melt. The results show for the first time that magmatic fragmentation can be achieved in silicate melt by decompression-induced vesiculation at slow decompression rates. Within this context, disequilibrium degassing plays an important role promoting fragmentation, which is directly related to the decompression rate. The results also indicate that for initial water concentrations and temperatures expected in natural shallow silica-rich magmas, continuous decompression until atmospheric pressure can result in high degrees of magma vesiculation. Finally, during vesiculation, a concomitant increase of nanolite crystallisation was observed, with potential implications for magma viscosity and fragmentation. These results give insight into the potential explosivity of shallow rhyolitic magmas such as those found at Laguna del Maule volcanic field in Chile and Krafla volcano in Iceland.

Resumen

Las erupciones volcánicas representan algunas de las mayores amenazas para la población, infraestructura y economías en el planeta. Están conducidas por la generación, almacenamiento, y transporte de magma hacia la superficie. Los estilos eruptivos abarcan un amplio rango desde erupciones explosivas violentas, que incluyen la generación de ceniza, hasta la efusión más calmada de lava, y tienen una gran diversidad de riesgos asociados.

Magmas que ascienden a niveles someros están sometidos a descompresión que lleva a las Perdida de volátiles y un consecuente aumento en la viscosidad, así como también la nucleación y crecimiento de cristales. Así es como la dinámica de desgasificación del magma, junto con sus propiedades físicas ejercen un control crucial en el estilo eruptivo de un volcán. Si es que una erupción de va a desarrollar de manera efusiva o explosiva depende dominantemente de si los volátiles exsueltos escapan eficientemente del magma o permanecen atrapados en el respectivamente. Las burbujas de volátiles exsueltos pueden nuclear y crecer aisladamente vía difusión de volátiles y por la expansión del gas en ellas causada por la descompresión producida durante el ascenso de magma y a la vez están limitadas por la resistencia ejercida por el magma que las rodea. Esta expansión puede acelerar el magma hacia la superficie y producir una gran sobrepresión en las burbujas que puede resultar en la fragmentación del magma. Por otro lado, las burbujas pueden coalescer y formar una red de poros conectados que permiten el escape de volátiles al exterior, lo que reduce la sobrepresión del gas en las burbujas y ralentiza el ascenso de magma. Tanto los fenocristales como los microlitos causan nucleación heterogénea de burbujas y facilitan la coalescencia de ellas en magmas que se desgasifican. Pero aún hay falta de investigación respecto a la influencia de los nanolitos en procesos que envuelven burbujas en la desgasificación.

Las propiedades físicas de un magma están controladas principalmente por la estructura química de su fase fundida y por la presencia física de fases suspendidas. Entre estas, la viscosidad del magma es la que comúnmente determina si una erupción será efusiva o explosiva. La viscosidad determina, por ejemplo, si es que las burbujas de volátiles exsueltos permanecerán acopladas o desacopladas de él, como también la expansión que pueden alcanzar, lo que afecta la dinámica de desgasificación del magma. La viscosidad total del magma depende de la viscosidad de su fase fundida y de la carga de cristales que contenga. La viscosidad de la fase fundida, por otra parte, depende principalmente de su concentración de agua disuelta, el contenido de hierro y el estado de oxidación, mientras que la cristalización

incrementa la su viscosidad generando cambios en la estructura química. Aún, los efectos en la reología del magma producidos por la cristalización de nanolitos has sido sólo reconocidos, pero no ha sido ampliamente estudiados hasta ahora.

Los magmas ricos en sílice están almacenados comúnmente en niveles someros de la corteza. Ellos han producido erupciones altamente explosivas que están acompañadas usualmente por la efusión de lavas o domos. Estos magmas suelen ser muy viscosos y contienen la suficiente cantidad de agua disuelta como para generar explosividad. Algunos estudios han encontrado reservorios de magma riolítico almacenados a niveles tan someros como ~2 km de profundidad, los que podrían tener altos riesgos asociados. Sin embargo, las condiciones necesarias para generar una erupción tanto efusiva como explosiva a partir de estos magmas no están claras.

En esta tesis, conduje varias aproximaciones experimentales para (1) testear la influencia de nanolitos en la dinámica de nucleación y crecimiento de burbujas, (2) determinar de mejor manera la influencia de enfriamiento en la cristalización de nanolitos de óxidos de hierro y titanio, (3) generar luces acerca de los roles del tipo y tamaño de cristales en la desgasificación de magmas riolíticos someros y (4) explorar la vesiculación y fragmentación explore que podría ocurrir en magmas riolíticos someros sometidos a descompresión.

Primero, conduje experimentos de vesiculación en un dilatómetro óptico usando magmas riolíticos tanto libres como conteniendo nanolitos. Documenté como los nanolitos pueden incrementar la densidad de burbujas en el magma y su tasa de expansión. Luego, inspeccioné una compilación de densidades de burbujas en rocas volcánicas de erupciones explosivas e inferí que algunos de los valores más altos que se pueden encontrar en la naturaleza podrían estar asociados a la presencia de nanolitos que no fueron previamente reconocidos en aquellas rocas. Finalmente, apliqué un modelo numérico de ascenso de magma donde maestro que para condiciones razonables para magma riolíticos, el incremento en la densidad de burbujas relacionados a la presencia de nanolitos podría mover una erupción que en principio sería efusiva hacia condiciones necesarias para generar un comportamiento explosivo.

Luego, investigué los cambios en la estructura de la fase fundida durante la transición desde un fundido libre de cristales hacia un magma que los contiene, junto con el proceso de cristalización mismo. Esto lo hice a través de experimentos de enfriamiento de magma a tasas altamente controladas en un dilatómetro óptico. Los resultados muestran que los nanolitos empiezan a formarse en conjunto con un aumento en la polimerización de la fase fundida. Estos experimentos, conducidos en condiciones oxidantes y a tasas de enfriamiento lentas, proveen de ideas acerca de la formación de nanolitos de óxidos de hierro y titanio y cambios

estructurales en la fase fundida que pueden ser esperados en sistemas volcánicos en condiciones equivalentes. Muestro que tanto el grado de polimerización del magma y la mayor concentración de cristales debido a la formación de nanolitos son probables que causen un aumento en la viscosidad toal del magma. En conjunto con la alta densidad de burbujas que producen y la alta tasa de expansión de magma resultante, los nanolitos pueden mover magmas someros desde una eventual erupción efusiva hacia condiciones favorables para generar una erupción explosiva

Tercero, conduje experimentos de vesiculación en un magma riolítico con múltiples fases cristalinas, inicialmente libre de burbujas y con una concentración de agua disuelta muy baja. Los resultados indican que la densidad de microlitos, específicamente de óxidos de hierro y titanio, ejercen un control dominante sobre la densidad de burbujas. Mientras tanto, el rol de los fenocristales o microlitos de otras fases minerales generando nucleación heterogénea es más limitado. Por otro lado, los fenocristales favorecen en mayor medida y más tempranamente que los microlitos la coalescencia de burbujas y su conectividad. Esto, al menos en magmas con baja cristalinidad. Comparando las texturas producidas en un magma libre de fenocristales, el magma que los contiene produce notablemente mayor coalescencia de burbujas y conectividad. Estos resultados ayudan a entender mejor los roles de fases cristalinas pre- y syn-eruptivas en cuanto a los procesos de desgasificación durante el ascenso de magma hacia la superficie.

Finalmente, doy primeras ideas acerca del proceso de vesiculación de magmas riolíticos someros que son sometidos a descompresión lenta. Conduje experimentos de descompresión lenta usando un magma riolítico rehidratado y un autoclave a alta temperatura presurizado internamente con gas. Los resultados muestran por primera vez que la fragmentación magmática puede ser alcanzada en magmas silicatados por vesiculación producida durante descompresión a tasas lentas. En este contexto, la desgasificación en desequilibrio, que está ligada a la tasa de descompresión, juega un rol importante favoreciendo la fragmentación. Estos resultados indican, que para una temperatura y concentración de agua esperable para magmas riolíticos someros, la descompresión continua hasta presión atmosférica puede resultar en altos grados de vesiculación magmática. Finalmente, durante la vesiculación, se observó un incremento en la cristalización de nanolitos, que podría tener implicancias en la viscosidad y fragmentación magmática. Estos resultados dan luces acerca del potencial explosivo de magmas riolíticos someros como los encontrados en el campo volcánico Laguna del Maule en Chile y el volcán Krafla en Islandia.

Acknowledgments

I wish to thank here to all the people that directly or indirectly contributed to make this thesis possible:

Firstly, thanks to you Betty for this opportunity and for introducing me into the world of experimental volcanology and work with magmas. Thanks for guiding me through my PhD with great ideas and your availability in this period, and also making the work environment a nice place. Thanks Don for the opportunity to work on my PhD in this great group, for being available when needed, for your very useful comments on my work and for supporting my ideas. Thanks Fabian for all the exciting and insightful discussions and ideas that came during this time and for your all your contribution to this work. Thanks a lot to you Mathieu for being a good friend and for all the help and discussions we had working together. Thanks to my office mates for making this time great, thanks Markus and also Christina for helping me deal with the German language. I also want to thank for all the help during this time to Corrado, Ulli, Kai and Melanie at LMU. Additionally, thanks to Claudio at ETH for the sample preparation.

I want to thank the great friends and group of people that for a long or short period of time, made of this place feel close to home. Thanks Valeria, Mathieu, Joan, Damien, Michaela, Basti, Jérémie, Ana, Leticia, Joali, Janina, Julia, Cristian, Stephanie, Markus, Caron, Nicola, Taylor, Lena, Sönke, Siddarth, Pablo, Anush, Kai, Iphi, Stephi, Diana, Christina, Adrian, Arianna, Dirk, Tim, Rike, Margot, Andre, Marco, Alejandra, Diego, Vero, Ludmila, Shanjie, Mar, Michael, Joanna, Zeynep, Mila, Lukas and if you were part of this and I didn't mention, I am sorry and please feel included.

Quisiera agradecer especialmente a mi madre Elga por ser esa persona genial y fuerte, por todo el apoyo que me brindó al momento de venir acá y que me ha dado hasta ahora, lo que me ha hecho sentir en casa incluso estando tan lejos. Muchas gracias por todo mamá. Lo mismo para mi hermano Claudio de quien el apoyo constante se ha convertido en una pieza esencial para mantener la motivación de seguir en esto. También por la misma razón a la Sole y la Leo. Gracias familia.

And finally, thanks to you Sandra for being a great partner and for all your support, especially in this last period.

Muchas gracias!

Preamble

Part of the content of this thesis is in review state, has been published or is in preparation for being submitted to a peer-reviewed scientific journal.

References relevant for this thesis are listed below and where a co-authored publication is used, only my contribution is reproduced herein. Modifications may have been applied that served for format and consistency of the overall thesis design.

Cáceres, F., Wadsworth, F.B., Scheu, B., Colombier, M., Madonna, C., Cimarelli, C., Hess, K-U., Kaliwoda, M., Ruthensteiner, B. and Dingwell, D.B. 2020. Can nanolites enhance eruption explosivity? Geology 48. doi: 10.1130/G47317.1

Cáceres, F., Scheu, B., Hess, K-U., Cimarelli, C., Vasseur, J., Kaliwoda, M. and Dingwell, D.B. From melt to crystals: The effects of cooling on Fe-Ti oxide nanolites crystallisation and melt polymerisation at oxidising conditions. *In review* in Chemical Geology.

Colombier, M., Wadsworth, F.B., Scheu, B., Vasseur, J., Dobson, K.J., **Cáceres, F.**, Allabar, A., Marone, F., Schlepütz, C. and Dingwell, D.B. 2020. In situ observation of the percolation threshold in multiphase magma. Bulletin of Volcanology 82:32. doi: 10.1007/s00445-020-1370-1

Wadsworth, F.B., Unwin, H.E., Vasseur, J., Kennedy, B.M., Holzmueller, J., Witcher, T., Adolf, J., **Cáceres, F.**, Casas, A.S., Cigala, V., Clement, A.M., Colombier, M., Cronin, S., Cronin, M., Dingwell, D.B., Freitas Guimarães, L., Höltgen, L., Kueppers, U., Seropian, G., Stern, S., Teissier, A., Vossen, C.E.J. and Weichselgartner, N. 2018. Trashcano: Developing a quantitative teaching tool to understand ballistics accelerated by explosive volcanic eruptions. Volcanica, 1 (2), 107-126. doi: 10.30909/vol.01.02.107126

Contents

Zusammenfassung ..... **iii**
Abstract ..... **vii**
Resumen ..... **xi**
Acknowledgments ..... **xv**
Preamble ..... **xvii**
1. Introduction **1**
2. Theoretical background **5**
2.1 Degassing of high-silica magma **5**
2.1.1 Volatile exsolution and bubble growth 5
2.1.2 Bubble nucleation 7
2.1.3 The role of crystals in degassing of magma 7
2.1.4 Outgassing 9
2.2 Nanolites in natural and experimental products **10**
2.2.1 Melt properties and nanolite formation 10
2.2.2 Identification of nanolites and changes in silicate melt 11
2.3 Magmatic fragmentation in silica-rich magma **13**
2.4 Shallow rhyolitic magmas **15**
2.4.1 Laguna del Maule Volcanic Field in Chile 16
2.4.2 Krafla volcano in Iceland 17
3. Materials and methods **19**
3.1 Experimental materials **19**
3.1.1 Natural obsidian 19
3.1.2 Natural vitrophyric rhyolite 20
3.1.3 Synthese Kb2 and Kb4 20
3.1.4 Synthesis Kb8 23
3.2 Pre-experimental sample preparation and analyses **24**
3.2.1 Drilling 24
3.2.2 Cutting 25
3.2.3 Mounting 25
3.2.4 Scanning electron microscope 25

3.2.5 Simultaneous Thermal Analysis 26
3.2.6 Raman spectroscopy 26
3.2.7 Water concentration of the materials 27
3.2.8 Electron microprobe analyses 28
3.2.9 Magnetic hysteresis 28
3.3 Experimental methods **29**
3.3.1 The optical dilatometer 29
3.3.2 The decompression autoclave 32
3.4 Post-experimental sample preparation and analyses **34**
3.4.1 Vesiculation in the optical dilatometer 34
3.4.2 Magma cooling in the optical dilatometer 35
3.4.3 Vesiculation and fragmentation in the decompression autoclave 35
3.4.4 X-ray Computed Tomography (CT) 36
4. The effect of nanolites on magma degassing and implications for eruption explosivity 37
Chapter Summary **37**
4.1 Samples used and experimental conditions **38**
4.2 Bubbles textures, number densities and groundmass characteristics **38**
4.3 Bubble growth rates **42**
4.4 Bubble number densities and nanolites in natural products **43**
4.5 Application to high-silica magmas: Effusive or explosive eruptive style? **46**
4.6 Concluding remarks **48**
5. Conditions for Fe-Ti oxide nanolites crystallisation during cooling of shallow rhyolitic magma 49
Chapter Summary **49**
5.1 Samples used and experimental conditions **50**
5.2 Experimental results **51**
5.2.1 Raman spectra 51
5.2.2 Scanning electron microscope imaging 54
5.2.3 Simultaneous thermal analyses 55
5.3 Discussion **56**
5.3.1 Conditions and timescales for nanolites crystallisation 58
5.3.2 The effect of cooling rate on melt structure and viscosity 61
5.3.3 Implications for natural volcanic systems 66
5.4 Concluding remarks **67**
6. The coupled effect of microlites and phenocrysts on bubble nucleation, coalescence and outgassing: Insights from degassing of low-water rhyolitic magma 69

Chapter Summary ... **69**
6.1 Samples used and experimental conditions ... **70**
6.2 Results ... **71**
6.3 Discussion ... **74**
6.3.1 Bubble nucleation on Fe-Ti oxide microlites ... 74
6.3.2 Coalescence and outgassing enhanced by phenocryst phases ... 76
6.3.3 Influence of viscosity ... 79
6.3.4 Implications for silicica-rich magma reservoirs ... 80
6.4 Concluding remarks ... **81**
7. First insights into slow decompression scenarios for shallow rhyolitic magma ... 83
Chapter Summary ... **83**
7.1 Samples used and experimental conditions ... **84**
7.2 Results ... **86**
7.3 Discussion ... **90**
7.3.1 Equilibrium and disequilibrium degassing ... 90
7.3.2 Bubble number densities ... 93
7.3.3 Bubble nucleation mechanism ... 94
7.3.4 The role of crystals ... 95
7.3.5 Implications for shallow silica-rich magmas ... 95
7.4 Concluding remarks ... **96**
8. Conclusions and outlook ... 97
8.1 Implications for volcanic eruptions ... 99
8.2 Outlook ... 100
Bibliography ... 103

List of figures

Figure 2.1. Bubble growth scheme. 6

Figure 2.2. Crystalline phase and contact angle relationship for heterogeneous nucleation 8

Figure 2.3. Laguna del Maule identified magma reservoir. 16

Figure 2.4. Location of and finding of IDDP-1 well in Krafla, Iceland 18

Figure 3.1. Scanning electron images of the pre-experimental materials 21

Figure 3.2. Particle size analysis of the pre-synthese powder 22

Figure 3.3. Magnetic hysteresis analyses 22

Figure 3.4. Optical dilatometer 30

Figure 3.5. Porosity comparison between optical dilatometer and computed tomography 31

Figure 3.6. Decompression autoclave apparatus 33

Figure 4.1. Real time vesiculation profiles 39

Figure 4.2. Comparison between pre- and post-experimental samples 40

Figure 4.3. Water solubility curve for rhyolitic magmas at 1 atm 41

Figure 4.4. Real time porosity evolution for nanolite-free and nanolite-bearing samples 42

Figure 4.5. Bubble number density of natural volcanic products 44

Figure 4.6. Sample from Kilian volcano (U1) with high Nb 45

Figure 4.7. One-dimensional magma ascent model 47

Figure 4.8. Gas volume fraction and bubble size evolution for a rhyolitic magma 48

Figure 5.1. Raman spectra for experimental samples 52

Figure 5.2. Backscattered electron image (BSE-SEM) of selected samples 54

Figure 5.3. Simultaneous thermal analysis of the experimental material 56

Figure 5.4. Raman spectra of the high wavenumber (HW) region 53

Figure 5.5. BSE- and chemical EDS-SEM images 55

Figure 5.6. Water solubility and magma viscosity 57

Figure 5.7. Raman spectra in the region between 650-700 cm^{-1} 59
Figure 5.8. Temperature and viscosity paths during cooling 61
Figure 5.9. Intensity and area ratios between peak band and region at each cooling rate..... 62
Figure 5.10. Deconvolution of the Raman spectra in the high wavenumber region 1. 63
Figure 5.11. Deconvolution of the Raman spectra in the high wavenumber region 2 64
Figure 5.12. Low and high wavenumber vs 670-690 cm^{-1} and 965-980 cm^{-1} ratio..... 65

Figure 6.1. Comparison between Krafla obsidian and LdM vitrophyric rhyolite. 71
Figure 6.2. X-ray computed tomography image of both types of materials..... 72
Figure 6.3. Porosity versus time for the LdM vitrophyric rhyolite. 73
Figure 6.4. Maximum and final porosities for the vitrophiric rhyolite..... 73
Figure 6.5. Tomography images of Fe-Ti oxides microlites and bubbles..... 75
Figure 6.6. Phenocryst-coalescence relationship..... 77
Figure 6.7. Gas escape from bubbles at the border of the samples. 78
Figure 6.8. Porosity versus bubble diameter calculated for a given bubble number density . 79

Figure 7.1. Pressure and temperature profiles in decompression experiments 85
Figure 7.2. Pre-experimental sample and different post-experimental samples..... 86
Figure 7.3. Post-experimental SEM images of samples decompressed until 1 bar..... 87
Figure 7.4. SEM images of samples decompressed until intermediate pressures 87
Figure 7.5. Porosity and bubble number density of decompressed samples. 89
Figure 7.6. Raman spectra and SEM images for pre- and post-experimental samples 89
Figure 7.7. Water solubility and melt viscosity for a rhyolitic composition..... 91
Figure 7.8. Exsolved water and its equilibrium porosity calculated for Kb8 sample..... 92
Figure 7.9. Porosities obtained for the difference experimental conditions..... 93

List of tables

Table 3.1. Chemical composition of glass for the natural and synthesised samples 23

Table 3.2. Glass transition temperature and water concentration..... 26

Table 4. 1. Bubble number densities for experimental conditions. 41

Table 5.1. Run experiments and nanolites detection according to different methods. 53

Table 5.2. Raman spectra parameters..... 65

Table 6.1. Final and maximum porosities for the LdM vitrophyric rhyolite experiments. 72

Table 7.1. Data for decompression experiments. 88

1

Introduction

Volcanic eruptions pose some of the greatest threats to population, infrastructure and economies in the Earth system (e.g. Cashman and Sparks 2013). The stages of generation in the Earth's interior, storage at intermediate levels and transport towards the surface of magma, represent the linchpin of every volcanic structure. In the upper part of this arrangement, the magma, a multiphase compound of silicate melt with suspended crystals and bubbles of exsolved volatiles, can experience phase changes that represent the starting and driving phenomena of every volcanic eruption.

Magmas that are stored in a reservoir may or not contain already bubbles of pre-eruptive exsolved volatiles (Wallace et al., 1995). These magmas can become supersaturated during ascent driven by decompression (Sparks 1978), heating (Lavallée et al., 2015) or chemical changes resulting from crystallisation (e.g. Zhang et al., 2007). The supersaturation causes bubbles to nucleate at an exsolution depth and to grow while magma continues rising towards the Earth's surface, causing the magma to accelerate and eventually producing a volcanic eruption (e.g. Gonnermann and Manga 2007). These volatile exsolution effects become more complex when the third phase is involved: the crystals. Crystals play several complex roles in the ascending magma that range from changing parameters such as the viscosity (e.g. Costa 2005), facilitating volatile exsolution through bubble formation (e.g. Shea 2017), to even promote gas escape (e.g. Lindoo et al., 2017; deGraffenried et al. 2019; Colombier et al., 2020). The crystal cargo of the magma is generally believed to play a central role influencing degassing processes. Both mm-scale phenocrysts and micron-scale microlites are known to cause heterogeneous bubble nucleation and to facilitate bubble coalescence, but nanometer-scale crystalline phases, so-called "nanolites", are a yet underreported phenomena in erupting magma. They have been just hypothesised as a potential control on the eruptive style of

volcanoes (Mujin and Nakamura 2014; Mujin et al., 2017; Di Genova et al., 2017) and suggested as a factor that may favour heterogeneous bubble nucleation (Shea 2017). Yet the influence of nanolites on bubble nucleation and growth, as well as the conditions at which these nanolites form and the possible consequences for the eruptive style of volcanoes remains wholly uninvestigated. Furthermore, no study has been carried out so far showing the coupled effect and interplay between natural microlites and phenocrysts in a degassing rhyolitic magma.

Eruptions span a highly variable range of styles from violent explosions and the generation of volcanic ash, to the relatively quiescent effusion of lava. The effusive (e.g. lava flows or domes) or explosive (e.g. Hawaiian, Strombolian, Vulcanian, sub- to Plinian) behaviour of volcanic activity is responsible for a wide variability in the associated hazards (e.g. Aspinall and Blong, 2015). Whether and eruption will develop in an effusive or explosive eruptive style depends dominantly on whether volatiles will escape or remain trapped in an ascending magma (e.g. Eichelberger et al., 1986). This is how degassing dynamics play a crucial role in controlling the explosivity of magma at erupting volcanoes.

Silica-rich magma have produced some of the largest explosive eruptions in historical times (e.g. Sparks et al., 1981; Self and Rampino, 1981; Williams and Self, 1983; Carey and Sigurdsson, 1985;1989 Fierstein and Hildreth, 1992; Alfano et al., 2011; Castro et al., 2013; Bonadonna et al., 2015). These magmas are often stored at shallow levels in the crust as a final pre-eruptive step (Cashman and Sparks, 2013). Furthermore, rhyolitic magma reservoirs have been found in shallow levels of a few kilometres in the crust, either by geophysical evidences (Laguna del Maule Volcanic Field in Chile; Feigl et al., 2014; Le Mével et al., 2016; Miller et al., 2017; Cordell et al., 2018; Wespestad et al., 2019) or direct contact with their magma by intersection with exploration wells (Krafla volcano in Iceland; Elders et al., 2011; 2014; Zierenberg et al., 2012). However, whether these shallow rhyolitic magma reservoirs may or not generate a volcanic eruption and the style this eruption would be are big questions not yet resolved. Rhyolitic explosive volcanism is modulated by the degassing of water, which is the main volatile present in those magmas at shallow levels (e.g. Wallace et al., 2015). Then, understanding the mechanisms of how water degasses from a rhyolitic melt at shallow levels and the role of crystalline phases in these processes are crucial to understand how eruptable such a magma could be. This thesis aims to fill these gaps in knowledge, focusing on the effect of nanolite to phenocryst phases controlling magma degassing and properties.

Chapter 2 gives the background on the processes governing the degassing processes of silica-rich magma, the role of crystal in such processes and magma properties, how nanolites have been identified so far and why they have been suggested to promote explosivity in mgamas. This chapter also gives examples of silica-rich magmas erupted and currently shallow rhyolitic reservoirs.

Chapter 3 explains the experimental methodology followed in order to assess the main questions stated in this chapter and the way how pre- and post-experimental products were analysed.

Chapter 4 shows the influence of nanolites on gas bubble nucleation and growth dynamics, suggests that some very high naturally-occurring bubble number densities could be associated with the presence of magmatic nanolites and shows how the effects produced by nanolites in the degassing magma could push an eruption that would otherwise be effusive into the conditions required for explosive behaviour

Chapter 5 sheds light into the conditions at which nanolites crystallise in rhyolitic magma. It focusses in effect of cooling on Fe-Ti oxide nanolite formation, showing that nanolites can form at cooling rates and in timescales relevant for shallow magmas. This chapter also shows how the silicate melt changes during nanolite crystallisation and how both processes may promote an increase of viscosity and explosivity in eventually erupting shallow magma.

Chapter 6 shows the coupled effect of microlites and phenocrysts on degassing of rhyolitic magma in terms of the roles of each type and size of mineral promoting bubble nucleation, coalescence and outgassing.

Chapter 7 gives first insights into the parameters controlling degassing and explosivity in shallow rhyolitic magma for slow decompression scenarios and the role play by crystallising nanolites during these processes.

Finally, chapter 8 gives the main conclusions obtained in this work regarding all the processes previously mentioned and possible future directions for assessing new scientific questions arose from this work.

2

Theoretical background

2.1 Degassing of high-silica magma

2.1.1 Volatile exsolution and bubble growth

Magma ascent is driven by bubble growth. At every volcano, volatiles play a fundamental role in conducting magma to the Earth's surface and generating eruptions. It is well known that magmas have many volatiles dissolved, from which the most abundant are H_2O, CO_2, S, Cl and F (e.g. Wallace et al., 2015). In high-silica magma, water becomes the most prevalent volatile, because is the most soluble volatile and then the last volatile species exsolving in most melts (Wallace et al., 2015; Shea 2017). Water can be exsolved when the magma reduces solubility, the maximum amount of a volatile species that can be dissolved under given conditions, and reaches supersaturation conditions (e.g. Zhang 1999; Liu et al., 2005). Supersaturation then is the difference between actual conditions (pressure and temperature) and the conditions at which the concentration of dissolved volatiles in the silicate melt would be in equilibrium with the co-existing gas phase, i.e. supersaturation represents the energy that must be supplied to increase the surface area between the two fluids in order to nucleate a gas phase bubble (Gonnermann and Manga 2012). Then, this supersaturation is a consequence of the attractive molecular forces that produce a jump in pressure across a curved interface between two fluids, also called surface tension (Gonnermann and Manga 2012).

The solubility reduction that causes supersaturation conditions may be driven in natural magmas by three main processes which are: (1) crystallisation, that changes melt composition

and increases volatile concentration (e.g. Zhang et al., 2007), (2) heating (e.g. Lavallée et al., 2015), but is mainly driven by (3) decompression during magma ascent or by a removal of overlying rocks (e.g. Sparks 1978; Zhang et al., 2007).

Volatiles, once exsolved, form bubbles that can grow by mass addition via volatile diffusion from the silicate melt or expansion of the supercritical fluids (from now on called gas phase) already exsolved (e.g. Sparks 1978) into the bubbles (Fig. 2.1), adding more buoyancy to the magma while this process occurs (Gonnermann and Manga 2007). However, when growing the viscosity of the bubble walls (i.e. silicate melt) is sufficient to inhibit bubble growth at equilibrium volume generating a viscous resistance to grow (e.g. Gonnermann and Manga 2007; 2012), increasing the gas pressure inside the bubble, which in turn, exerts high stresses on the surrounding liquid (Prousevitch et al., 1993). While growing, bubbles might remain isolated and build-up overpressure, or form permeable networks that allow the supercritical fluids escape as gas via outgassing, reducing bubble overpressure (Lensky et al., 2001; Gonnermann and Manga, 2007; 2012) and releasing the gas into the atmosphere or conduit walls (e.g. Jaupart and Allègre 1991).

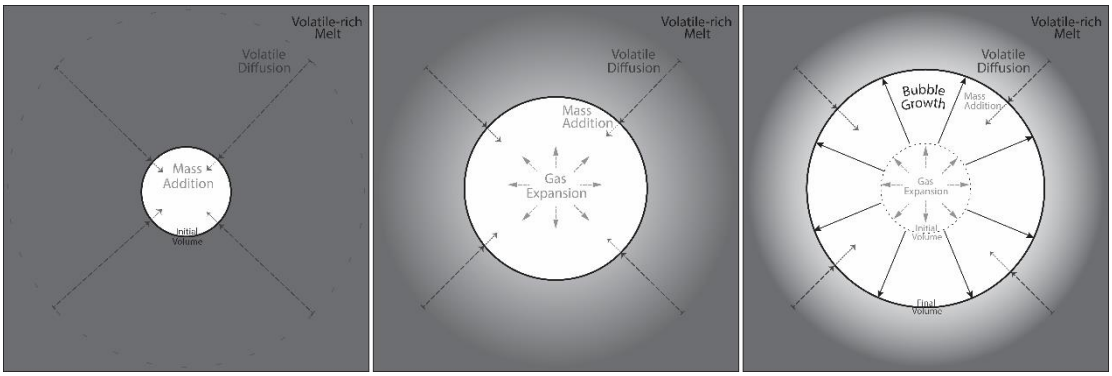

Figure 2.1. Bubble growth scheme. When nucleated, a bubble grows by mass addition and gas expansion together with a viscous relaxation of the surrounding melt. See the process in time from left to right.

A first-order control on whether an eruption can be explosive or not, is the rate at which bubbles grow in the melt (e.g. McBirney and Murase, 1970; Forte and Castro 2019), and the propensity for permeable outgassing during bubble growth (e.g. Degruyter et al., 2012). Both of these factors - bubble growth rates and permeable outgassing efficiency - are influenced strongly by the number density of bubbles that form in nucleation events as high bubble number densities shorten the distances for water to diffuse between bubbles, reduce the viscous resistance to growth, and result in smaller bubble-bubble pairs at the onset of permeability (e.g. Gonnermann and Manga 2007; Degruyter et al., 2012).

2.1.2 Bubble nucleation

Stated the causes of bubble formation and growth, bubble nucleation is not a simple process. Bubbles nuclei require to have a minimum size in order to remain stable and avoid reabsorption of the water molecules into the melt. That minimum size is given by the critical radius of the bubble (e.g. Proussevitch et al., 1993), which typically varies between 1-10 nm (Gonnermann and Gardner, 2013). Below this value, the bubbles will shrink and disappear. From here, bubble nucleation can occur homogeneously, i.e. when nucleation sites are lacking and the volatile separate from a one phase (silicate melt) magma to form a two-phase (gas bubbles + silicate melt) magma (e.g. Mourtada Bonnefoi and Laporte, 2004), or it can occurs heterogeneously, i.e. when crystals provide nucleation sites that allow volatiles to separate from the two-phase magma (silicate melt + crystals) as gas bubbles creating a three-phase (silicate melt + crystals + gas bubbles) magma (e.g. Cluzel et al., 2008). But even reaching supersaturation conditions, a rhyolitic magma might not nucleate bubbles. Water-rich bubbles do not nucleate as an immediate response to supersaturation and they require reaching a minimum supersaturation pressure in order to overcome the energy barrier provided by the surface tension (e.g. Gonnermann and Manga 2007; 2012). This supersaturation pressure can be in the order of ~10 MPa, but can also reach greater values than 100 MPa (e.g. Mangan and Sisson, 2000; Mourtada-Bonnefoi and Laporte, 1999, 2002; 2004; Hamada et al., 2010; Gonnermann and Gardner, 2013), finally causing water exsolution at higher rates than equilibrium scenarios at the moment when nucleation occurs (Mangan and Sisson, 2000; Shea 2017), generating an accelerated bubble growth and possibly high bubble number density. For homogeneous nucleation, bubbles per volume unit (or bubble number density, N_b) is dependent of the local decompression rate, volatile diffusivity, volatile concentration, temperature and surface tension (e.g. Toramaru 2006; Shea 2017).

2.1.3 The role of crystals in degassing of magma

It was stated that homogeneous nucleation required high values of supersaturation pressure in order to generate bubbles. On the other hand, crystals can play an important role favouring bubble formation by offering a surface for heterogeneous nucleation (e.g. Hurwitz and Navon, 1994; Mangan et al., 2004; Gardner and Denis, 2004; Cluzel et al., 2008; Larsen 2008; Shea 2017; Pleše et al., 2018). This effect can reduce the supersaturation pressure needed in order to nucleate bubbles to values below 20 MPa and even reaching ~1 MPa (e.g. Hurwitz

and Navon, 1994; Gardner et al., 1999; Gardner and Denis 2004). This is achieved because crystals reduce the energy required to create and maintain an interface between the bubble and the melt, or surface tension, (e.g. Shea 2017). Depending on the mineral phase, heterogeneous nucleation can also be promoted more by Fe-Ti oxides than other phases such as pyroxenes and feldspars (Fig. 2.2), since they increase the contact angle between the bubble interface and the crystal, reducing the energy needed for nucleation (e.g. Shea 2017).

Additionally, as shown beforehand, the bubble number density is strongly dependent of decompression rate for homogeneous bubble nucleation (e.g. Mangan and Sisson, 2000; Mourtada-Bonnefoi and Laporte, 2004; Toramaru 2006), but the decompression rate needed to reach a certain value of N_b can decrease considerable by several order of magnitude when nucleation occurs heterogeneously (e.g. Cluzel et al., 2008; Hamada et al., 2010, Shea 2017). Since the decompression rate controls the degree of supersaturation of the silicate melt (e.g. Gonnermann and Manga 2007; 2012), is supersaturation or a significant amount of crystals what mostly dictates N_b in a degassing magma, and hence the inter-bubble distances for water to diffuse favoring equilibrium degassing at higher Nb values (e.g. Gonnermann and Manga 2007; Shea 2017).

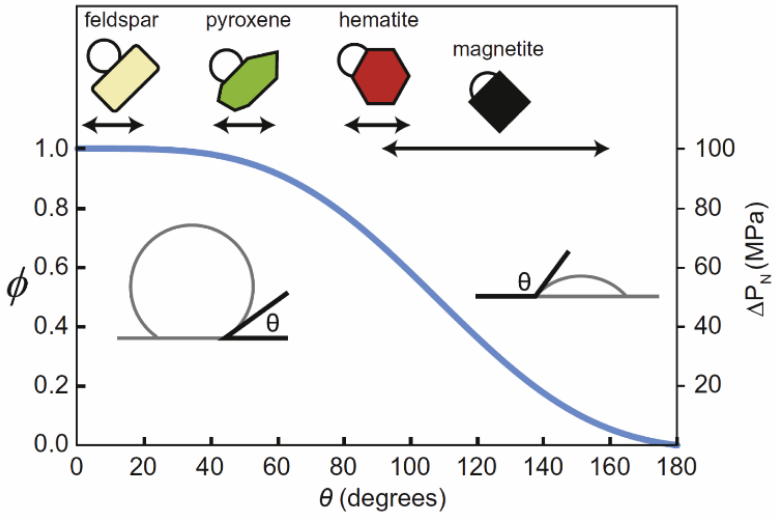

Figure 2.2. Crystalline phase and contact angle relationship for heterogeneous bubble nucleation. ∅ represents a factor dependent on the contact angle between the bubble interface and the solid, it is equal to 1 for homogeneous nucleation. θ is the contact anlge related to melt-crystal and bubble-crystal interfacial energies, where higher angles reduce the energy needed for nucleation. Image modified from Shea (2017).

While low-crystalline or crystal-free magmas tend to preserve impermeable networks or have high percolation thresholds (e.g. Lindoo et al., 2016; Lindoo et al., 2017; Giachetti et al., 2019; Ryan et al., 2019), another important known effect of crystals is favouring bubble coalescence and connectivity as a consequence of limiting bubble growth and expansion (Okumura et al., 2009; Oppenheimer et al., 2015). This effect can decrease the percolation threshold (the critical porosity at which permeability starts) and it has been studied individually for microlites- and phenocrysts-bearing magmas (Lindoo et al., 2017, deGraffenried et al. 2019) and magma analogues (e.g. Colombier et al., 2020).

2.1.4 Outgassing

As mentioned before, the efficiency at which the exsolving volatiles can escape from the multi-phase magmatic system via outgassing at shallow levels will be crucial to determine if a magma will erupt effusively or explosively (e.g. Rust and Cashman, 2004; Mueller et al., 2008; Gonnermann and Manga, 2012; Colombier et al., 2017a; Cassidy et al., 2018). The way and timescales at which permeable pathways form are then critical to determine whether a magma will produce an effusive or explosive volcanic eruption when reaching the surface.

Outgassing through permeable networks can occur when gas phase bubbles (e.g. Giachetti et al., 2019) and/or fractures (e.g. Heap et al., 2019) connect each other through the magma. So far, the known mechanisms that play important roles favouring the permeability of magmas are crystallisation (e.g. Oppenheimer et al., 2015; Lindoo et al., 2017; deGraffenried et al. 2019; Colombier et al., 2020), porosity increase (e.g. Eichelberger et al., 1986; Colombier et al., 2017a), bubble coalescence and connectivity (Blower 2001; Colombier et al., 2017a), low degree of shear deformation (Okumura et al., 2009; Gonnermann et al., 2017) and fracturing (e.g. Kushnir et al., 2017; Farquharson et al., 2017). While the mechanisms that help to decrease the permeability of a magma are the compaction or collapse of the pore network (e.g. Okumura et al., 2009; Ashwell et al., 2015), high degrees of shear deformation (Gonnermann et al., 2017), viscous healing of fractures by welding (Tuffen et al., 2003; Kennedy et al., 2010) and the particle-filling of fractures (e.g. Kendrick et al., 2016; Heap et al., 2019). However, outgassing processes are complex and permeability can undergo increases or reductions and turn from one to the other one in hysterical processes (e.g. Rust and Cashman 2004). For instance, while the pores pressure increases and remains higher than the magmastatic pressure, the permeable network is stable. However, when the pressure of the pore-connected network is exceeded by

the magmastatic pressure, the pore network can collapse reducing the porosity and the permeability of the magma (e.g. Wadsworth et al., 2016; Kennedy et al., 2016).

2.2 Nanolites in natural and experimental products

It has been previously shown in this chapter that crystal at micro- to millimetre scale have important effects on the degassing of magma, however the observation that nanolites (nanometer-scale crystalline phases) are extant in products of explosive volcanism (e.g. Mujin and Nakamura 2014) raises the general question as to what their physical role might be in bubble dynamics during magma ascent and volcanic explosivity.

Nanolites have been identified in natural volcanic products (e.g. Schlinger et al., 1988; Sharp et al., 1996; Mujin and Nakamura 2014; Barone et al., 2016; Zellmer et al., 2016; Colombier et al., 2017b), and experimental products (e.g. Liebske et al., 2003; Di Muro et al., 2006; Di Genova et al., 2017). They were defined as such by Sharp et al., (1996) and since then they have had increasing attention, since the formation of nanolites has been suggested as a factor that may favour heterogeneous bubble nucleation (Shea 2017), and they have been invoked as a potential control on the eruptive style of volcanoes (Mujin and Nakamura 2014; Mujin et al., 2017; Di Genova et al., 2017).

2.2.1 Melt properties and nanolite formation

It has been observed that nanolites can crystallise in magmas at low pressure, most likely, when dehydration-driven undercooling increases (e.g. Mujin and Nakamura 2014), during magma annealing or slow cooling (Liebske et al., 2003; Di Muro et al., 2006). But no study has been made so far on the conditions at which nanolites can form, as most of the nanolite observation has been made for Fe-Ti oxides, the iron oxidation state of the melt for sure plays an important role in forming nanolites and modifying the silicate melt from which the elements are uptaken. All this, with important impacts in the physical properties of magma.

The physical properties of a magma are mainly controlled by the chemical structure of its silicate melt phase and the physical presence of suspended phases. Of these, it is magma viscosity which is often a dominant factor determining whether a magma will erupt effusively

or explosively (e.g. Di Genova et al., 2017a; Cassidy et al., 2018). Magma viscosity depends on the viscosity of the silicate melt phase as well as the crystal load, and it can increase orders of magnitude with increasing crystal content (e.g. Costa 2005; Cimarelli et al., 2011; Chevrel et al., 2015; Kolzenburg et al., 2018). The effect of oxygen fugacity on the viscosity of the silicate melt phase is also important, as magma viscosity will increase where more oxidising conditions are reached (e.g. Kolzenburg et al., 2018), and because oxygen fugacity determines the iron oxidation state of the silicate melt. Iron can act in silicate melts as network former (Fe_2O_3) or network modifier (Fe_2O) according to its oxidation state (Dingwell and Virgo, 1987), producing that the higher relative abundance of oxidised iron (Fe^{3+}), the higher the silicate melt viscosity (e.g. Liebske et al., 2003; Bouhifd et al., 2004; Di Genova et al., 2017b).

Nanolites crystallisation also has the potential to have an important impact on the physical properties of magmas. It has been shown by Di Genova et al.(2017a) that Fe-Ti oxide nanolite crystallisation can increase the viscosity of a rhyolitic magma by several orders of magnitude by depleting the silicate melt in Fe and loading the magma with crystals. Considering this and the possible effect of nanolites on degassing and eruptive style of volcanoes, it becomes crucial to better understand the conditions and timescales for these nanolites to form and the structural changes in the silicate melt occurring during nanolites crystallisation.

2.2.2 Identification of nanolites and changes in silicate melt

Nanolites are not easy to identify. Scanning and transmission electron microscopy have been able to identify them (e.g. Sharp et al., 1996; Liebske et al., 2003; Mujin and Nakamura 2014; Mujin et al., 2017) and indirectly magnetite has been inferred to be a nanolite phase from magnetic increases in nanolite-bearing samples (e.g. Di Genova et al., 2017a). However, the small nature of nanolites makes them difficult to study, since they are smaller than or at the limit of the resolution of most of the analytical techniques (e.g. electron microprobe analysis, scanning electron microscope) and their signals thus mix with those of the host glass phase, but spectroscopic methods provides an opportunity to distinguish phase specific signals.

Raman spectroscopy has been proved to be a powerful non-destructive tool for studying silicate melt structure, oxidation state and water concentration in glasses (e.g. Mysen et al., 1980; Di Muro et al., 2006a; Di Muro et al., 2009; Mercier et al., 2009; Le Losq et al., 2012; Neuville et al., 2014; Di Genova et al., 2017c; Le Losq and Neuville 2017; Giordano et al., 2019), as well

as for confirming the presence of Fe-Ti oxide nanolites. Di Genova et al. (2017c) showed that a peak between $670 - 690\ cm^{-1}$ of the Raman spectra of silicate glasses appears when Fe-Ti oxide nanolites are present, with a concomitant decrease of the what is called the Fe^{3+} band.

The Raman spectra shape of silicate glasses is commonly divided into three regions: (1) the low wavenumber (LW) between $\sim 200 - 650\ cm^{-1}$, (2) the middle wavenumber (MW) between $\sim 650 - 850\ cm^{-1}$, and (3) the high wavenumber (HW) between $\sim 850 - 1250\ cm^{-1}$, where all of them can be found in literature with slight variations in the extremes wavenumbers (e.g. Mercier et al., 2009; Neuville et al., 2014; Giodano et al., 2019). Among these, the less constrained is the MW region, which is mainly attributed to Si-O bond stretching vibrations in the Si-O-Si plane and its intensity increases with Si content or more polymerised glasses (Seifert et al., 1982; McMillan et al., 1994; Giordano et al., 2019).

The shape of the LW region responds to vibrations of tetrahedra rings with commonly three to six or even more members present in the silicate network (e.g. Neuville et al., 2014; Giordano et al., 2019). On the other hand, the shape of the HW region responds to bond stretching vibrations of (Si^{4+}, Al^{4+} or Fe^{3+})-O^- units tetrahedrally coordinated that can have variable number of non-bridging oxygens. These units are commonly denoted as Q^n with *n* being the number of bridging oxygens varying from 0 to 4 (e.g. McMillan, 1984; Mercier et al., 2009; Neuville et al., 2014; Giordano et al., 2019). The effect of network-modifiers or charge balancing cations on the structure of the silicate melt can then be inferred from these localised bands in this region (e.g. Mercier et al., 2009).

In silicate glasses, the assignment of different bands to each of these Q^n species can be variable depending on the particular chemical differences of bonds in the material studied given by the ions forming them (e.g. Mysen et al., 1980; Furukawa et al., 1981; Mysen et al., 1981; Le Losq and Neuville, 2017). However, latest studies (e.g. Neuville et al., 2014; Di Genova et al., 2017b; Le Losq et al., 2017) have assigned the bands $\sim 930 - 960\ cm^{-1}$ and $\sim 1090 - 1100\ cm^{-1}$ to Q^2 and Q^3 units respectively, and $\sim 1140 - 1150\ cm^{-1}$ and $\sim 1190 - 1200\ cm^{-1}$ to $Q^{4,II}$ and $Q^{4,I}$ units differing in the angle of vibrations, but both counting for Q^4 units. It has also been recognised a band at $\sim 1070\ cm^{-1}$ related to structural units with metal or alkaline cations (Fukumi et al., 1992) that is not affected by Q^n species distribution (Le Losq et al., 2017). This band has been named as T_{2s} and correlated to ferrous iron (Fe^{2+}) in rhyolitic glasses, together with a band at $\sim 965 - 980\ cm^{-1}$ that has been attributed to the ferric iron (Fe^{3+}) in the structure possibly as four-fold coordinated (e.g. Cochain et al., 2012; Stabile et al., 2017; Di Genova et al., 2017b).

2.3 Magmatic fragmentation in silica-rich magma

The most explosive eruptions are associated to high viscosity magma such as dacitic or rhyolitic (e.g. Eichelberger, 1995; Gonnermann, 2015). Even if eruptions of silica-rich magmas can have effusive phases, most of these eruptions have had at least an explosive eruptive phase (e.g. Eichelberger and Westrich, 1981; Castro and Dingwell, 2009; Castro et al., 2013; Forte and Castro, 2019). Consequently, the control mechanisms of fragmentation and how this process occurs in natural silic-rich magma is crucial to understand explosive eruptions.

Magma fragmentation, the process at which the magma transforms from being a continuous silicate melt phase with crystals and bubbles into discrete pieces of magma surrounded by a continuous gas phase, is driven by bubble growth when magma volume increases and the mama accelerates toward the surface. This is a process that is thought to occur in a narrow depth interval at the fragmentation surface (Gonnermann and Manga, 2007). The magmatic fragmentation processes then can occur driven by two main mechanisms which are brittle fragmentation and fluid-dynamic breakup (Gonnermann, 2015). However, the process that produces fragmentation may differ depending on the type of magma and mainly on its viscosity.

The fluid-dynamic breakup occurs mainly in low-viscosity magmas such as basaltic ones and is driven by a decoupled gas phase respect to magma. In these magmas, bubble growth is not hindered by melt viscosity making that only little overpressure builds up compared to silicic magmas and leading to significant bubble coalescence (Gonnermann, 2015; Cashman and Scheu, 2015). This mechanism can produce eruptions as magma jets (Hawaiian eruptions) and magmatic bubble bursts (Strombolian eruptions), where the first ones are characterised by magma escaping the volcanic vent at speeds of commonly $\sim\ 10 - 100\ m\ s^{-1}$ (Wilson, 1999), reaching typically hundreds of meters height (Houghton and Gonnermann, 2008), while the later are characterised by the bursting of large gas slugs formed by high degree of bubble coalescence (Gerst et al., 2013; James et al., 2013). Basaltic Plinian eruptions can also occur, but their fragmentation mechanisms are still poorly understood, however a recent study (Arzilli et al., 2019) associates these highly explosive basaltic eruptions to rapid crystallisation and increase in viscosity.

On the other hand, brittle fragmentation occurs when the melt, a viscoelastic material, responds to an applied stress in a predominantly elastic manner which is the case of highly polymerised

silicate melts such as rhyolitic melts (Gonnermann 2015). Magma expansion, driven by bubble growth, can result in extensional strain rates large enough to reach the glass transition, which is the transition between viscous (or ductile) and elastic (or brittle) behaviour (Dingwell, 1996; Papale, 1999). When a silicate melt is subjected to large stress over a short period of time, deformation will occur, accommodated by reversible changes in molecular bonds (or elastic deformation at small strain), but when the same silicate melt is long subjected to large stress, the inability of the melt structure to relax on the timescale of the deformation can result in brittle failure (e.g., Dingwell and Webb, 1989; Webb and Dingwell, 1990).

This process of brittle failure is likely to occur at scenarios of silica-rich magma subjected to rapid decompression, where buoyant bubble rise is hindered by a viscous drag of the surrounding melt and the gas phase is then coupled to the magma, making the bubbles more prone to build up overpressure and produce acceleration of the magma while bubbles expand (Gonnermann, 2015). The fragmentation process has been extensively studied experimentally through shock tube experiments (e.g., Alidibirov and Dingwell, 1996; Martel et al., 2000; 2001; Spieler et al., 2004; Kueppers et al., 2006; Scheu et al., 2006; 2008; Mueller et al., 2008), where very rapid decompression is triggered by the rupture of a diaphragm. Through these experiments, it has been shown that fragmentation can be achieved by brittle failure across the glass transition by rapid decompression. Here, brittle failure occurs when the porous overpressure exceeds a critical fragmentation threshold, that mainly depends on the extent of magma porosity and permeability (e.g. Spieler et al., 2004; Mueller et al., 2008). Additionally, numerical models have shown (e.g. Papale, 1999) that acceleration of the ascending magma can exceed the structural relaxation rate of the magma or melt phase and cause fragmentation (Dingwell, 1996).

In natural cases, fragmentation of silica-rich magma can produce Plinian eruptions, which are characterised by sustained activity of hours to days, and are commonly explained by both bubble overpressure and acceleration (e.g. Cashman and Scheu, 2015). Other style of eruptions commonly produced by silica-rich magma are the Vulcanian eruptions, which are short-lived explosions mainly caused by a disruption of a shallow stagnant magma in the conduit, such as plug or dome. In this type of eruptions, initially vesicular magma result in fragmentation as a result of bubble overpressure caused by rapid decompression. The disruption of the magma plug or dome, subsequently, drives the migration of a fragmentation front downward in the conduit, which creates new surfaces that repeat the fragmentation in a layer-by-layer process,

as long as the overpressure is sufficient to overcome the strength of the magma (Fowler et al., 2010; Cashman and Scheu, 2015).

2.4 Shallow rhyolitic magmas

Two big eruptions fed by rhyolitic magma occurred in the last dozen years kept the attention of the scientific community: Chaitén 2008 and Cordón Caulle 2011.

Chaitén volcano is placed in the Southern Volcanic Zone (SVZ) of the Andes, in Chile. It started and eruptive cycle in 2 May, 2008, with a brief seismic forewarning of only a day before the eruption when earthquakes were felt by residents of Chaitén city (Castro and Dingwell, 2009). This was considered a dormant volcano and hence no great monitoring system was dedicated to it by the date. This eruption lasted almost two years and started with a highly explosive (Carn et al., 2009; Watt et al., 2009) Plinian phase that raised ash columns to height of $19 - 21\ km$ that formed several with pyroclastic density currents (e.g. Pallister et al., 2013). After the 10 May, the volcano showed hybrid behaviour with simultaneous explosive emissions of ash and lava effusion that, finally, after 31 May transitioned to long-lasting effusive emissions forming a lava dome ending by the beginning of 2010. The materials erupted during this period were rhyolitic (e.g. Castro and Dingwell, 2009; Alfano et al., 2011; Pallister et al., 2013) and have been inferred to be previously stored at $\sim 5\ km$ depth with temperature between $780 - 825\ °C$ (Castro and Dingwell, 2009).

Cordón Caulle is a fissure system part of the SVZ and forms together with Puyehue volcano the Puyehue-Cordón Caulle Volcanic Complex. This volcano entered in an eruptive cycle in 4 June, 2011 that started with rhyolitic (Castro el at., 2013) explosive activity emitting ash columns up to $10 - 12\ km$ height (Bonadonna et al., 2015). After ten days, the eruption moved to a hybrid behaviour (Schipper et al., 2013) of Vulcanian explosions together with the emission of a lava flow of ~3.6 km length that finished in August 2012 (Tuffen et al., 2013). The source of this rhyolitic magma has been estimated at a depth of $\sim 2.5 - 5\ km$ depth with temperatures between $870 - 920\ °C$ (Castro et al., 2013).

However, what has kept the attention of the community is not only the erupted rhyolitic magmas, but those that have been recognised to be stored at shallow levels in the crust that

could eventually be erupted, potentially generating big explosive eruptions like just mentioned. This is case for Laguna del Maule and Krafla rhyolitic reservoirs.

2.4.1 Laguna del Maule Volcanic Field in Chile

The Laguna del Maule Volcanic Field is placed in the northern part of the Southern Volcanic Zone (SVZ) of the Andes in Chile. It covers an area of about 500 km^2 with 130 basaltic-to-rhyolitic eruptive vents around the lake the gives its name. In this area, more than 350 km^3 of volcanic material have been erupted since the Pleistocene (Munizaga, 1978; Frey et al., 1984; Hildreth et al., 2010), but the most interesting part is that guring the post-glacial period (<25 ky; Singer et al., 2000), 36 identified rhyolitic-to-rhyodacitic lava flows and domes were erupted from 24 eruptive vents (Fig. 2.3) around the lake (Hildreth et al., 2010).

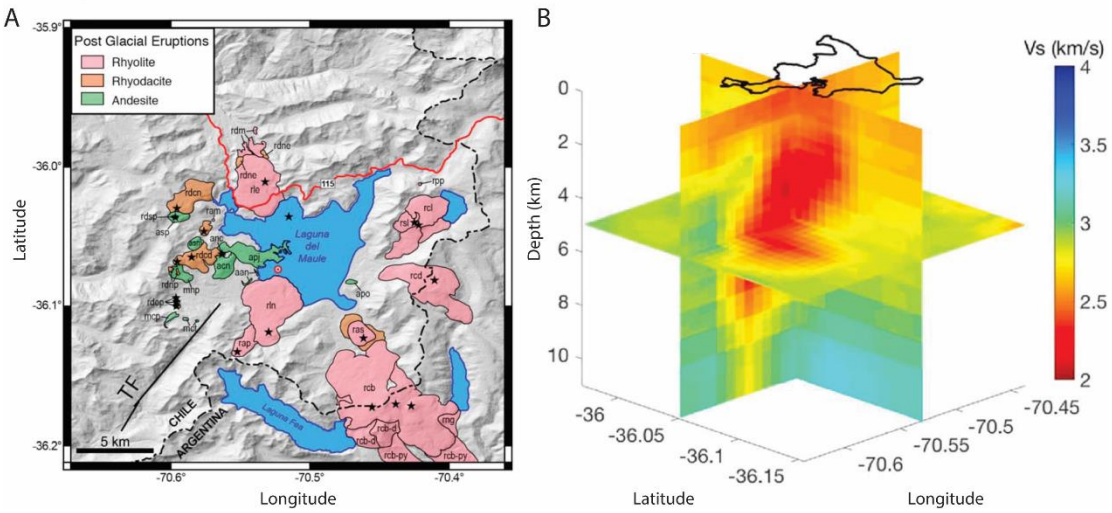

Figure 2.3. Laguna del Maule identified magma reservoir. (**A**) Shows the location of the area and its silica-rich post-glacial eruptive units. (**B**) Shows the magma reservoir imaged with surface-wave tomography. Images modified from Wespestad et al. (2019).

While the origin of the silica-rich eruptive units is still unknown, this area has been the focus of multidisciplinary studies in recent years aiming to understand an accelerated ground uplift of its southwestern part (e.g. Fournier et al. 2010; Feigl et al., 2014). The rate of ground inflation has been estimated in $> 250\ mm/yr$ between 2007 and 2012 (Feigl et al., 2014), reaching a peak of $400\ mm/year$ in early 2010. A decreasing rate of inflation was recorded between 2013 and 2014, which coincided with an event of high seismicity in the area (Le Mével et al., 2016). This uplift has been faster than other documented deformation events at big

calderas such as Yellowstone and Santorini (Chang et al., 2010; Newman et al., 2012). The uplift at this zone has been attributed to inputs into a shallow ($2-8\ km$ depth; Fig. 2.3) rhyolitic reservoir (Feigl et al., 2014; Le Mével et al., 2016; Miller et al., 2017; Cordell et al., 2018; Wespestad et al., 2019).

2.4.2 Krafla volcano in Iceland

The case of Krafla volcano has more direct evidences. Within the Iceland Deep Drilling Project (IDDP), an industry-government consortium aimed to explore for supercritical hydrothermal fluids with the potential to be utilised for energy production (Friðleifsson and Elders 2005). The IDDP-1 drill well was originally designed to drill $4-5\ km$ into the Krafla geothermal field. However, the drill unexpectedly intersected rhyolitic melt at approximately $\sim 2100\ m$ depth (Fig. 2.4) that prevented more drilling (Elders et al. 2011). This is not the first time that magma has been intersected in drilling during geothermal exploration, as the cases of the Puna Geothermal field in Hawaii that intersected dacitic melt at $2488\ m$ depth in 2005 (Teplow et al., 2009) and the previous intersection of glass with 69.0 to 78.8 $wt.\%$ SiO_2 that was recovered at the Krafla geothermal system in 2008 at a depth of 2571 m (Mortensen et al., 2010).

Krafla volcano is placed in North Iceland Rift Zone. It is made up of a central volcano and a NNE-SSW fissure swarm (Fig. 2.4A). ~100 ka, a caldera-forming eruption occurred depositing a rhyolitic welded tuff. The most recent periods of activity at Krafla occurred between 1724-1729 with the Myvatn-fires, and between 1975-1984 with the Krafla-fires, both eruptions are characterised by rifting and basaltic material emitted. A magma chamber at $3-7\ km$ depth beneath the volcano was detected during the Krafla-fires by S-wave shadowing (Einarsson, 1978) when the centre of the caldera was cyclically uplifted until basaltic magma was released by dike injections/eruptions into the fissure swarm to the north. The bimodal nature of the eruptive rocks at Krafla, i.e. mainly basaltic and rhyolitic, has been studied and the rhyolitic part has been proposed to have formed by near-solidus fractionation of melted hydrothermally altered basalts, rather than the typical assumption of extreme fractionation of primary basaltic magma (Jónasson 1994; 2007).

As described by Elders et al. (2011), the magma recovered in the IDDP-1 well at $\sim 2.1\ km$ depth corresponds to a partly vesicular and sparsely phyric high-silica rhyolitic glass with

76.53 $wt.\%$ SiO_2 and ~1.8 $wt.\%$ H_2O dissolved. Its main mineral phases are titanomagnetite, plagioclase, augite and pigeonite and it is emplaced at pressures intermediate between hydrostatic and lithostatic ($\sim 16 - 55\ MPa$) at 850-920 °C (Elders et al., 2011; Zierenberg et al., 2012). This magma was interpreted to have formed by anhydrous mantle-derived magma assimilating partially melted hydrothermally altered basalts (Elders et al., 2011).

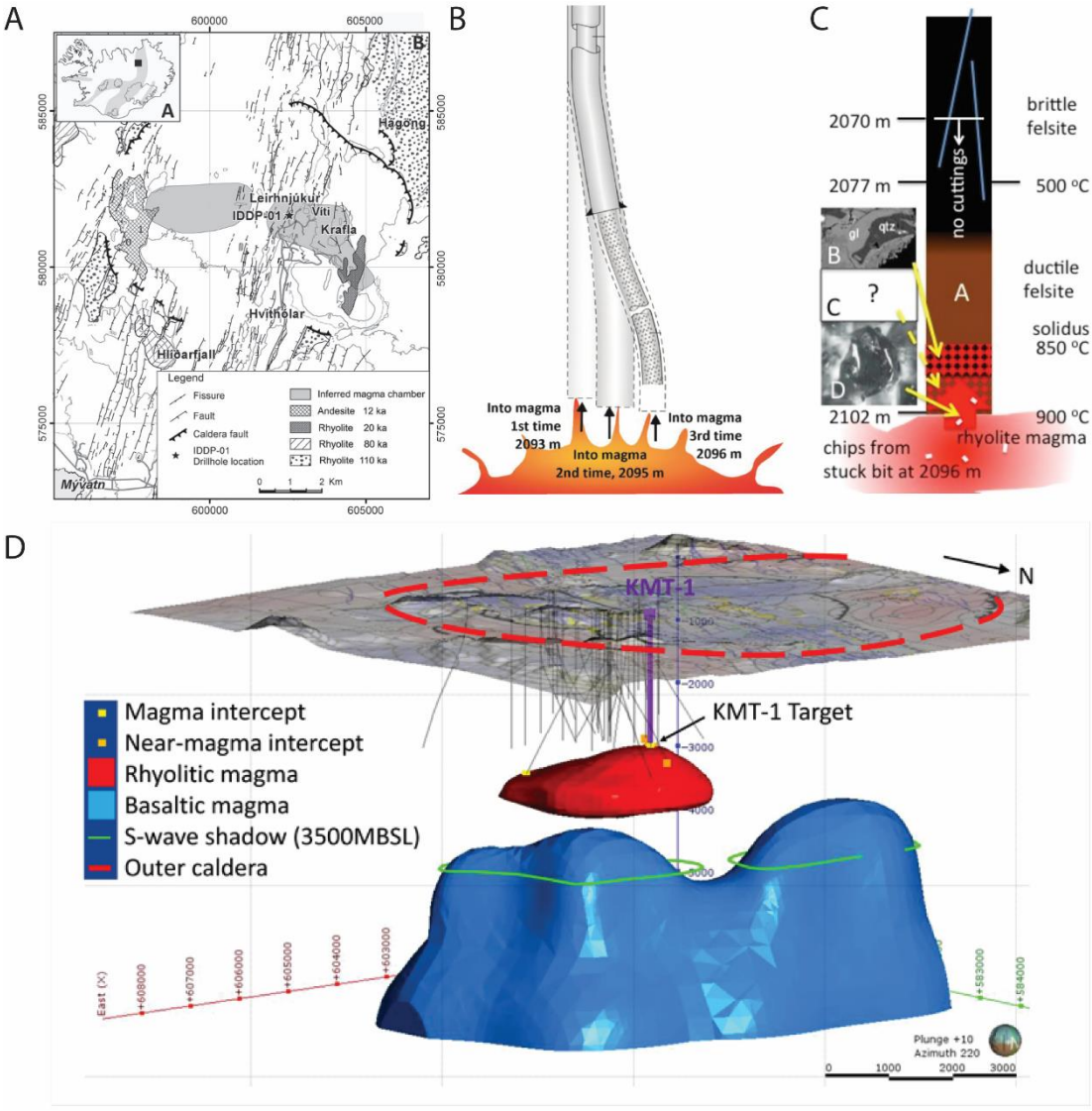

Figure 2.4. Location of IDDP-1 well in Krafla, Iceland. (**A**) Map showing the location of Krafla in Iceland and the place of the IDDP-1 drill. Map modified after Sæmundsson (2008) and Elders et al. (2011). (**B**) Scheme of the IDDP-1 well hit into magma. Image modified after Friðleifsson et al. (2013). (**C**) Scheme of the main findings by the IDDP-1 well. In the scheme, A represents the well, B represents the partially melted felsite, C is the missing partially crystallised rhyolite and D represents the rhyolite found. Scheme modified after Eichelberger et al. (2018). (**D**) Model of the Krafla rhyolitic reservoir targeted by the project Krafla Magma Testbed (KMT) with the planned drill KMT-1. Figure from Eichelberger (2019).

3

Materials and methods

This chapter contains all the information about the different materials used for every kind of experiment conducted in this thesis. The information about the sample preparation and pre- and post-experimental analyses are also described herein, together with the technical description for analytical methods and the experimental setups used for the different experiments. In this thesis, different types of experiments were conducted fulfilling different purposes which include heating-induced magma vesiculation, controlled magma cooling and slow decompression experiments. The materials used differ for every type of experiments, including cores of whole rock, synthesised glass and rock powder.

3.1 Experimental materials

Natural volcanic materials were collected from two different areas in order to use as staring material for experiments and synthesis of new samples. The first one is an obsidian from Hrafntinnuhryggur eruption of Krafla volcano in Iceland. The second one a vitrophyric rhyolite from Loma de los Espejos flow at Laguna del Maule Volcanic Field in Chile. Additional materials were synthesised using some of these natural ones, particularly with the obsidian from Krafla.

3.1.1 Natural obsidian

The natural obsidian collected from Hrafntinnuhryggur eruption at Krafla, Iceland, corresponds to a dark piece of glass with no visible fracture or alteration. Microscopically, it

contains a very low crystallinity consistent of $<< 1\ vol.\%$ of Fe-Ti oxide microlites in a glassy groundmass and is free of other mineral phases. This material is also bubble- and nanolite-free (Fig. 3.1) checked with SEM and Ramana analyses (see following sections for details). Chemically, it corresponds to an Fe-rich rhyolite (according to Warshaw and Smith 1988) with 3.34 wt.% FeO_T. (Table 3.1). The portion of the block used for experiments has no visible fractures or alteration at a macro- and microscopic scale.

3.1.2 Natural vitrophyric rhyolite

This vitrophyric rhyolite was collected from Loma de los Espejos rhyolitic coulée at Laguna del Maule Volcanic Field in Chile. It corresponds to a slightly transparent glass containing $\sim 4.5\ vol.\%$ of phenocrysts of feldspars, biotite and Fe-Ti oxides, as well as microlites of feldspar and Fe-Ti oxides in the glassy groundmass (Cáceres et al., 2018). It is bubble- and nanolite-free (Fig. 3.1). The block used for experiments has no visible fractures or alteration at a macro- and microscopic scale.

3.1.3 Synthese Kb2 and Kb4

These two samples were synthesised using powder from the natural obsidian form Krafla. It was produced at high pressure and temperature in a Hot Isostatic Press (HIP) at the Rock Physics and Mechanics Laboratory, ETH Zurich in Switzerland. For preparation, a block of the natural obsidian was finely powdered and sieved down to $< 63\ \mu m$ particle diameter (Fig. 3.2). The powder was put in an iron cannister internally covered by a Mo foil, in order to avoid contamination from the cannister into the sample. The procedure followed was placing the cannister into a metallic box that allows to keep the shape of the tube while compacting with a press during filling. The filling process was done by adding between $10 - 55\ g$ of the powder and then pressing with a piston with a pressure of $20\ tons$ in order to compress the powder and minimize air volume. The procedure was repeated until filling one cannister of $5\ cm$-diameter and $10\ cm$-length, and a second cannister of $3.2\ cm$-diameter and $20\ cm$-length, representing the samples Kb2 and Kb4 respectively. A Mo lid and then an iron lid were put and the cannisters were then welded in order to seal them.

Both materials (Kb2 and Kb4) were then subjected to the same temperature and pressure of $800\ °C$ and $23\ MPa$ respectively for $3\ hours$ and then rapidly quenched at $\sim 40\ °C\ min^{-1}$ in

the HIP. Finally, the cannister were open with a saw for further sample preparation for experiments and for analyses of the materials. Both materials present $< 1\ vol.\%$ relicts of Fe-Ti oxides microlites and an estimate of $\sim 2\ vol.\%$ Fe-Ti oxide nanolites that were identified with the scanning electron microscope (Fig. 3.1), Raman spectroscopy (see Figure 4.2 in Chapter 4) and magnetic hysteresis analysis (Fig. 3.3). Small bubbles ($< 5\ \mu m$) can be found sporadically in the groundmass representing $<\ 1\ vol.\%$ of the sample.

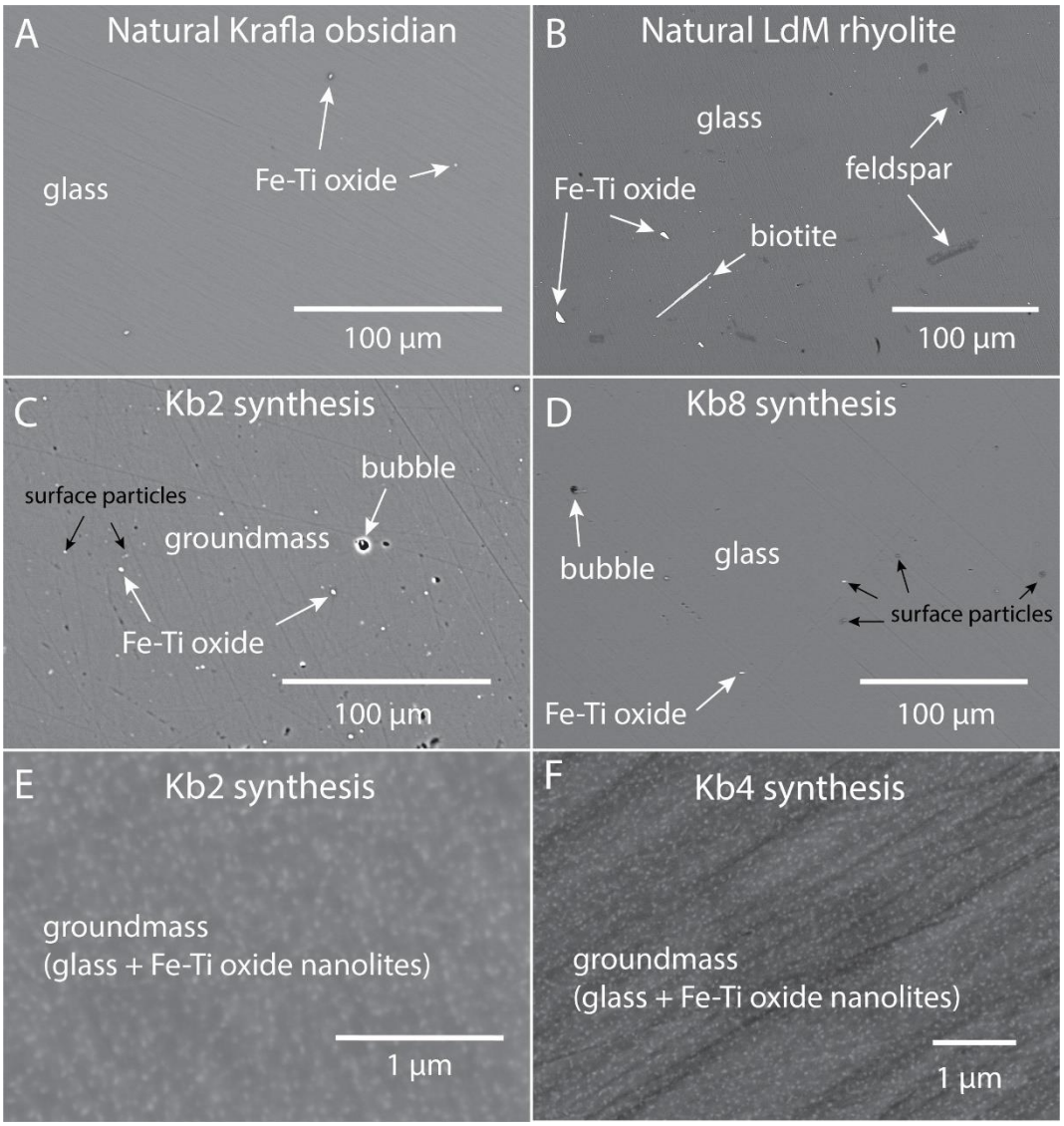

Figure 3.1. Scanning electron microscope images of the pre-experimental materials. Images were acquired with the back-scattered electron detector and show general textures for every sample type. (**A**) Natural obsidian from Krafla, Iceland. (**B**) Natural vitrophyric rhyolite from Laguna del Maule Volcanic Field, Chile. (**C**) Kb2 synthesis. (**D**) Kb8 synthesis. (**E**) Zoom in to the groundmass in Kb2 synthesis showing Fe-Ti oxide nanolites and glass. (**F**) Zoom in to groundmass in Kb4 synthesis also showing Fe-Ti oxide nanolites and glass.

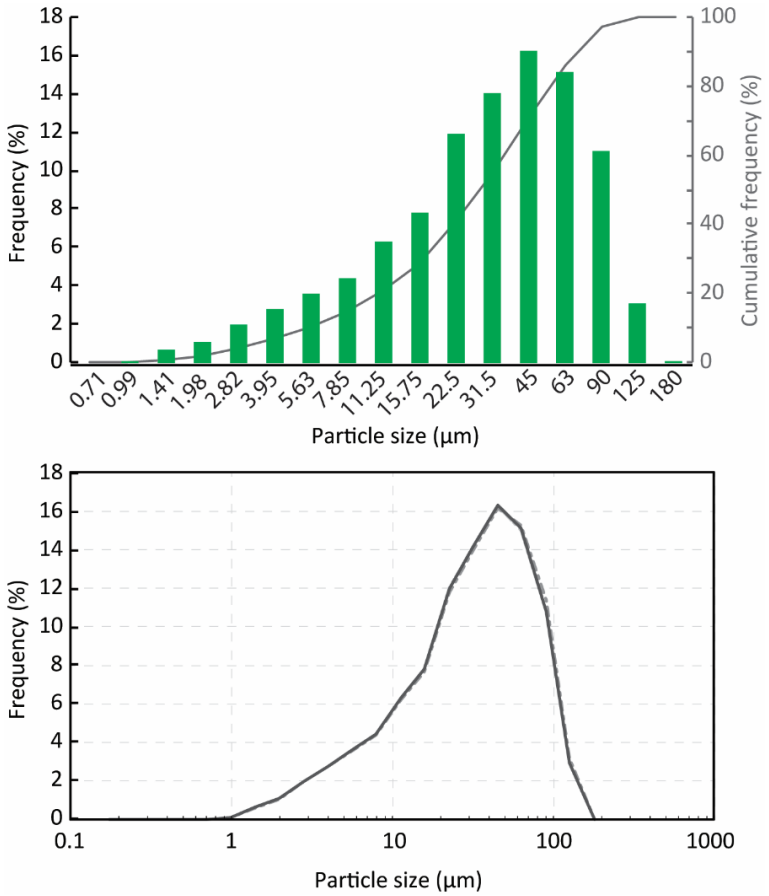

Figure 3.2. Particle size analysis of the pre-synthese powder. Approximately 90% of the material has a particle size smaller than 63 µm and the representativity of this sample size distributions is good shown by the three independent analyses conducted in the sample that can be seen in the lower figure overlapping each other.

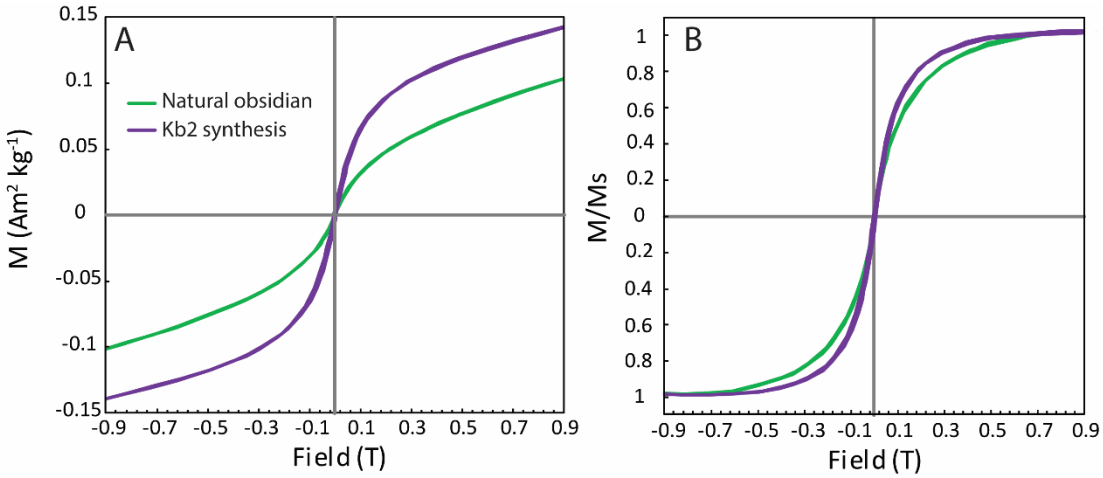

Figure 3.3. Magnetic hysteresis analyses of the Natural obsidian (nanolite-free) and the synthesis Kb2 (nanolite-bearing). (**A**) Shows the hysteresis loops of magnetisation for the field applied. (**B**) Shows the hysteresis loops corrected for a paramagnetic slope using the linear portion of every loop for fields higher than 0.5 T and normalised for the saturation magnetisation Ms (the magnetisation at which the projected slope crosses a field of 0 T). The samples shown a superparamagnetic behaviour and the magnetisation increases in the nanolite-bearing sample (Kb2) respect to the nanolite-free samples (Natural obsidian) for which the magnetisation is given by the Fe-Ti oxide microlites.

Table 3.1. Chemical composition of glass for the natural and synthesised samples. Data represent the average of 10 points (n=10) measured on the groundmass and normalised to a water-free basis. Shown are: Natural Krafla = Krafla natural obsidian, Kb2 = Synthesis Kb2 (nanolite-bearing, ~0.34 wt.% H_2O), Kb8= Synthesis Kb8 (~2.1 wt.% H_2O), LdM = Laguna del Maule natural vitrophyric rhyolite.

Oxides (wt.%)	**Natural Krafla**	**Kb2[a]**	**Kb8**	**Natural LdM[b]**
Original (n=10)				
SiO_2	75.55	75.51	75.14	75.11
TiO_2	0.26	0.21	0.24	0.14
Al_2O_3	12.14	12.18	11.97	12.86
FeOT	3.35	3.25	3.27	0.82
MnO	0.10	0.14	0.11	0.08
MgO	0.11	0.09	0.09	0.11
CaO	1.73	1.73	1.72	0.58
Na_2O	4.29	4.19	4.21	4.24
K_2O	2.73	2.75	2.67	4.40
P_2O_5	0.01	0.02	0.03	0.02
Cr_2O_3	0.02	0.01	0.02	0.01
MoO_3	0.06	0.01	0.04	-
Total	100.36	100.09	99.50	98.36
Normalised values				
SiO_2	75.27	75.44	75.52	76.36
TiO_2	0.26	0.21	0.24	0.15
Al_2O_3	12.10	12.17	12.03	13.07
FeO	3.34	3.24	3.29	0.83
MnO	0.10	0.14	0.11	0.09
MgO	0.11	0.09	0.09	0.11
CaO	1.73	1.73	1.73	0.58
Na_2O	4.27	4.19	4.23	4.31
K_2O	2.72	2.75	2.69	4.48
P_2O_5	0.01	0.02	0.03	0.02
Cr_2O_3	0.02	0.01	0.02	0.01
MoO_3	0.06	0.01	0.04	-
Total	100	100	100	100

b: Analysis correspond to the groundmass (glass + nanolites).

a: Chemistry from Cáceres et al. (2018) with n=5.

3.1.4 Synthesis Kb8

The synthesis Kb8 was prepared in the same hot isostatic press at higher temperature and pressure in order to produce a crystal-free and re-hydrated rhyolitic material. Here, the same procedure as for Kb2 and Kb4 was followed, but adding a specific amount of deionised water. The powder was previously dried at $199\ °C$ for $23\ hours$ and then stored in an air tight

container. After adding a small amount of powder into the cannister, this was pressed and then the water was added in small amounts ($< 1.5\ g$) with a calibrated high precision pipet. The filling procedure was continued adding more powder, repeating the pressing and adding more water. The addition of water was done controlling the weight percentage added according to the mass of obsidian powder added, in order to be the fraction of water targeted for the synthesis.

This material was prepared in a $3.2\ cm$-diameter and $20\ cm$-length cannister. The sealed cannister was then subjected to a temperature of $1000\ °C$ and pressure of $120\ MPa$ for $5\ hours$ to ensure homogeneous water dissolution and a complete sintering of the powder particles. The sample was then rapidly quenched at $\sim 40\ °C\ min^{-1}$ in the HIP. Finally, the cannister was opened with a saw for further sample preparation for analyses and experiments.

The final material is considered crystal-free with <<1 vol.% Fe-Ti oxide microlites, probably relicts from the original obsidian powder. This, according to scanning electron microscope imaging and Raman analyses (Figs. 3.1). Small bubbles ($< 5\ \mu m$) can be found sporadically in the groundmass representing $<<\ 1\ vol.\%$ of the sample. The water content of the resultant material is described in the next section. Additionally, no evidence of chemical contamination was found for all synthese (Kb2, Kb4, Kb8) either from the iron cannister or the Mo foil (Table 3.1).

3.2 Pre-experimental sample preparation and analyses

3.2.1 Drilling

The samples were drilled out from the cannisters and the natural materials with diamond-headed drills of $2.5 - 8\ mm$ inner diameter according to the different experiments or analyses conducted. For heating- or decompression-induced vesiculation experiments, a drill of $5\ mm$ diameter was used and $3 - 5\ cm$-length cores were obtained. Additionally, for recovering the samples after magma cooling experiments in Pt-Rh crucibles, a drill of $2.5\ mm$ diameter was used and the cores obtained were $\sim 5\ mm$-length. Additional cores of $8\ mm$ diameter were obtained for textural analyses and control experiments to check the influence of sample size.

3.2.2 Cutting

The cores were precisely cut into $\sim 1.5 - 8\ mm$-length discs that represent the different samples for experiment or analyses. The cutting was conducted using a $200\ \mu m$-thick wire saw. The corresponding sample size used for every type of experiments or analysis is explained in the corresponding chapter.

After cutting, samples were carefully cleaned with Aceton and deionised water in order to remove any wax or impurity from the samples surfaces, residuary from the cutting process. The cylindrical samples were then then dried at $100\ °C$ for $24\ hours$ in a furnace to remove humidity from the surface before weighing in a high precision balance ($0.01\ mg$) and sizing with a precision caliper ($0.01\ mm$).

3.2.3 Mounting

Discs of each sample were separately mounted into epoxy resin for further analyses. All the mounted samples were then carefully polished until a $3\ \mu m$ particle diamond-paste in order to generate a smooth surface that serves for imaging of nano- to milli-meter scaled crystals or bubbles, as well as for Raman analyses. All polished samples were cleaned with deionised water in an ultrasonic bath for $30\ minutes$ in order to remove any remaining particle from the surface. Then, the samples were dried at $50\ °C$ for $24\ hours$ in a furnace in order to eliminate water from samples surfaces that could alter analyses, especially Raman spectra acquisition. Before every experimental set, the materials used were analysed under several analytical techniques in order to identify the different phases (glass, crystals and vesicles) present, textural variations, chemical homogeneity or heterogeneity, possible chemical contamination and differences in some physical properties. These techniques are described below.

3.2.4 Scanning electron microscope

The materials were analysed with a HITACHI SU5000 scanning electron microscope (SEM) at LMU Munich, using the back-scattered electron detector (BSE) in order to obtain high precision images of the materials at a nano- to millimetric scale. Conditions were varied according to the phase targeted, but the most challenging was the imaging of Fe-Ti oxide

nanolites. For these particular phases, the conditions applied were an accelerating voltage between $10 - 12kV$, current of $0.1\ mA$ and $5.5\ mm$ working distance. Nanolites of Fe-Ti oxides were clearly visible as brighter phases at magnifications of $x13{,}000$ and higher. Energy dispersive X-Ray spectroscopy (EDS) was applied to selected points in the nanolite-bearing material for mapping of chemical elements around relict magnetite microlites. Materials Kb2 and Kb4 are nanolite-bearing. The identification of the mineral phases representing these nanolites was made with a Raman spectroscope which is explained below.

3.2.5 Simultaneous Thermal Analysis

All materials were analysed with Simultaneous Thermal Analysis (combined Differential Scanning Calorimetry and Thermogravimetry methods) using a NETZSCH® STA 449C Jupiter at LMU Munich, in order to obtain their glass transition temperature and water content. These analyses were performed with a heating and cooling phase of $25\ °C\ min^{-1}$ or $10\ °C\ min^{-1}$, being the same rate for heating and cooling at every analysis. The peak temperatures for the glass transition and the water concentrations for all analysed pre-experimental material are given in Table 3.2.

Table 3.2. Glass transition temperature and water concentration for the pre-experimental materials. Nat. = Natural, Syn. = Synthesis, LdM = Laguna del Maule, g = glass, n = nanolites, m = microlites, p = phenocrysts, STA- simultaneous thermal analysis.

Material	Nat. Krafla (g+m)	Nat. LdM (g+m+p)	Syn. Kb4 (g+n+m)	Syn. Kb4 (g+n+m)	Syn. Kb8 (g)
Tg peak temperature (°C)	689	769	677	678	494
Mass loss, 1000°C (wt.%)	0	0	0.22	0.21	2.07
H_2O_{STA}[a] (wt.%)	-	0.10	0.32	0.31	2.17
H_2O_{Raman} (wt.%)	-	-	-	-	2.10
H_2O_{FTIR} (wt.%)	0.15[b]	-	0.34	0.34[c]	-

[a] STA mass loss + solubility at 900°C according to Liu et al., 2005

[b] values from Tuffen and Castro (2009)

[c] assumed from Kb2

3.2.6 Raman spectroscopy

Raman analyses were performed in order to identify nanolite phases and water content of the materials, using a confocal HORIBA XploRa micro-Raman spectrometer at the Mineral

State Collection of Munich. The instrument was calibrated with a silica standard and the spectra were acquired with a green Nd:YAG-Laser ($532\ nm$ wavelength), focused through the $100x$ objective lens, with an $1\ \mu m$ laser spot diameter that provided a power at the sample surface of $\sim 2.5\ mW$. Laser attenuation was 25% of the total laser power, grating of $1200T$, confocal hole of $300\ \mu m$, slit of $200\ \mu m$ and an exposure times of $30\ s$ and $60\ s$ three times acquired for nanolites and water determination respectively. The backscattered Raman radiation was collected between $100 - 1500\ cm^{-1}$ for nanolite identification, in order to include the low and high wavelength regions, as well as the band where the Fe-Ti oxide nanolites peak appears. For water determination, the backscattered Raman radiation was collected between $50 - 4000\ cm^{-1}$ and the method of Di Genova et al. (2017c) was applied. The results were compared to additional analyses conducted at the University of Roma Tre.

Because of the Raman spectra might change as a function of excitation line and temperature (e.g. Neuville et al., 2014), all spectra were corrected for intensity (hereafter called Long-corrected spectra) according to Long (1977). Ten spectra were acquired for each sample in order to test the reproducibility of our analyses and an average of the Long-corrected spectra is used hereafter for analyses and further discussion. A third-degree polynomial baseline was systematically subtracted from all averaged spectra with reference at $100 - 200\ cm^{-1}$ and $1250 - 1400\ cm^{-1}$ when spectra are presented and directly discussed.

3.2.7 Water concentration of the materials

The water concentration, as just shown, was determined by STA and Raman analyses. However, for certain materials one or the other method carried issues depending on the analysis. Here I show the specific values of water concentration considered for each material.

For the natural obsidian, STA analysis does not show any mass loss up to $1000\ °C$ and the Raman analysis consider an error of at least $0.16\ wt.\%$. But a concentration of $0.11 - 0.15\ wt.\%$ H_2O was previously analysed with FTIR method by Tuffen and Castro (2009) for this eruptive unit. Here this last value is considered as the water concentration of the material.

The Laguna del Maule rhyolite shows a similar behaviour. No mass loss associated to water exsolution was registered, and this sample has not been previously analysed by FTIR, then a $0.1\ wt.\%$ H_2O is assumed, calculated according to the solubility of rhyolitic magma (Liu et al.,

2005) at $\sim 900\ ^{\circ}C$, which is the highest temperature of the STA analysis. Additionally, this value coincides with the expected viscosity at the glass transition temperature close to 11.4 log units, within some small error, when applied the viscosity model of Hess and Dingwell (1996) suitable for this composition. For this reason, this estimation is considered a good value for the water content of the sample.

The synthesised material Kb2 shows a mass loss equivalent to $0.22\ wt.\%$ H_2O for which the water concentration, adding the water solubility of $0.1\ wt.\%$ at $1000^{\circ}C$ of the maximum temperature for the STA analysis, the sample has $\sim 0.32\ wt.\%$ H_2O by STA method. However, considering the nanolite content of the sample, this is an underestimate of the glass water concentration. In order to obtain the actual water concentration of the glass, an additional FTIR analysis was conducted in this sample at the University of Oregon, giving a glass water concentration of $0.34\ wt.\%$, consistent with the STA analysis and the nanolite content of the material.

For the material Kb8, the Raman analyses represent good values of the water concentration. The error associated to these type of analyses ($\pm 0.16\ wt.\%$) represent a low value compared to the water concentration measured, which is 2.1 wt.%.

3.2.8 Electron microprobe analyses

Glass chemistry of the pre-experimental material (reported in Table 3.1) was acquired using a Cameca SX100 electron microprobe analyser (EMPA) at LMU Munich. Analyses were acquired using a $10\ \mu m$ spot diameter, an accelerating voltage of $15 kV$ and electron beam current of $5\ nA$. Counting times were between 6 and $30\ s$ depending on the mobility of analysed elements and the half times for peaks and background.

3.2.9 Magnetic hysteresis

Magnetic hysteresis analyses were conducted with a Variable Field Translation Balance (VFTB) at LMU Munich. The analyses were carried out at room temperature in cylindrical cores of 5 mm-diameter and 3 mm-length of the natural obsidian and the Kb2 synthesis, in order to check the magnetic increment as a result of the presence of Fe-Ti oxides

nanolites in the Kb2 material respect to the natural one. The analyses in both samples was conducted at the same conditions with applied fields between $-0.942 - 0.944\ T$.

3.3 Experimental methods

3.3.1 The optical dilatometer

The optical dilatometer is a device comprising three main parts: a light source, a furnace and a camera (Fig. 3.4A). The light source consists of a halogen lamp that emits a light toward the furnace. The furnace contains a removable alumina tube where the sample is located on a mobile carriage that holds a lid with a window, allowing the light to enter from one side into the tube. At the other side of the furnace there is an outlet window that allows the light to exit the tube zone in the furnace. The carriage consists of the lid and an S-type thermocouple on which a sample is placed on an alumina plate. The camera receives the light that is emitted in the light source and travels through the tube in the furnace.

While operating, the sample located in the tube partially blocks the pass of light, creating a sample shade that is recorded with the camera in an image. The image is then converted into binary (Fig. 3.4B-C), i.e. black and white, and the in-build software recognizes and records the sample dimensions and stores an image when required, according to the acquisition program. The three parts are connected together to a computer that controls precisely heating, isothermal hold or cooling from a specific temperature, depending on the aimed experimental conditions. During the process, many parameters are recorder such as time, furnace and sample temperatures, sample contact angles, sample height, sample base and sample transactional area. The data can be acquired in high and low frequencies, allowing to monitor in real time the conditions and geometry changes in the sample.

For this device, sample temperatures up to $\sim 1400\ ^{\circ}C$ were reach at heating rates between 0.1-60 $^{\circ}C\ min^{-1}$ and cooling rates between $0.1 - 50\ ^{\circ}C\ min^{-1}$. In this thesis, I am interested in precisely control the cooling rate of a magma portion in a crucible from high temperature and in obtaining the volume changes of cylindrical samples while heating or holding temperature. For different cases, the way this device is applied is explained in the specific chapter according to different purposes.

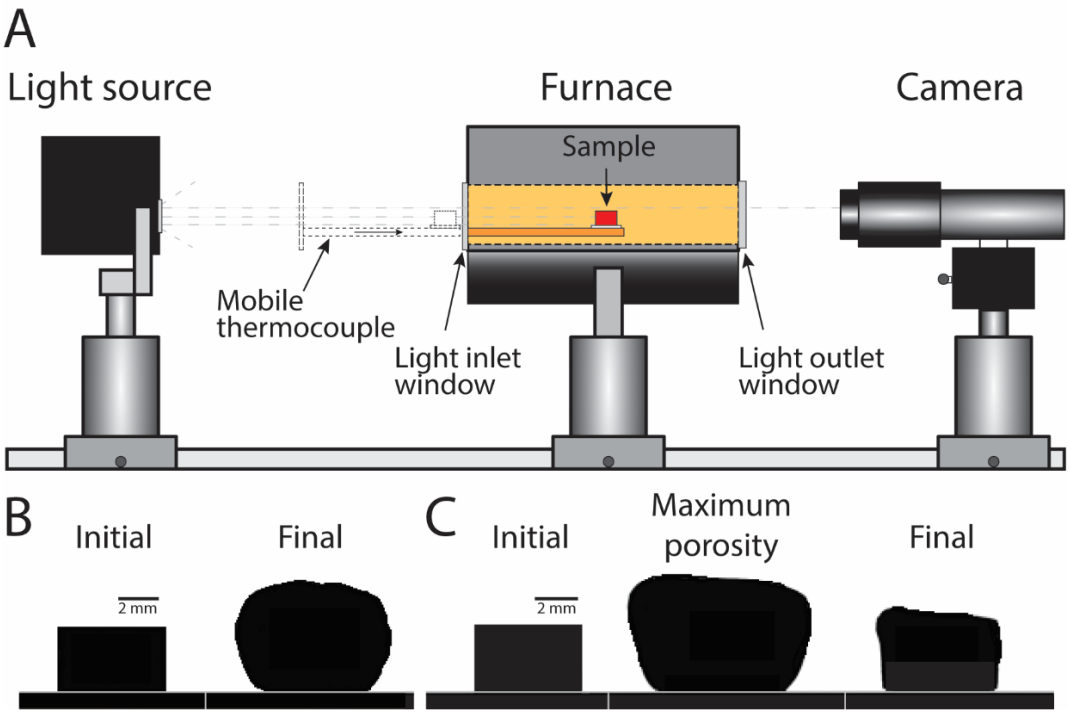

Figure 3.4. Optical dilatometer. Optical dilatometer and images acquired. (**A**) Sketch of the main parts of the optical dilatometer consisting on a light source, a central furnace and a camera. Sample is located on a mobile thermocouple that is introduced into the furnace and light enters the furnace through a window, passes along the ceramic tube and leaves the furnace through another window to reach the camera. The sample blocks the light producing a shadow that is recorder by the camera as shown in B and C. (**B**) Sample images recorder by the optical dilatometer at the beginning and the end of the heating program for samples that reach equilibrium porosity. (**C**) Sample images (as in **B**) recorded at the beginning, during and the end of the heating program for samples that shrank after outgassing. Here the samples reach a maximum porosity and then deflate to a lower final porosity.

In order to convert the data acquired by the optical dilatometer into a porosity value, I applied the following equation in order to covert the measured area of the sample into volume by calculating the volume of a cylinder with equivalent area and height:

$$V = \pi h \left[\frac{\left(\frac{A}{h}\right)}{2}\right]^2 \quad (1)$$

where V is the volume of the sample, A is the area captured by the optical dilatometer and h in the height of the samples captured by the optical dilatometer. The area and height of the sample represent precise measurements in the optical dilatometer. Then, the porosity Φ is calculated at every point applying the following equation:

$$\Phi = 1 - \frac{V_i}{V} \quad (2)$$

where $\emptyset$ is the porosity, V_i is the initial referential volume and V is the volume at each time.

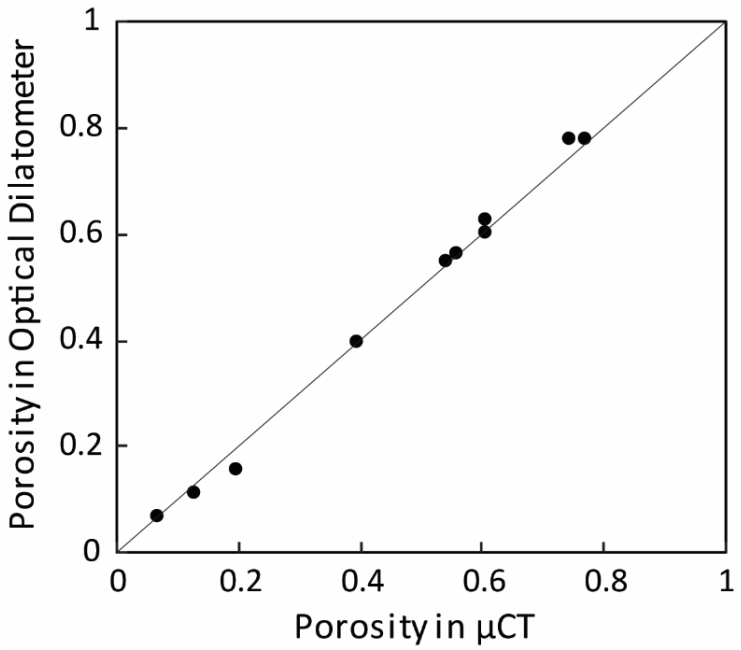

Figure 3.5. Porosity comparison between optical dilatometer and computed tomography. Both methods give a standard deviation of ~0.02 representing a ~2% sample vesicularity that is considered as the error for the porosity measurement with equations 1 and 2.

This method for obtaining porosity has been compared to the porosity measured with the computed tomography, which is a good reliable value obtained with a non-destructive method. The comparison was made for several post-experimental products of rhyolitic samples covering a porosity range between $0.06 - 0.77$, giving a standard deviation of ± 0.019 ($\sim 2\%$ vesicularity) that is considered to be the error associated to the optical dilatometer according to this way of obtaining it. The comparison is then shown in Figure 3.5.

From the porosity, it is possible to estimate the average bubble radius using an input of the bubble number density of the sample. This is assuming a monodisperse distribution of the bubbles and it can be calculated as:

$$r = \left(\frac{\Phi}{\frac{4}{3}\pi N_b (1-\Phi)} \right)^{1/3} \quad (3)$$

Where r is the bubble redius, Φ is the porosity, and N_b is the bubble number density. This method has been previously used for estimations of the bubble size during decompression (e.g. Cassidy et al., 2018).

3.3.2 The decompression autoclave

This experimental apparatus (Fig. 3.6) consists of a NIMONIC® autoclave, a thermocouple system, a pressurised gas inlet/outlet system and an external furnace. The sample is placed from the open top part of the autoclave in a stainless steel sample holder that is gently lowered with a rod inserted from the bottom of the autoclave until approximately two thirds of the high of it, where the inner diameter decreases and the sample holder stays at final position.

The thermocouple system consists of a K-type thermocouple sealed-welded inside a stainless steel rod of the same diameter as the autoclave bottom hole. The rod was then sealed-welded to a small closing nut that holds a copper ring that serves as sealing between the contact of the autoclave and the entire thermocouple system. This thermocouple system in inserted from the bottom of the autoclave, where it reaches the sample holder. This sample holder has a 1 mm-diameter hole at the base, allowing the thermocouple to directly monitor the temperature of the sample at less than 1 mm distance form it. This thermocouple system, once inserted from the bottom of the autoclave, is compressed against the autoclave with a compressive closure assembly through screws.

In the upper part, the system is sealed with a diaphragm system that remains unbroken during the complete experiment. Pressurised argon gas is then inserted at pressures of $\sim$100 bar controlled with a gas inlet valve and measured with a pressure transducer placed next to the gas entrance at the top of the autoclave. Additional pressurised argon gas is inserted in a small pressure chamber at the top of the autoclave, that divides pressure hold by the diaphragms into two. After reaching the initial gas pressure in the autoclave, the valve is closed and the system is gas tight. The autoclave is then externally heated by the surrounding furnace and the inner temperature and pressure are monitored with the thermocouple and pressure transducer. The

outer autoclave temperature is also monitored with an additional K-type thermocouple in direct contact with the external surface of the autoclave.

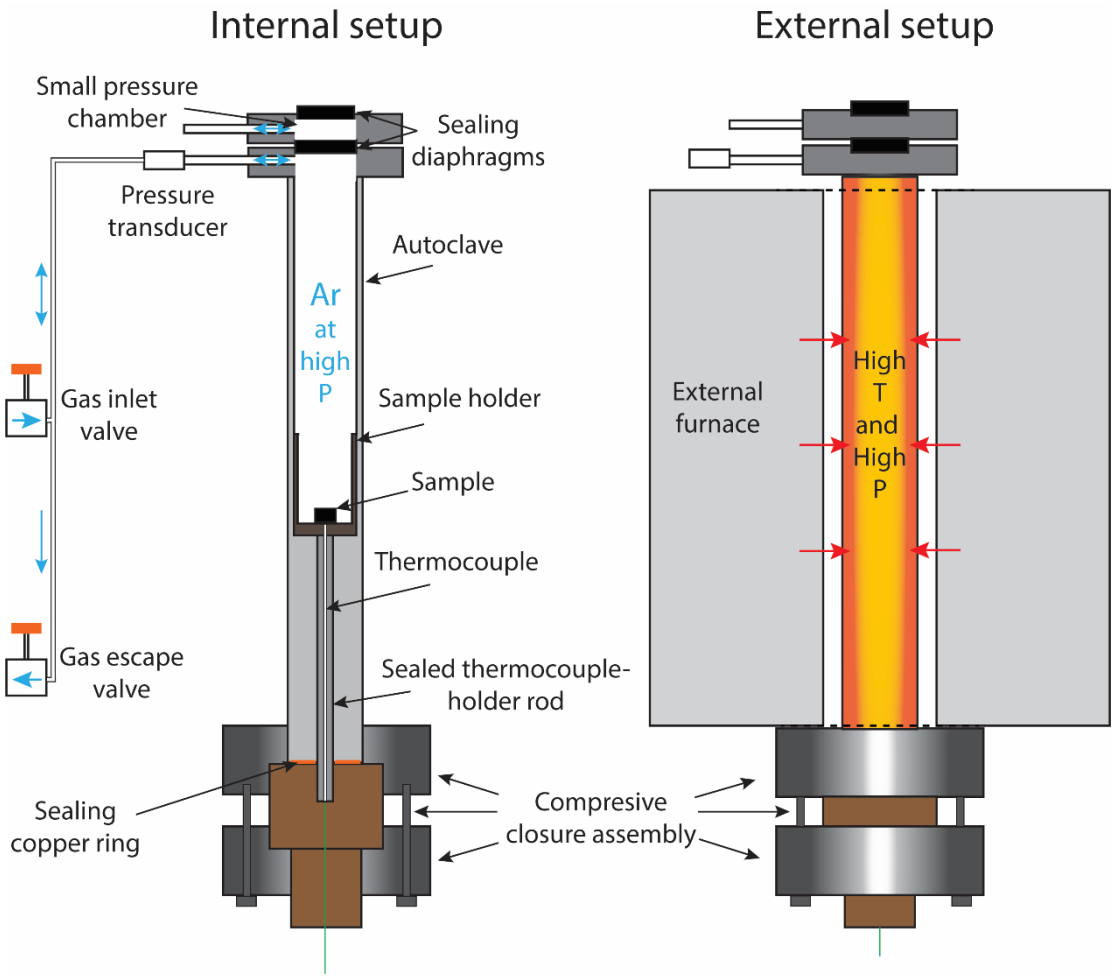

Figure 3.6. Decompression autoclave apparatus. Consists of a sealed autoclave were the sample is placed inside in a sample holder with a basal hole that allows the thermocouple to directly monitor the temperature at $< 1\ mm$ distance from the sample. The pressure is raised by introducing argon gas through the gas inlet valve and by increasing the temperature externally with a surrounding furnace. The pressure is monitored with a transducer and is controlled with the gas escape valve after closing the inlet valve. All the system is gas tight. Ar gas fluxes are presented in blue arrows.

The final internal pressure is reached by heating the autoclave with the furnace, which increases the gas temperature and hence the gas pressure inside the autoclave. The excess of pressure is released by opening the gas escape valve in order to maintain a stable pressure during heating until reaching the targeted conditions for the experiment.

After reaching the targeted conditions, the decompression is manually controlled by releasing gas with the gas escape valve. The decompression rate is made linear or non-linear. The linear

decompression is controlled with a sound chronometer previously programmed to emit a sound every specific lapse of time, while the pressure is continuously released at the rate of the chronometer, coordinating a pressure drop to the time lapse. The non-linear decompression is controlled by opening the gas escape valve once a specific amount, controlled by grading marks on the valve, and left releasing the gas until a final targeted pressure.

In this thesis, I am interested in precisely control the decompression rate at which a magma is subjected. For this, cylindrical samples of the synthesised materials are placed into the setup and heated to magmatic temperatures between $775 - 875\,°C$ and pressures equivalent to shallow magma ($\leq 35\,MPa$). The specific decompression rates and the samples used are explained in detail in the specific chapter.

3.4 Post-experimental sample preparation and analyses

After experiments, the resultant samples were again analysed with the different methods explained above, but with slight variations according to the differences between pre- and post-experimental samples type. Here I explained the procedure applied for the different samples type according to the experimental procedure followed.

3.4.1 Vesiculation in the optical dilatometer

The sample cylinders subjected to high temperature in the optical dilatometer for vesiculation experiments were weighted immediately after every experiment and stored in sample container with a small piece of paper to avoid hard contact between the sample and the container and eventual sample fracturing or damaged produced by mechanical abrasion. Selected samples were cut-opened with a fine wire saw ($\sim 200\,\mu m$) and mounted into epoxy resin for SEM and Raman analyses. After resin application, the submerged sample was placed into vacuum chamber to allow the resin to penetrate in the porous network and remove the air from the porous as much as possible, and then the samples into resin were left to dry for $\sim 48\,hours$. After drying, the samples were polished, cleaned and dried following the procedure mentioned in the last sections.

Raman analyses were then conducted in selected samples in order to check for nanolites presence or absence in the post-experimental materials and compared them with the pre-experimental ones. For this, Raman spectra were acquired in the $100 - 1500\ cm^{-1}$ region at the conditions mentioned before for the pre-experimental materials.

SEM images were acquired in the post experimental samples in order to check for bubble textures. Porosity and bubble number density was measured of selected smaples. For the latest two purposes, I binarized the SEM images (i.e. black and white) and then I performed the analyses with the software FOAMS (Shea et al., 2010a).

3.4.2 Magma cooling in the optical dilatometer

The samples subjected to high temperature and controlled cooling rate in the optical dilatometer were recovered and drilled out of the Pt_{80}-Rh_{20} crucibles as explained in the drilling section. This, in order to perform Raman and SEM analyses. The cores obtained were then cut with the wire saw and two pieces were separately mounted into resin. Subsequently, the mounts were polished and cleaned following the procedures explained in the pre-experimental sample preparation section.

The samples prepared for Raman was analysed for nanolite content at the same conditions as pre-experimental materials, by selecting at least 10 points randomly distributed in the sample area. On the other hand, the samples prepared for SEM analyses were imaged in order to picture the presence or absence of Fe-Ti oxide nanolites at the same conditions as the pre-experimental materials.

3.4.3 Vesiculation and fragmentation in the decompression autoclave

For the post-experimental samples of the decompression experiments, the procedure was the same as for the vesiculation experiments in the optical dilatometer. Since the vesiculation is higher in these samples driven by their higher initial water concentration, the impregnation of the porous network was more complex. In large samples, expoxy resin was added on the cut surface and the samples were put into vacuum to allow the resin to impregnated into the porous. After drying for 24 hours, these samples were mounted according

to the normal procedure. An additional layer of resin had to be added in some cases after the 48 hours drying of resin, in order to fill remaining void spaced.

In case of fragmentation of the sample, collection of the fragments was done by turning the sample holder onto a white piece of paper and then put into a glass sample container. The impregnation of the fragmented samples was made using fragmented pieces only following the normal procedure..

3.4.4 X-ray Computed Tomography (CT)

Selected post-experimental samples were analysed with X-ray computed tomography (CT). The analyses were performed in a GE-Instruments™ Phoenix Nanotom-M device at the Zoology State Collection Munich, Germany. Using in-built analysis functions in Avizo™, textural observations and analyses of porosity and bubble number density were made.

This is a powerful and non-destructive method that allows to obtain images of the interior of samples at a maximum spatial resolution of 200 nm per voxel edge, depending on the operating conditions and the distance between the source and the detector. However, the interplay between image contrast and measurement time did not allow to reach resolutions higher than approximately 2 μm. Additionally, to properly resolve the images for reliable bubble texture analyses, a minimum size of the analysed object of about four times the spatial resolution reached is needed (considering error minimization). This means, to properly analyse the images, inter-bubble glass films in the order of 8 μm as minimum are required, which is not possible to have in a representative volume in, for example, the nanolite-bearing samples as it can be seen in the Figure 4.2D (Chapter 4). However, other textural analyses as well as porosity and bubble number density measurements were performed in samples were inter-bubble films could properly be resolved.

4

The effect of nanolites on magma degassing and implications for eruption explosivity

Chapter Summary

The degassing dynamics play a crucial role in controlling the explosivity of magmas in volcanic systems. Degassing of magmatic water typically involves nucleation and growth of water-rich bubbles, which increases magma buoyancy and, in turn, drives magma ascent. The crystal cargo of the magma is generally believed to play a central role influencing these processes. Both mm-scale phenocrysts and micron-scale microlites are known to cause heterogeneous bubble nucleation and to facilitate bubble coalescence. However, nanometer-scale crystalline phases, so-called "nanolites", are a widespread yet underreported phenomena in erupting magmas and they are hypothesised to exert a primary control on the eruptive style of silicic volcanoes. Yet the influence of nanolites on bubble-hosted degassing processes remains wholly uninvestigated. In order to test the influence of nanolites on gas bubble nucleation and growth dynamics, in this chapter I use an experimental approach to document how nanolites can increase the bubble number density in a degassing silicic magma. I then inspect a compilation of bubble number densities from natural volcanic rocks from explosive eruptions and infer that some very high naturally-occurring bubble number densities could be associated with the presence of magmatic nanolites. Finally, using a numerical magma ascent

model, it is shown that for reasonable starting conditions for silicic eruptions, an increase in the resulting bubble number density associated with nanolites could push an eruption that would otherwise be effusive into the conditions required for explosive behaviour.

4.1 Samples used and experimental conditions

Here I used two materials to conduct the bubble-growth experiments. The first one, the iron-rich (Table 3.1) nanolite-free rhyolite obsidian (Figs. 3.1A, 4.2A) from Hrafntinnuhryggur eruption of Krafla volcano in Iceland (see Chapter 3 for details). The second one, the synthesised nanolite-bearing sample Kb2 (Figs. 3.1B, 4.2B) of the same rhyolitic composition (see Table 3.1).

Cylinders of 5 mm diameter and 3 mm height of both materials were mounted into the optical dilatometer, then heated at controlled heating rates and kept at final temperature for dwell times of 8 $hours$. The heating rate applied was 30 $°C\ min^{-1}$ to isothermal dwells at $820 - 1000\ °C$. The real-time sample area and shape were recorded as they crossed the glass transition. Increases in the recorded sample area were transformed to porosity values according to equations 1 and 2 (Fig. 4.1). The experimental products for the two sample types were then analysed (see Chapter 3) and compared.

Additionally, five experiments were conducted without a dwell time at final temperature. These experiments were conducted at heating rates of $1 - 60\ °C\ min^{-1}$ up to a final temperature of $850\ °C$ and then fast quenched in air by removing the sample from the optical dilatometer.

4.2 Bubbles textures, number densities and groundmass characteristics

Using run-products for experiments that reached equilibrium porosity and bubble size, it is determined that for the natural obsidian, the bubble number density produced during the experiments range $10^{-1} \leq N_b \leq 10^{1}\ mm^{-3}$ (Table 4.1), with final bubble sizes between $0.2 \leq R_b \leq 1.5\ mm$ (Fig. 4.2C). On the other hand, for the re-melted, nanolite-bearing samples, the bubble number densities were much higher in the order of magnitude between

$10^6 \leq N_b \leq 10^7\ mm^{-3}$ (Table 4.1) and with significantly smaller final bubble sizes that range $10^{-3} \leq R_b \leq 10^{-1}\ mm$ (Fig. 4.2D).

Porosities of the post-experimental nanolite-bearing samples range $0.15 - 0.78$, while the porosities for the nanolite-free sample range $0.4 - 0.65$. These values of bubble number density and bubble size obtained here for the natural, nanolite-free obsidian, are consistent with experiments carried out with samples of the same composition and at similar experimental conditions by Ryan et al. (2015).

Both post-experimental materials preserve their original nanolite-free or nanolite-bearing characteristic, as well as their microlite content. However, nanolites in the nanolite-bearing samples grew from their original pre-experimental size to an average of $200\ nm$ without changing the phases involved. This can be confirmed comparing the Raman spectra acquired in the pre- and post-experimental material for which an example is presented in Figure 4.2G.

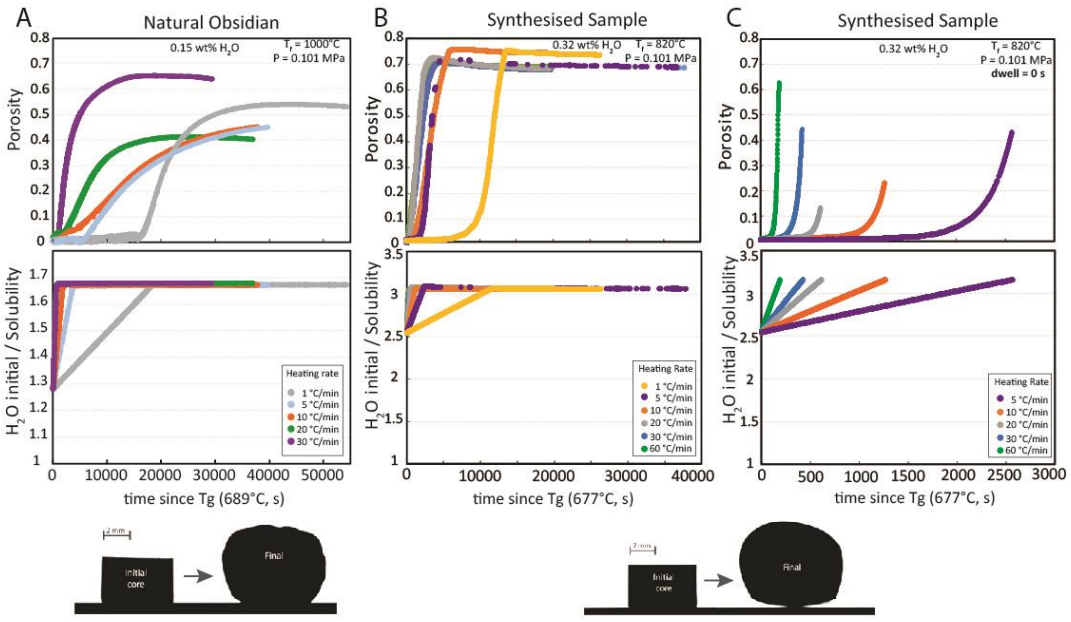

Figure 4.1. Real time vesiculation profiles for: (**A**) natural (nanolite-free) and (**B-C**) synthesised (nanolite-rich) samples, together with the evolution of the ratio of the initial H_2O concentration and the H_2O solubility. Initial H_2O is measured value from STA analysis (see Chapter 3), and the H_2O solubility is computed using Liu et al. (2005) solubility model valid for rhyolites and for which 1 bar pressure was input. (**C**) Represents experiments conducted with only a heating phase (without dwell time at maximum temperature). Bottom silhouette images represent the sample images acquired from the optical dilatometer at the beginning and end (final porosity) of the heating program of a representative sample of each kind, from which volumes are computed continuously

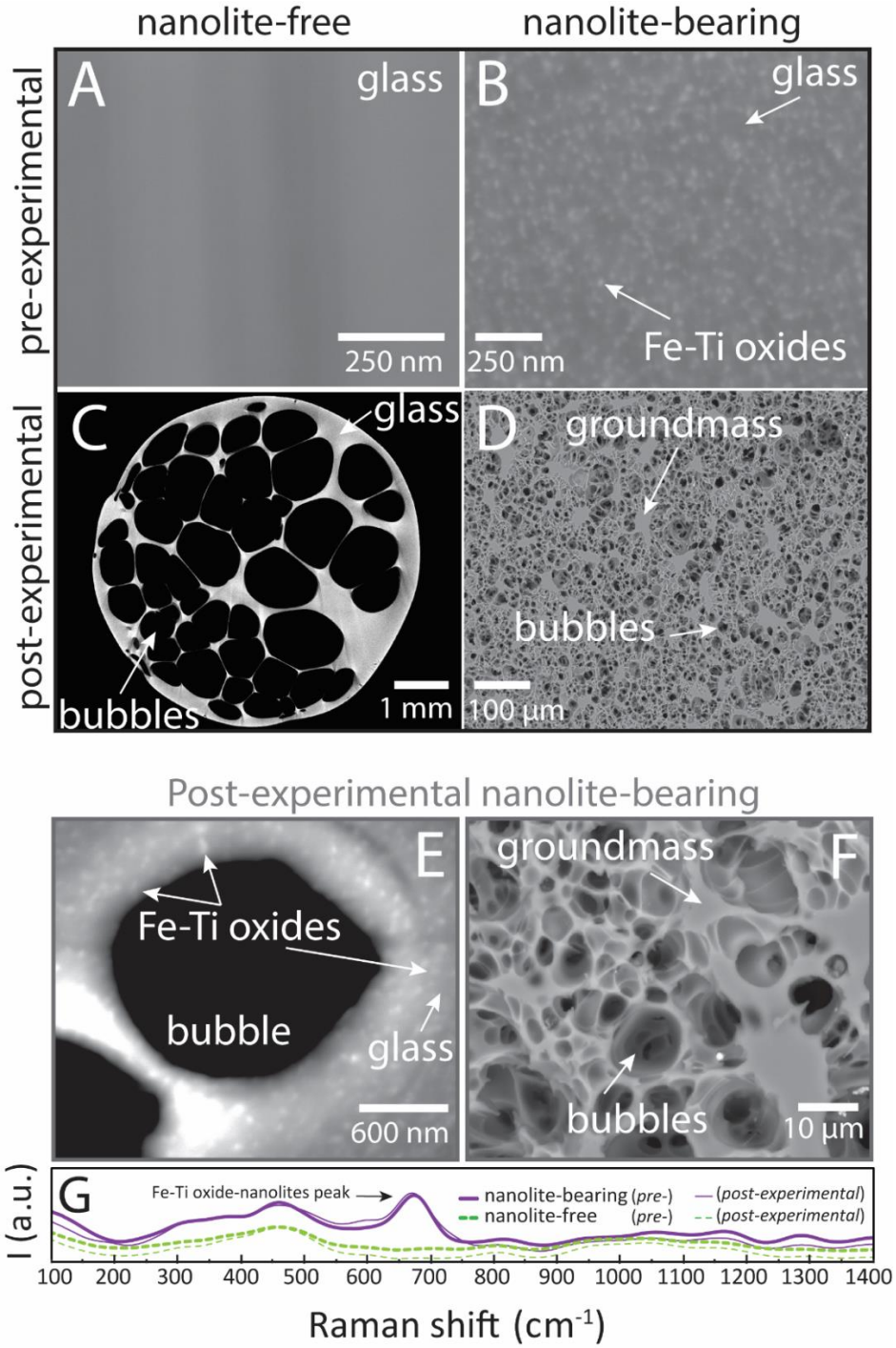

Figure 4.2. Comparison between pre- and post-experimental samples. (A) Back-Scattered Electron (BSE) SEM image of pre-experimental natural obsidian showing nanolite-free glass. (B) BSE-SEM image of pre-experimental nanolite-bearing sample containing a high crystal number density ($\sim 10^{12}\ mm^{-3}$). (C) X-ray Computed Tomography (CT) image of post-experimental nanolite-free sample showing high vesicularity (~60%) with low bubble number density ($\sim 10^{0}\ mm^{-3}$). (D) BSE-SEM image of post-experimental nanolite-bearing sample with high vesicularity (~70%) and a high bubble number density ($\sim 10^{7}\ mm^{-3}$). (E) Zoom to post-experimental nanolite-bearing sample and nanolite-bubble coexistence. (F) Zoom to bubbles and interstitial groundmass (nanolites + glass) in post-experimental nanolite-bearing sample showing bubble interaction and sizes. (G) Raman spectra for nanolite-free and nanolite-bearing samples pre-and post- experimental. The Fe-Ti oxide nanolites peak ($\sim 670\ cm^{-1}$) is pointed with an arrow.

Table 4. 1. Bubble number densities for experimental conditions.

Sample name	Sample type	Heating rate (°C min^{-1})	Dwell temperature (°C)	Nb^{A} (mm^{-3})	Nb^{B} (mm^{-3})
Kb2-OD-03	nanolite-bearing	20	1000	5.95 x 10^{6}	-
Kb2-OD-06	nanolite-bearing	30	850	5.58 x 10^{7}	-
Kb2-OD-14	nanolite-bearing	30	845	8.06 x 10^{7}	-
Kb2-OD-15	nanolite-bearing	5	820	8.46 x 10^{6}	-
Kb2-OD-16	nanolite-bearing	10	820	1.79 x 10^{6}	-
Kb2-OD-18	nanolite-bearing	1	820	5.33 x 10^{6}	-
Kb2-OD-20	nanolite-bearing	60	820	1.48 x 10^{7}	-
Kb2-OD-21	nanolite-bearing	30	820	2.45 x 10^{7}	-
Ka-OD-02	nanolite-free	30	950	-	1.47 x 10^{1}
Ka-OD-03	nanolite-free	30	1000	-	7.90 x 10^{0}
Ka-OD-04	nanolite-free	30	975	-	6.51 x 10^{0}
Ka-OD-08	nanolite-free	5	1000	2.39 x 10^{0}	-
Ka-OD-10	nanolite-free	20	1000	8.64 x 10^{-1}	-
Ka-OD-14	nanolite-free	1	1000	5.97 x 10^{0}	-
Ka-OD-17	nanolite-free	30	1000	-	1.52 x 10^{0}
Ka-OD-19	nanolite-free	10	1000	-	1.63 x 10^{-1}

[A] N_b melt corrected measured with FOAMS (Shea et al., 2010) from 2D SEM-BSE images.

[B] N_b melt corrected measured with Avizo^{TM} from 3D CT reconstructions.

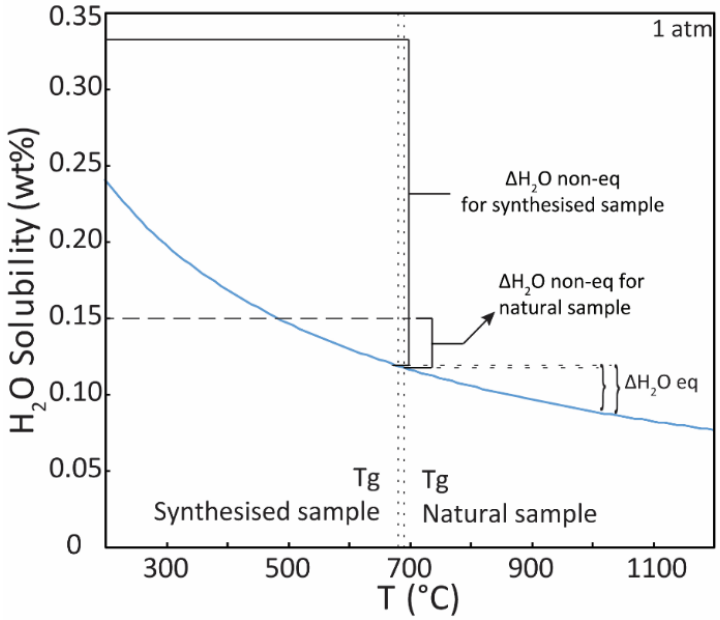

Figure 4.3. Water solubility curve for rhyolitic magmas at 1 atm. Vertical dotted lines show the glass transition temperature (Tg) for both the synthesised samples and the natural obsidian. Gray keys show the water exsolved (Δwt% H_2O) in equilibrium conditions dependent of the final temperature. Black keys show the supersaturation level and hence the amount of water exsolved in non-equilibrium conditions after crossing Tg during heating. Solubility model of Liu et al. (2005). Viscosity model of Hess and Dingwell (1996).

4.3 Bubble growth rates

During heating, both materials experienced a small thermal expansion of less than 1 vol.% before crossing the glass transition temperature (Tg; ~689 °C for the natural obsidian and ~677 °C for the synthesised sample), followed by a non-linear accelerated expansion, steady expansion and finally a decelerated expansion until reaching an equilibrium state during dwell time at final temperature (Fig. 4.1)

The ultimate driving force of oversaturation-driven nucleation and growth of water-rich bubbles is the temperature-, composition- and pressure dependent water solubility of the melt phase (Liu et al., 2005). In these experiments, the expansion after Tg is purely produced by growth of water-rich bubbles driven by water exsolution from the melt when heating decreases water solubility during the experiments. In order to study the volume change driven by bubble growth, the small thermal expansion was subtracted and only the expansion driven by porosity increase was considered.

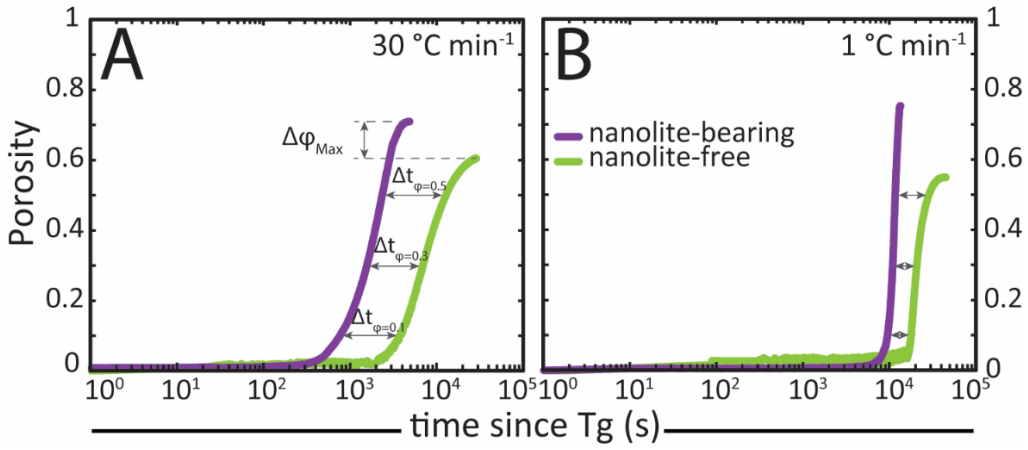

Figure 4.4. Experimental profiles of real time porosity evolution for nanolite-free (green) and nanolite-bearing (purple) samples: (**A**) 30 $°C\ min^{-1}$ and (**B**) 1 $°C\ min^{-1}$ heating rates. Glass viscosities (η) and water diffusivities (D) were calculated using the models of Hess and Dingwell (1996) and Zhang and Ni (2010) respectively. Nanolite-free samples were heated up to 1000 $°C$ ($\eta \sim 10^{7} Pa.s, D \sim 6x10^{-13} m^{2} s^{-1}$) and nanolite-bearing samples was heated up to 820 $°C$ ($\eta \sim 10^{9} Pa.s, D \sim 2x10^{-13} m^{2} s^{-1}$). Even at 180 $°C$ lower, the nanolite-bearing samples expands more quickly compared to the nanolite-free ones. The time difference when sample pairs reached 0.1, 0.3 and 0.5 porosity values is shown as reference (grey arrows). Profiles are shown starting from the point when samples cross the glass transition temperature. Water solubility at 820 and 1000 $°C$ is computed according to Liu et al. (2005).

For experiments conducted at the same heating rates, the nanolite-bearing sample always began expanding significantly earlier and with a higher resultant expansion rate than the nanolite-free sample (Fig. 4.4). While the two sample types (nanolite-free and -bearing) had subtly different initial water concentrations, it is assumed that the discrepancy in onset time and expansion rate (bubble growth) cannot be attributed to this small difference in starting water content, even if the supersaturation of water is higher (Fig.4.3).

To justify this, it is noted that even when comparing conditions where the calculated melt viscosity is higher and water diffusivity is lower in the nanolite-bearing sample (Fig. 4.4), the growth rates were more rapid. The increase in crystal content can only increase the viscosity (e.g. Costa 2005), producing more resistance for bubble growth. Instead, this gap between the two sample types is attributed to the difference in their nucleated bubble number density.

4.4 Bubble number densities and nanolites in natural products

The number density of homogeneously nucleated bubbles (N_b) during degassing of an ascending magma is dominantly controlled by the decompression rate (e.g. Toramaru 2006; Shea 2017). However, heterogeneous nucleation may decrease the decompression rate needed to produce the same N_b by orders of magnitude (e.g. Cluzel et al., 2008; Hamada et al., 2010; Shea 2017). High N_b ($\sim 10^7\ mm^{-3}$) in natural silicic explosive products (e.g. 7.7 ka BP Mt Mazama eruption; Klug et al., 2002) have been attributed to combination of fast decompression rates and the presence of relatively high ($10^0 - 10^2\ mm^{-3}$) crystal number densities during degassing (e.g. Hamada et al., 2010), with an emphasis on the additional role played by decompression (or ascent) rates. The data suggest that the nucleation of nanolites in magmas could result in high bubble number densities and associated high bubble growth rates in situations where nanolites grow below or in the kinetic window of bubble nucleation. This implies a possibility of reaching high bubble number densities by heterogeneous nucleation of bubbles on nanolites even at relatively lower decompression rates.

To show the general relevance of this form of nanolite-driven heterogeneous nucleation, I compiled published estimates of bubble number density ranges in natural products of explosive eruptions from a wide range of magmatic compositions (Fig. 4.5A). These data show that across a wide range from intermediate to high silica magma compositions, mean N_b tend to be around $10^5 - 10^6\ mm^{-3}$, with maxima at $> 10^8\ mm^{-3}$ (Fig. 4.5C; similar to data compiled

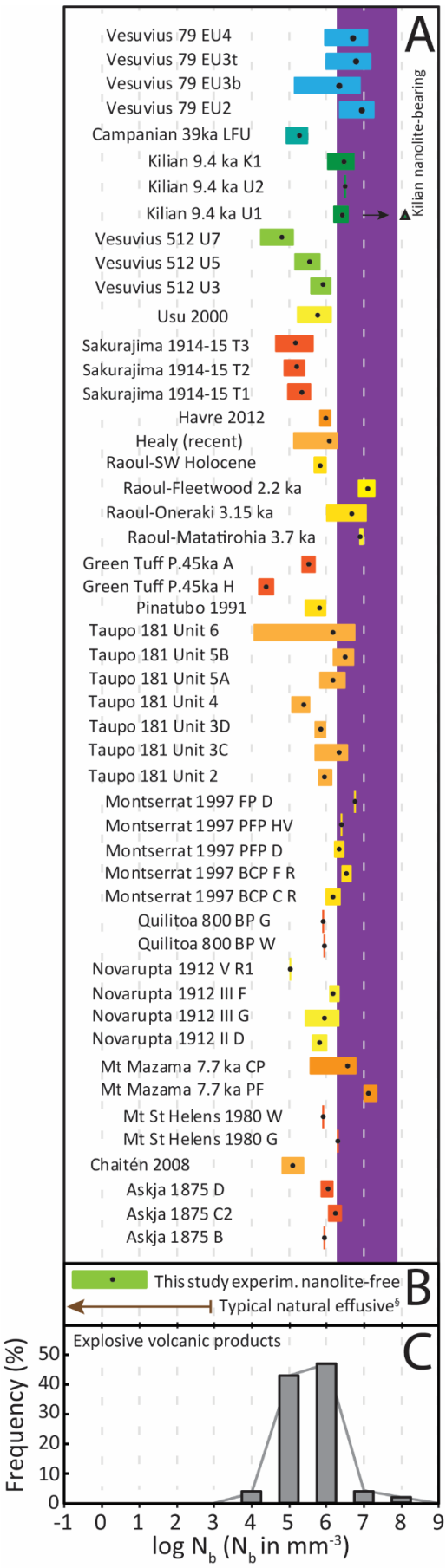

Figure 4.5. Bubble number density (N_b) of the products of explosive volcanic eruptions and effusive products as reference. (**A**) N_b recorded in clasts from different phases or units of an eruption with minimum and maximum reported values where black dots show the mean value. Colors denote glass composition: orange and yellow for rhyolitic, green for trachytic and blue for phonolitic. Color are attributed based the composition of the glass only. The purple region shows the experimental range for the nanolite-rich samples in this study. For Kilian U1, area and dot show the range and mean value without nanolites and black triangle shows the value with nanolites. (**B**) Range for nanolite-free experimental samples in this study (green) and typical natural effusive. § Referential range for varied (basaltic, trachytic and rhyolitic) effusive products. (**C**) The frequency distribution of N_b mean values for which more than 80% of the data fall in the range of $10^5 - 10^6\ mm^{-3}$. Eruptions included are: Vesuvius 79 (Cioni et al., 1995; Gurioli et al., 2005; Shea et al., 2010; Shea et al., 2012;); Campanian (Polacci et al., 2003; Shea 2017); Kilian 9.4 ka (Colombier et al., 2017b); Vesuvius 512 (Cioni et al., 2011); Usu 2000 (Suzuki and Nakada 2002); Sakurajima 1914-1915 (Nakamura 2006); Havre, Healy and Raoul-SW (Rotella et al., 2015); R-Fleetwood 2.2 ka, R-Oneraki 3.15 ka and R-Matatirohia 3.7 ka (Barker et al., 2013; Rotella et al., 2014); Green Tuff Pantelleria 45 ka (Lanzo et al., 2013; Campagnola et al., 2016); Pinatubo 1991 (Rutherford and Devine 1996; Polacci et al. 2001; Shea 2017); Taupo 181 (Stokes et al., 1992; Houghton et al. 2010); Montserrat 1997 (Harford et al., 2003; Giachetti et al. 2010); Quilotoa 800 BP (Rosi et al., 2004; Stewart and Castro 2016); Novarupta 1912 (Fierstein and Hildreth 1992; Coombs and Gardner 2001; Adams et al., 2006a); Mt. Mazama 7.7 ka (Bacon and Druitt 1988; Klug et al., 2002); Mt. St. Helens 1980 (Klug and Cashman 1994; Blundy and Cashman 2005); Chaitén 2008 (Alfano et al., 2011; Alfano et al., 2012) and Askja 1875 (Sigurdsson and Sparks 1981; Carey et al., 2009); Effusive range (Cáceres et al., 2018; Colombier et al., 2017b; Degruyter et al., 2012; Giachetti et al. 2010; Shea et al., 2010a).

Shea 2017). I note that the bubble number densities produced in the nanolite-bearing samples are in the high range ($\geq 10^6\ mm^{-3}$) of bubble number densities found in natural explosive products. For comparison, data for N_b in intermediate to silicic effusive eruptions are sparse, but typical values are lower than $10^3\ mm^{-3}$ (Fig. 4.5B).

Nanolites are not widely reported in volcanic erupted products, and therefore the subset of this compilation for which nanolites have been identified is low. Nanolites of Fe-Ti oxides have been observed to be present in the reduced melt fraction of a phenocryst- and microlite-bearing fragment explosively ejected in an eruptive transition from a lava dome at Kilian volcano, France (Colombier et al., 2017b; Fig. 4.6). These nanolite-bearing products have an N_b up to two orders of magnitude higher than the nanolite-free products of the same eruption (Fig. 4.5A). In the case of the 2011 Shinmoedake eruption, Japan (Mujin and Nakamura 2014; Mujin et al., 2017), nanolites of low-Ca pyroxenes, plagioclase and Fe-Ti oxides are present in all the transition sequence from sub-Plinian to effusive eruptive style. Even though the nature of these nanolites differs to those in this study according to the different composition of the magmas involved, nanolites are present in the products of the first and most explosive phase of the eruption with N_n of $\sim 10^{13}\ mm^{-3}$, comparable to those in this study ($\sim 10^{12}\ mm^{-3}$).

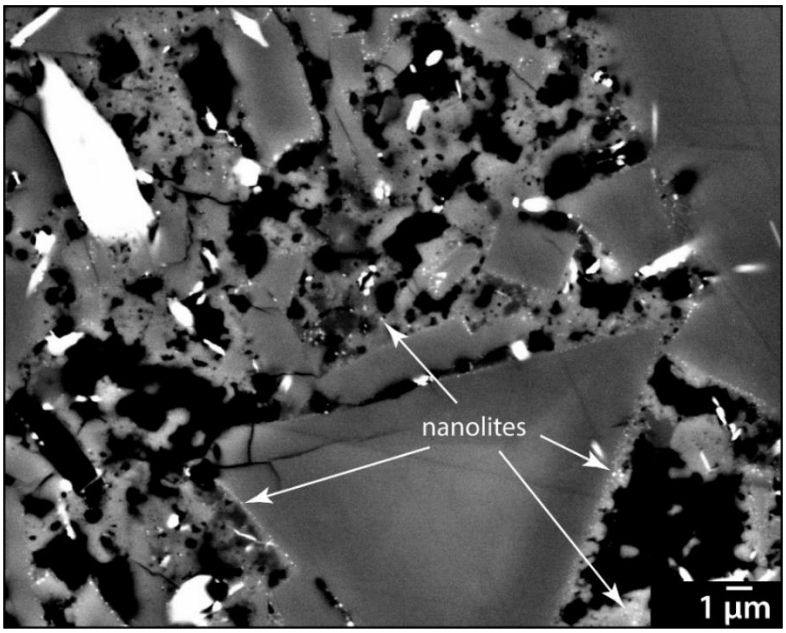

Figure 4.6. Sample from Kilian volcano (U1) with high N_b ($\sim 10^8\ mm^{-3}$) and nanolites. Modified after Colombier et al. (2017b).

This compilation of naturally-occurring bubble number densities (Fig. 4.5), along with the few observations that exist for the natural occurrence of nanolites suggest that nanolites may play

an important role in increasing the bubble number density relative to nanolite-free magma. This is consistent with the findings of the experimental work (Figs. 4.2 and 4.4). While here it is not meant to claim that this is the only cause of high bubble number densities, it can be argued that it is a process that plays a role in shallow magma ascent and cannot be neglected.

4.5 Application to high-silica magmas: Effusive or explosive eruptive style?

So far in this chapter, it has been experimentally established that silicic magmas that can form nanolites prior to bubble nucleation events are likely to results in high bubble number densities compared with magmas without nanolites. In a second step, it has been shown that these high experimental N_b values in nanolite-bearing melts are at the upper end of naturally-occurring ones, and that in the few available cases, nanolites have been found in erupted products of explosive eruptions increasing N_b. As a final step, it is aimed to use a reference magma ascent model to show what the effect of such an increase in bubble number density could be in ascending magmas. In doing so, the purpose is not to model heterogeneous nucleation of bubbles on nanolites explicitly, and instead use existing tools to build the case for the critical effect nanolites may have in an ascending magma.

Now, magma ascent in a conduit will be simulated using a one-dimensional two-phase model developed by Degruyter et al. (2012), that considers magma ascent and eventual permeable outgassing at high porosities. Although the model used works on the basis of equilibrium degassing and does not consider the mechanism (i.e. homogeneous or heterogeneous) and kinetics of bubble nucleation, it is suitable for investigating the effect that existing bubbles exert on the eruptive behavior of ascending magma in a volcanic conduit, since it predicts whether a magma will fragment during ascent or not, effectively showing whether an eruption could be effusive or explosive at the Earth's surface.

This model requires an input of N_b and initial bubble size, as well as conditions regarding the conduit dimensions, initial magma storage depth, temperature and initial water content. Conduit diameters of $10, 16$ and $20\ m$ are used as inputs, and magma starting conditions appropriate for a well-studied case such as the Chaitén 2008 eruption (Castro and Dingwell 2009): a 5-km-length conduit, initial reservoir pressure of $120\ MPa$, magma temperature of

$825\ °C$, initial water content $4.27\ wt.\%$ and an initial bubble size of $10^{-7}\ m$. Where not stated, default inputs from Degruyter's et al. (2012) model are used. This model is solved varying N_b, using the same range found in natural explosive products, also covering the range obtained experimentally for the nanolite-bearing sample in this study (Fig. 4.5A).

The simulations (Fig. 4.7 and 4.8) show that for a given range of common conduit dimensions, the range of N_b found in natural magmas ($10^4 - 10^8\ mm^{-3}$) can explain the difference between effusive and explosive eruptive style. Even if the conduit diameter seems to be a sensitive variable, at one eruption site with a given conduit geometry the increase in N_b associated with bubble nucleation on nanolites could result in a transition from effusive to explosive eruption (Fig. 4.7, dotted to solid lines respectively). These results are also consistent with low N_b and high N_b inferred for effusive and explosive eruptions respectively (e.g. Cluzel et al., 2008). Moreover, for the conduit diameters investigated, the range of N_b that appears to be associated with nanolites (purple bar in Fig. 4.5A), is sufficiently high to result in explosive volcanism in most of the studied scenarios.

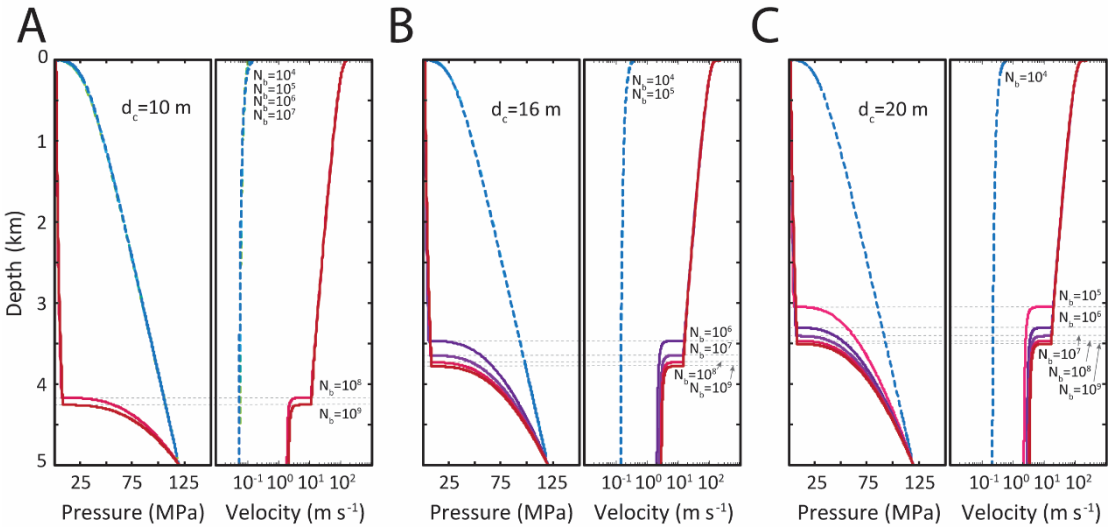

Figure 4.7. One-dimensional magma ascent model. The model of Degruyter et al. (2012) is applied, that considers magma ascent and outgassing. A 5-km-length conduit case is considered using the well-studied conditions for Chaitén 2008 eruption (Castro and Dingwell 2009) as input parameters: initial reservoir pressure $P_0 = 120\ MPa$, magma temperature $T = 825\ °C$, initial water content $C_0 = 4.27\ wt.\%$, initial bubble size $R_0 = 10^{-7}\ m$ (see Data Repository). The effect of bubble number densities is systematically explored in the range N_b of $10^4 - 10^9\ mm^{-3}$ on the evolution of pressure gradient, ascent velocity and initiation of fragmentation in a conduit of (**A**) $10\ m$, (**B**) $16\ m$, and (**C**) $20\ m$ diameter. Note that fragmentation is indicated by discontinuous jump corner in pressure-depth or velocity-depth curves. Fragmentation level is marked with grey dotted lines. For a given conduit diameter, an increase in N_b induces explosive behaviour. In (**A**) fragmentation is reached only for high N_b ($10^8 - 10^9\ mm^{-3}$). In (**B**) fragmentation is reached for N_b within the range produced for nanolite-bearing magma ($10^6 - 10^7\ mm^{-3}$) and higher. In (**C**) fragmentation starts at values of N_b most found in natural explosive volcanic products ($\geq 10^5\ mm^{-3}$) and covering the range found in the nanolite-bearing samples of this study ($10^6 - 10^7\ mm^{-3}$).

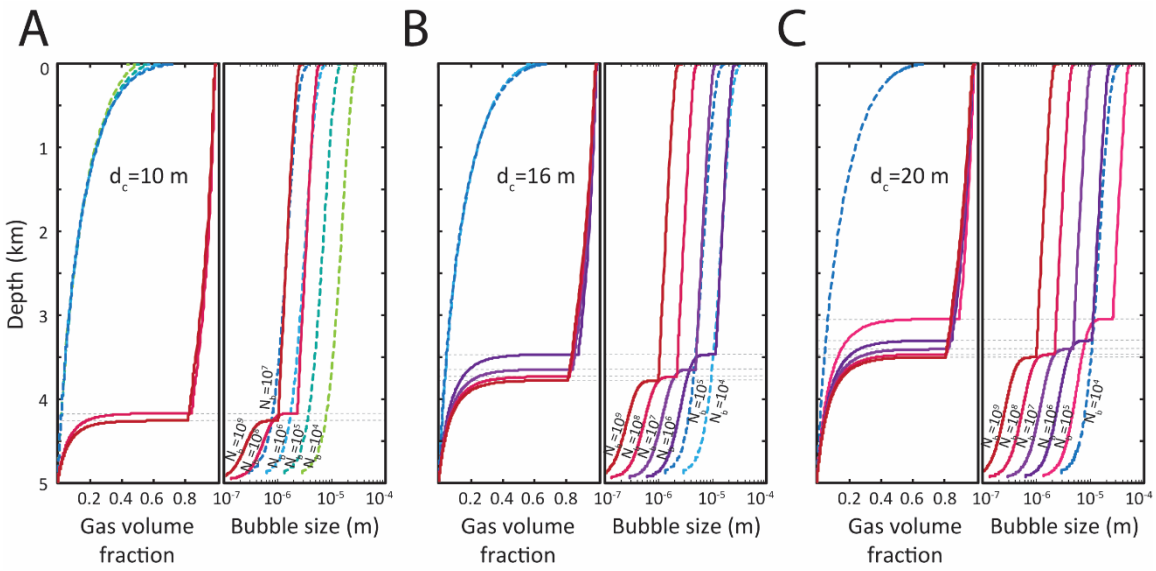

Figure 4.8. Gas volume fraction and bubble size evolution for a rhyolitic magma ascending in a conduit of: (A) 10 m, (B) 16 m, and (C) 20 m diameter. Results are shown varying bubble number density (N_b) between 10^4-10^9 mm^{-3}. Effusive eruptions are in dotted lines and explosive eruptions in solid lines. Fragmentation level is marked as a grey dotted line. Model used was that of Degruyter et al. (2012). For details of modeling see main text. Bubble size was calculated following equation 3 (see Chapter 3).

4.6 Concluding remarks

It has been shown that nanolites can be efficient sites for bubble nucleation leading to high bubble number densities and growth rates. An important observation about natural occurring textures is that high bubble number densities, such as those produced by nanolite-bearing samples in these experiments, are found in highly explosive natural volcanic products.

Combining these observations and numerical model results, it is proposed that nanolites may play a critical role in enhancing the propensity for eruptions to be explosive by accelerating the ascent of magma and deepening the fragmentation level of an ascending magma.

5

Conditions for Fe-Ti oxide nanolites crystallisation during cooling of shallow rhyolitic magma

Chapter Summary

Magma properties, such as viscosity and crystal content are of crucial importance to understand the behaviour of erupting volcanoes. The bulk viscosity of a magma is largely controlled by the viscosity of its silicate melt phase and its crystal load. Magma viscosity in turn exerts a primary control on the eruption style and its shifts between explosive and effusive. Magmas ascending to shallow levels are subjected to decompression that leads to volatile loss and melt viscosity increase as well as the nucleation and growth of microlites and nanolites. Yet the effects of nanolites on magma rheology have only been investigated to day in a reconnaissance fashion. In order to understand the effect of cooling on Fe-Ti oxide nanolites crystallisation and silicate melt structure, I conducted magma cooling experiments at highly controlled cooling rates between $0.1 - 50\ °C\ min^{-1}$. All experiments were run in air at atmospheric pressure conditions using with an Fe-rich rhyolitic magma at superliquidus starting conditions. I analysed the resultant glasses with a micro-Raman spectrometer to study the structural changes in the melt during the transition from a crystal-free melt to a nanolite-

bearing magma, as well as the process of nanolite crystallisation. The Raman spectra show that in the experiments, nanolites start forming at cooling rates of $0.5\ °C\ min^{-1}$ or lower concomitantly with an increase in melt polymerisation. The timescales for nanolite formation are estimated to range in the order of $10^4\ s$ for dynamic crystallisation and the same timescales are sufficient for isothermal crystallisation. The experimental results at oxidising conditions and slow cooling rate provide valuable insights into the formation of Fe-Ti oxide nanolites and structural changes of silicate melts in natural volcanic systems. Both, the higher degree of melt polymerisation and the higher load of crystals due to the formation of nanolites are likely to cause an increase in the magma viscosity, in addition nanolites provide sites for heterogeneous bubble nucleation in degassing magmas. In concert this bears the potential to shift shallow magmas from an effusive eruption style into conditions favourable for an explosive eruption.

5.1 Samples used and experimental conditions

For these experimental series, I used the rhyolitic (Table 3.1) natural obsidian from Hrafntinnuhryggur eruption of Krafla volcano in Iceland. It is worth to mention that it corresponds to a nanolite-free glass with $< 1\ vol.\%$ Fe-Ti oxide microlite content. A block of this obsidian was finely powdered down to $< 63\ \mu m$ particle diameter (as shown in Figure 3.2) and then dried at $80\ °C$ for $24\ hours$ before storing in an air tight container.

Experiments were conducted by melting in air at $1\ bar$ atmospheric pressure the fine obsidian powder in the optical dilatometer. For each experiment, a $6\ mm$-diameter and $6\ mm$-length Pt_{80}-Rh_{20} crucible was filled with $\sim 0.6\ g$ of the glass powder and pressed by manual force with a small piston in order to compact the powder. The crucible containing the sample is placed into the optical dilatometer on an alumina-covered S-type thermocouple that measures temperature with high precision ($\pm 2\ °C$). Before each experiment, the powder was heated for three hours at $245\ °C$ in order to eliminate any humidity acquired during storage. The crucibles were then heated to $1385\ °C$ at $30\ °C\ min^{-1}$ and held at that temperature for $3\ hours$, in order to produce a homogeneous crystal-free melt. After dwelling at $1385\ °C$, the melts were cooled down under precisely-controlled cooling rates between $0.1 - 50\ °C\ min^{-1}$ to a final temperature of $100\ °C$, then the furnace was turned off to cool freely to ambient room temperature ($\sim 23°C$). After experiments, the samples were drilled out of the centre of the Pt-Rh crucibles with a $2.5\ mm$ (inner diameter) diamond coring tool, obtaining $\sim 5\ mm$-length cores. The cores were precisely cut into $\sim 1.5\ mm$-length discs with a $200\ \mu m$-thick wire saw.

After cutting, two discs of each sample were mounted into epoxy resin for further analyses. All mounted samples were carefully polished down to 3 μm particle diamond paste in order to generate a smooth surface that serves for imaging of crystals as well as Raman analyses. The polished samples were cleaned with deionised water in an ultrasonic bath for 30 $minutes$ to remove any remaining particles adhering to the surface. Finally, samples were dried at 50 $°C$ for 24 $hours$ in a drying oven in order to eliminate water from samples surfaces that could alter analyses, especially Raman spectra acquisition.

Additionally, Simultaneous Thermal Analyses were performed using single sample powders subjected to a series of heating-cooling cycles to 1400 $°C$. One heating-cooling cycle was conducted to 900 $°C$ after slow cooling from 1400 $°C$. Initially, fast heating and cooling phases were conducted at 25 $°C\ min^{-1}$ (1400 $°C$) in order to obtain the glass transition temperature of the pure melt/glass phase mimicking the initial conditions of the controlled-cooling experiments. Secondly, after heating up to 1400 $°C$ a slow cooling rate of 0.5 $°C\ min^{-1}$ was applied down to far below the glass transition temperature, in order to produce nanolites, and then re-heated to 900 $°C$ and cooled at 25 $°C\ min^{-1}$ to obtain the glass transition temperature of the melt/glass fraction in the crystallised sample. Because of resolution limitations at slow heating and cooling rates ($< 1\ °C\ min^{-1}$), it was not possible to obtain a distinguishable exothermic peak associated to crystallisation.

5.2 Experimental results

5.2.1 Raman spectra

The Raman spectra of all post-experimental samples in this study, as well as an additional referential sample synthesised for 3 $hours$ at 800 $°C$ and 23 MPa are presented in Figure 5.1. All spectra show an asymmetric low wavenumber ($200 - 650\ cm^{-1}$) region with a prominent peak centred around $460 - 475\ cm^{-1}$, shifting to lower wavenumbers while cooling rate decreases. This peak decreases in intensity with decreasing cooling rate. Also in this region, all spectra show two shoulders at $\sim 300\ cm^{-1}$ and $\sim 375\ cm^{-1}$ and a third shoulder at $\sim 600\ cm^{-1}$. The two shoulders at lower wavenumbers increase with decreasing cooling rate, while the shoulder at higher wavenumber tends to become less clear at slower cooling rates,

especially when a peak between $670 - 690\ cm^{-1}$ starts appearing. The area of this low wavenumber region slightly decreases with slower cooling rates.

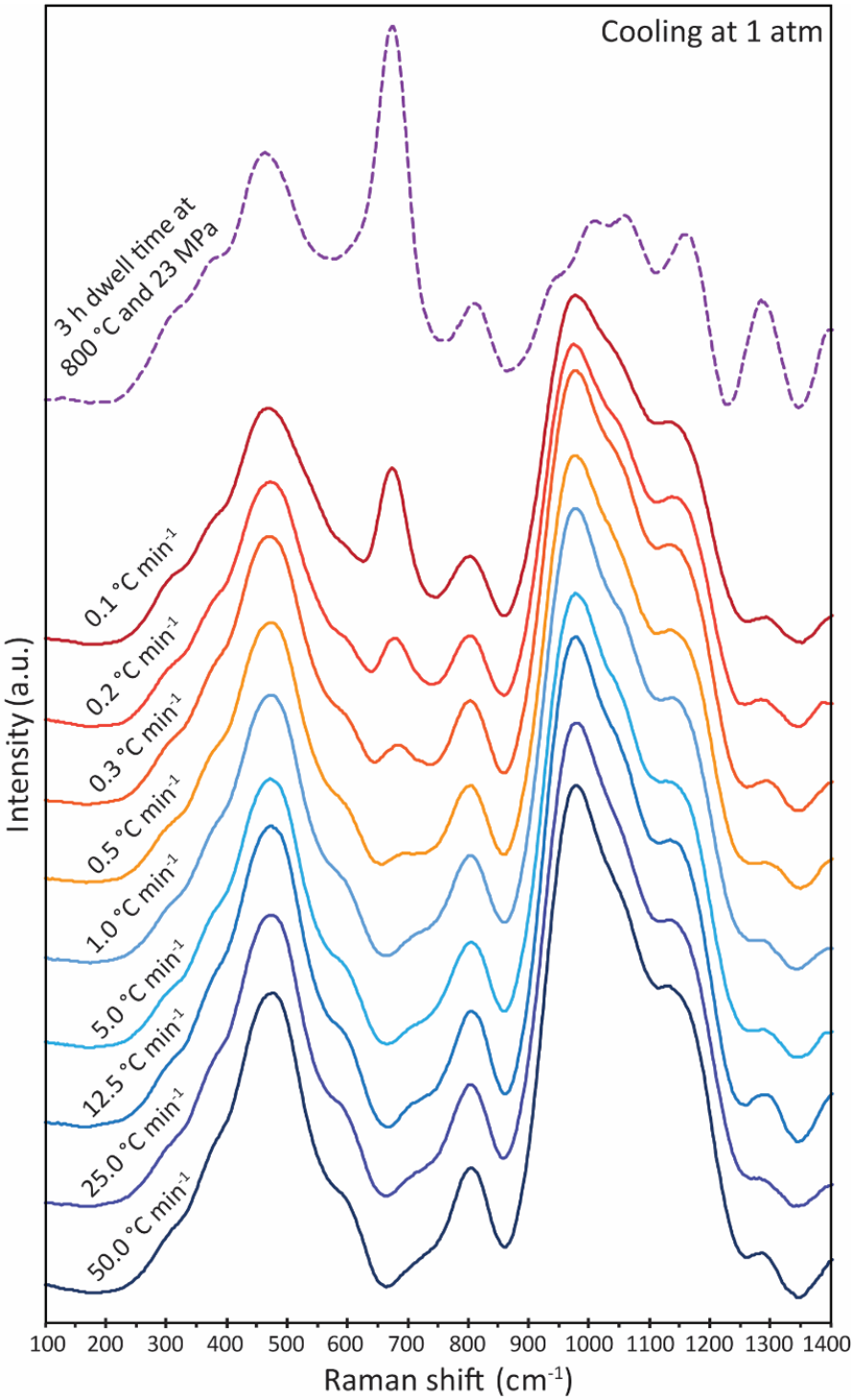

Figure 5.1. Raman spectra between $100 - 1400\ \mathrm{cm}^{-1}$ for experimental samples. Spectra are presented after intensity correction and baseline substraction (see Chapter 3 for details in spectra treatment). Colours represent the different cooling rates applied. Note the differences shapes of the low wavenumber (LW) and high wavenumber (HW) regions, and specially the peak at $670 - 690\ cm^{-1}$ in the middle wavenumber (MW) region.

Table 5.1. Run experiments and nanolites detection according to different methods.

Sample Name	Cooling rate (°C/min)	T_i (°C)	T_{Dwell} (°C)	T_f (°C)	Pressure (MPa)	Time $T_{liquidus}$-T_g (s)	Phases[a]
Kb-nano-03	50	1385	-	100	0.101	$2.2x10^2$	g
Kb-nano-04	5	1385	-	100	0.101	$2.2x10^3$	g
Kb-nano-05	25	1385	-	100	0.101	$4.3x10^2$	g
Kb-nano-06	1	1385	-	100	0.101	$1.1x10^4$	g
Kb-nano-07	12.5	1385	-	100	0.101	$8.6x10^2$	g
Kb-nano-08	0.5	1385	-	100	0.101	$2.2x10^4$	g+n[b]
Kb-nano-09	0.3	1385	-	100	0.101	$3.6x10^4$	g+n
Kb-nano-10	0.1	1385	-	100	0.101	$1.1x10^5$	g+n
Kb-nano-11	0.2	1385	-	100	0.101	$5.4x10^4$	g+n
Kb4-nano	-	-	800	-	23	$1.1x10^4$	g+n

a: magmatic phases (g=glass, n=Fe-Ti oxide nanolites).

b: nanolites identified by Raman peak only.

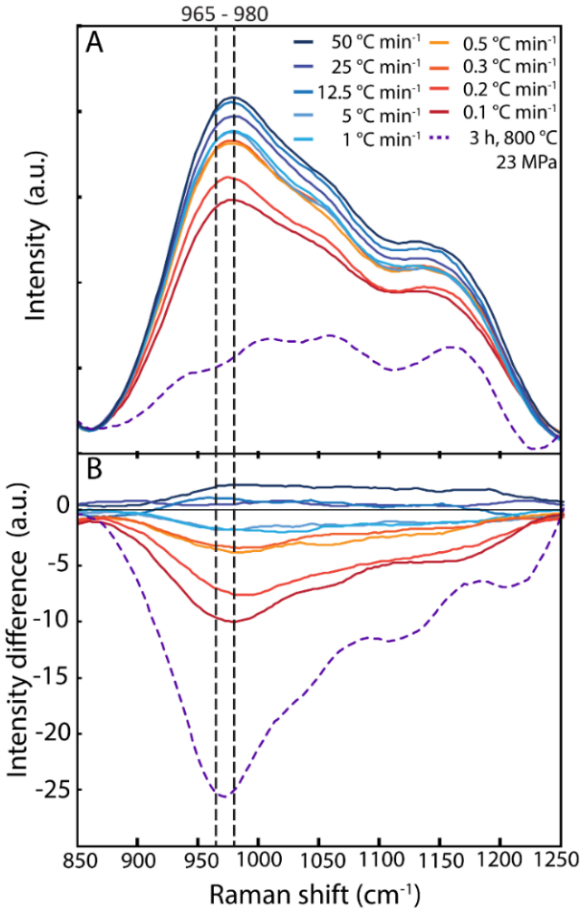

Figure 5.2. Raman spectra of the high wavenumber (HW) region between $850 - 1250\ cm^{-1}$. (**A**) Long-corrected Raman spectra. (**B**) Difference between each spectrum and the average between $1 - 50\ °C\ min^{-1}$ (black horizontal line). The band between $960 - 980\ cm^{-1}$ is marked with dotted lines. This band has been considered to be related to the abundance of Fe^{3+} (e.g. Cochain et al., 2012; Di Genova et al., 2017), hence variations in this band represent variations in ferric iron content of the glass. The peak appears to be closer to 980 cm and decreases in the intensity with decreasing cooling rate.

5.2.2 Scanning electron microscope imaging

BSE-SEM images show low nanolite content in samples subjected to cooling rates between $0.1 - 0.3\ °C\ min^{-1}$ and they were not visible in other samples subjected to different cooling rates (Fig. 5.3). Contrastingly, the sample synthesised at high pressure shows a high nanolite concentration with crystals between $\sim 10 - 50\ nm$ and relict magnetite microlites (Fig. 5.4). In this last sample, BSE- and EDS-SEM images taken at the neighbourhood of a relict magnetite microlite (Fig. 5.4) show a ring with an absence of nanolites and a relative depletion of Fe and a relative enrichment of K. Samples subjected to cooling rates between $1 - 50\ °C\ min^{-1}$ show a homogeneous nanolite-free glass with no remaining Fe-Ti oxide microlite content. The sample subjected to a cooling rate of $0.5\ °C\ min^{-1}$ has no visible mineral phase in BSE-SEM images.

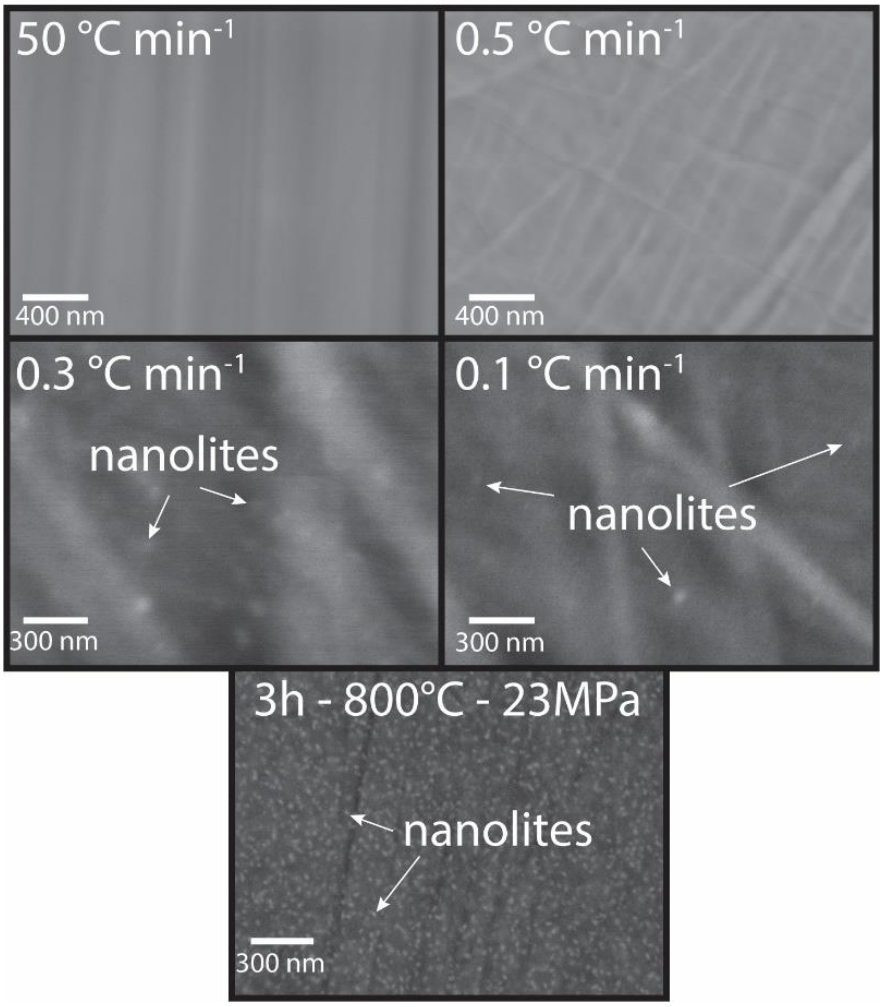

Figure 5.3. Backscattered electron image (BSE-SEM) of selected samples showing glass (darker grey phase) and Fe-Ti oxide nanolites (white and light grey phases). Straight lines represent preparation scratches. Cooling rates are presented in each case.

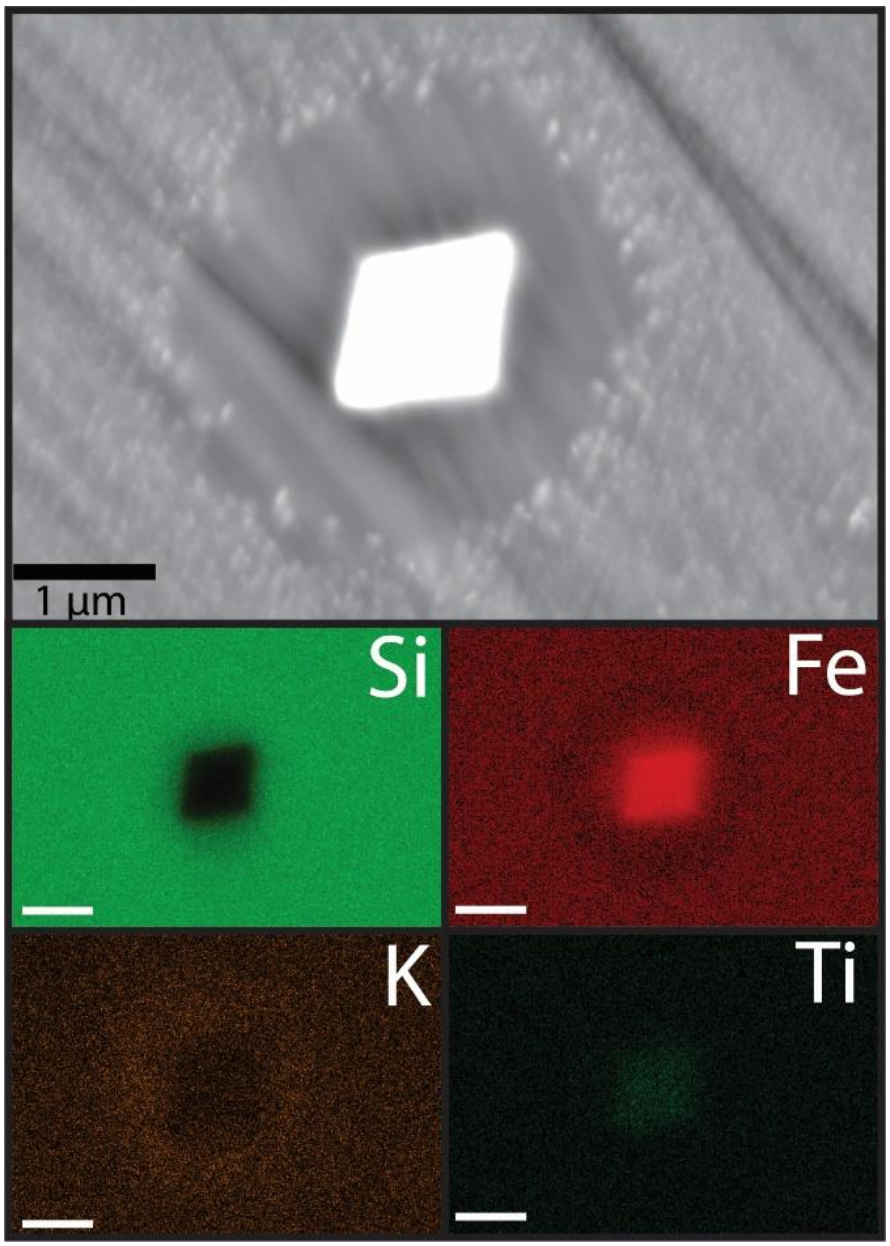

Figure 5.4. BSE- and chemical EDS-SEM images of the sample subjected at 800 $°C$ and 23 MPa. A magnetite microlite is shown together with the nanolite-bearing groundmass and a nanolite-free transition ring. It is possible to see an enrichment of K together with a depletion of Fe in the transitional ring zone.

5.2.3 Simultaneous thermal analyses

Two of the three simultaneous thermal analyses show a peak glass transition temperature at $\sim 772\ °C$, these are the analyses conducted in glass/melt phase only (i.e. without crystals). Instead, the two-phase sample (i.e. glass/melt + crystals) shows a $\sim 12\ °C$ shift towards higher temperatures, with a glass transition at $\sim 784\ °C$ (Fig. 5.5).

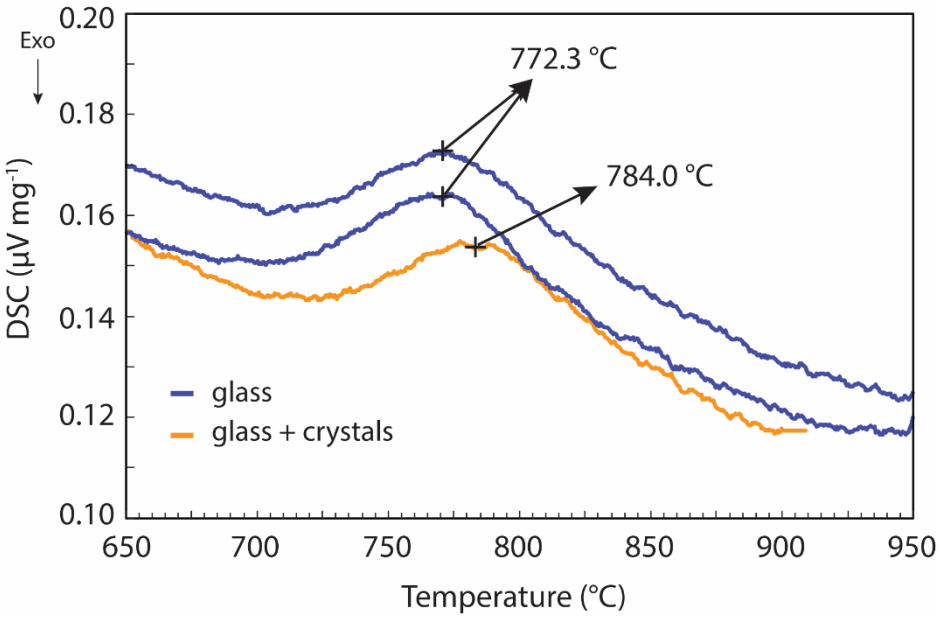

Figure 5.5. Simultaneous thermal analysis of the experimental material. Blue lines represent analyses performed with heating (up to 1400 °C) and cooling (below Tg) at rates of 25 °$C\ min^{-1}$. Yellow line represents an analysis performed in a sample previously heated up to 1400 °C and then cooled down to 0.5 °$C\ min^{-1}$ (i.e. contains nanolites, see discussion). This analysis was performed with heating (up to 910 °C) and cooling (below Tg) also at rates of 25 °$C\ min^{-1}$. Note the shift in peak temperature (Tg).

5.3 Discussion

The initial condition of 3 $hours$ dwell time at 1385 °C is sufficient to remove any memory effect in a rhyolitic melt such as specific sites for heterogeneous nucleation or any incomplete structural rearrangement within the melt (e.g. Vetere et al., 2013). The relaxation timescale of a silicate melt has been shown to be $\tau = \eta/G_\infty$, where η is the viscosity and G_∞ is the shear modulus with a mean value of $\sim 10\ GPa$ (Dingwell and Webb, 1989). The relaxation time can also be considered as the time for structural re-equilibration of the melt. For these experiments, at temperatures just above the liquidus, the viscosity is $\sim 10^9\ Pa\ s$ (calculated using Hess and Dingwell, 1996 and Liu et al., 2005 for water content; Fig. 5.6), which results in relaxation timescales in the order or $10^{-1}\ s$. Additionally, no relict mineral was observed with BSE-SEM images in any of the run products, meaning that the initial magmas are homogeneous and crystal nucleation started as homogeneous nucleation driven by cooling and not heterogeneously.

Furthermore, the absence of both a Raman peak between $670 - 690\ cm^{-1}$ and a brighter phase from BSE-SEM images in the range of $1 - 50$ °$C\ min^{-1}$ cooling rates, imply that in the

samples subjected to cooling rate between $0.1 - 0.5\ °C\ min^{-1}$, nanolites were formed as a result of magmatic cooling and they were not crystallised as a result of the heating produced by the laser during Raman analyses. It has been shown beforehand that analyses at these Raman conditions cannot crystallise Fe-Ti oxides over the timescales of the analyses (e.g. Di Genova et al., 2017c).

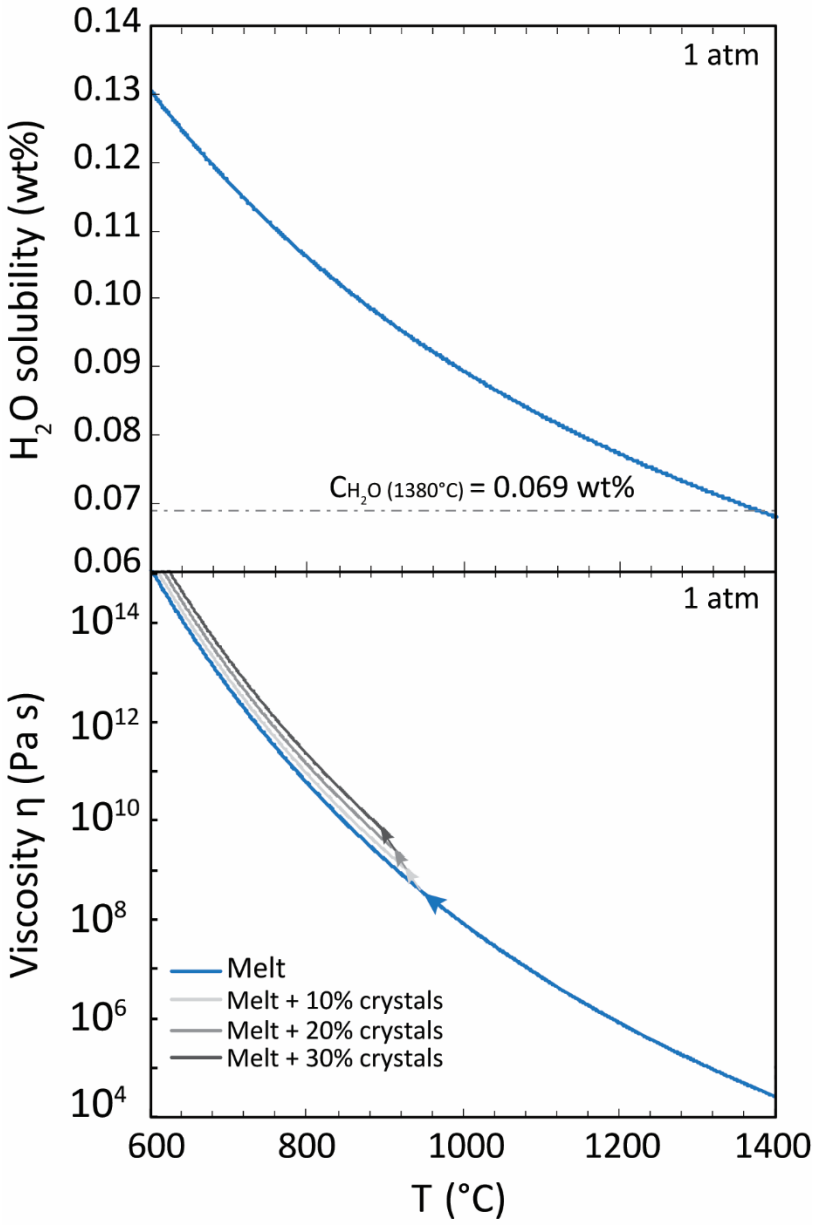

Figure 5.6. Water solubility (upper diagram) and magma viscosity (lower diagram) according to the starting cooling conditions. Water solubility was calculated using Liu et al., (2005) and the melt viscosity using Hess and Dingwell (1996). The viscosity of the melt in the experiments is shown in blue with a 0.069 wt.% H_2O according to the solubility calculation (upper diagram). The viscosity with crystal load is shown only as a reference in grey lines according to $\eta_{magma} = \eta_{melt}(C_{H_2O}, T) f(\varphi)$ (Costa 2005), considering a starting point of crystallisation in 952 °C. The transition from melt to melt+crystals are only schematic (grey arrows). Crystal bearing viscosity is computed for a crystal fraction φ of 0.1, 0.2 and 0.3. As reference, in the crystallinity given by nanolites was reported in Chapter 3 with a crystal fraction of nanolites φ_n of 0.02 in the synthesised sample.

The fact that this peak ($670 - 690\ cm^{-1}$) becomes higher in intensity at slower cooling rates and concomitantly the Fe^{3+} band decreases (Fig. 5.2) suggests that there is an increase in the nanolite content. Di Genova et al. (2018) associated this behaviour to a higher degree of nanolite crystallisation, but nevertheless this behaviour could be caused by higher nanolite nucleation or by higher growth of nanolites at lower number density, both processes potentially causing the same crystallinity. Considering the sample subjected to a dwell time ($3\ hours$) and higher pressure ($23\ MPa$) (Fig. 5.3), nanolites crystallised at a high relative number density compared to those subjected to controlled cooling. This sample also presents a much higher intensity at the $670 - 690\ cm^{-1}$ peak and closer to $670\ cm^{-1}$ compared to the cooling-controlled samples. In parallel, no clear BSD-SEM images distinguishing the abundance of nanolites between $0.1 - 0.3\ °C\ min^{-1}$ cooling rates could be taken, driven by the low backscattered signal given by the nanolites. Figure 5.3 shows an apparent higher number density of nanolites in the sample subjected to $0.3\ °C\ min^{-1}$ than the one cooled down at $0.1\ °C\ min^{-1}$, samples that show lower and higher intensity in the $670 - 690\ cm^{-1}$ peak respectively. This confirms the dichotomy of the $670 - 690\ cm^{-1}$ peak intensity regarding the identification of the crystal number density or bigger crystals and it can only be applied to identify the overall crystallinity in the samples

However, and based on the Raman peak intensities at the $670 - 690\ cm^{-1}$ band, higher crystal content can be inferred from a higher peak intensity. The results are consistent with similar cooling experiments conducted in a rhyolitic magma (Vetere et al., 2013) and more primitive magmas (Iezzi et al., 2008; Mollo et al., 2009; Vetere et al., 2013) that also correlate a higher crystal content with decreasing cooling rate.

5.3.1 Conditions and timescales for nanolites crystallisation

There are minimum chemical conditions regarding element concentrations in order to form nanolites. Figure 5.4 shows that nanolites did not form around pre-existing Fe-Ti oxide crystals that were surrounded by melt depleted in iron. Even though the small scale of these crystals and their depleted "haloes" exclude measure of the absolute chemistry of such regions, shown in Figure 5.4, it is clear from the EDS-SEM images that Fe-Ti oxide nanolites do not form in iron-poor and more differentiated rhyolitic melts. This is shown by the relative decrease of Fe and an important increase in K concentration in the nanolite-free region around a microlite. Furthermore, the absolute decrease in the Fe^{3+} band ($965 - 980\ cm^{-1}$) of the high

wavenumber region of the Raman spectra (Fig. 5.2) is most likely driven by the uptake of Fe by the forming crystals, where it becomes more evident for samples with higher nanolite content subjected to slower cooling rates. Mollo et al. (2009) showed how in a range of conditions where titanomagnetite (solid solution between ulvospinel and magnetite) crystallises, the relative total iron content in the mineral is higher at faster cooling rates, and other cations (e.g. Ti) become more concentrated in the minerals at slower cooling rates. This confirms that the first chemical uptake of Fe-Ti oxide nanolites requires a relatively high iron concentration and they are less probable to form in iron-poor differentiated magmas such as calc-alkaline rhyolites.

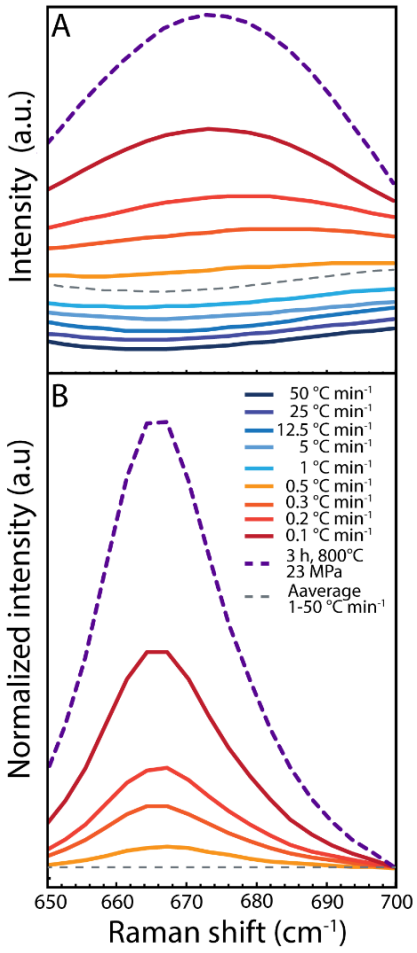

Figure 5.7. Raman spectra in the region between 650−700 cm^{-1}. (**A**) Shows the spectra at different cooling rate and the spectra of the sample prepared at 800 $°C$ and 23 MPa for comparison. It can be noticed two main shapes of the spectra in this region: the first one synoidal between $1 - 50\ °C\ min^{-1}$ and the second one concave between $0.1 - 0.5\ °C\ min^{-1}$. The average of the synoidal spectra between $1 - 50\ °C\ min^{-1}$ is shown in grey dotted line. (**B**) Shows the spectra normalised to the average line in **A**.

Despite the observation that there is a clear correlation between cooling rate of the experimental magmas and nanolite content (Fig. 5.7), the temperature at which the nanolites start to crystallise remains unknown. Therefore, in order to better constrain the starting crystallisation conditions for nanolites, I performed a thermodynamical crystallisation modelling approach by using rhyolite-MELTS (Gualda et al., 2012; Ghiorso and Gualda, 2015). For this I used the chemical composition of the starting material given in Table 3.1 (Chapter 3).

The modelling was considered isobarically at $1\,bar$ and cooling starting from $1385\,°C$, reproducing the experimental conditions. An oxygen fugacity at the NNO and NNO+1 (in log units) buffers were used with steps of $5\,°C$ for cooling down to $600\,°C$, i.e. $\sim 180\,°C$ lower than the glass transition temperature (Fig. 5.8). As identified in SEM and Raman analyses, only Fe-Ti oxides were able to crystallise. The modelling shows that within the temperature range over the glass transition temperature, spinel species (mostly ulvospinel-magnetite solid solution) could crystallise at a liquidus temperature of $952\,°C$ without difference for both buffers, so any Fe-Ti oxide is not expected to crystallise over this temperature in the system and this temperature is then considered to represent the starting point for crystallisation of Fe-Ti oxide nanolites during cooling.

On the other hand, the low intensity peak for the sample cooled at $0.5\,°C\,min^{-1}$ and the absence at any BSD-SEM image, suggest that this cooling rate represents the minimum rate at which nanolites are able to nucleate. It is possible to compare the time at which every magma was subjected to temperatures between the liquidus and the glass transition (Fig. 5.8; Table 5.1). This time varies between $10^2 - 10^5\,s$ from the fastest to the slowest cooling rate applied and the transition from nanolite-free to nanolite-bearing occurs between 1 and $0.5\,°C\,min^{-1}$ in a timescale of $10^4\,s$. This is also consistent with the dwell time of 3 $hours$ ($\sim 10^4\,s$) at which the sample subjected to high pressure formed nanolites. It is possible then to constrain the minimum timescale for nanolites to form in the experiments in the order of $10^4\,s$ for dynamic crystallisation (cooling), while the same timescale is sufficient for equilibrium crystallisation.

Nucleation theory indicates that the nucleation rate is related to the polymerisation degree of the melt, whereby it should be higher in a less polymerised melt (Kirkpatrick 1983). Thus it is anticipated that the changes in the melt structure during cooling will likely affect any potential nucleation. In the following section I analyse the changes in the melt structure during cooling and its relation to nanolite formation.

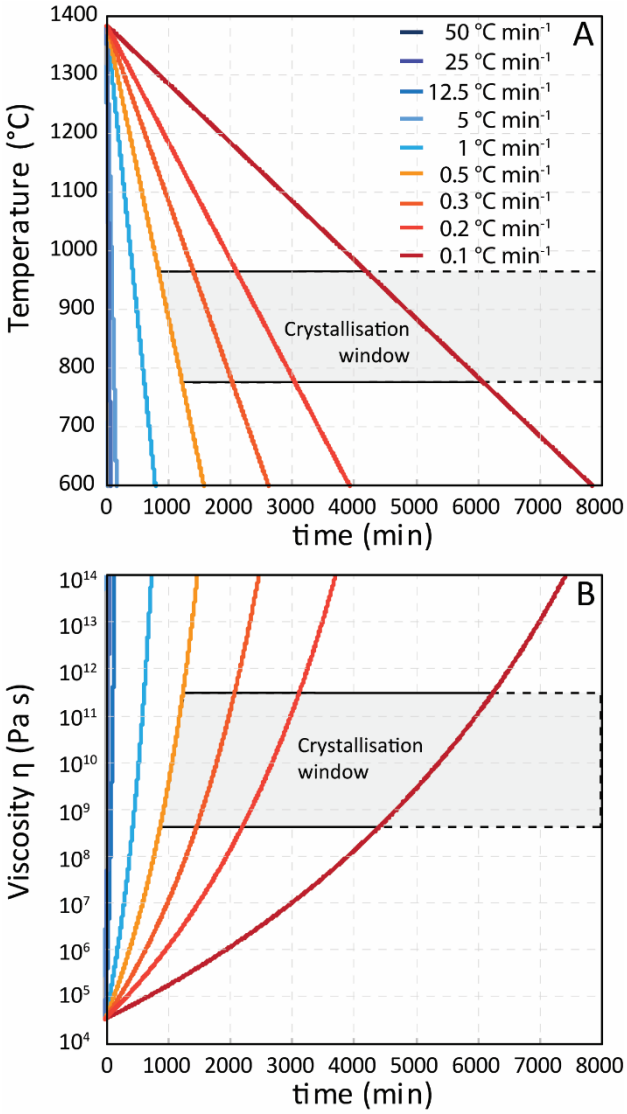

Figure 5.8. Temperature and viscosity paths during cooling. (**A**) Cooling paths from starting dwell temperature of 1385 °C until below the glass transition temperature. (**B**) Viscosity paths for every cooling experiment calculated using Hess and Dingwell (1996) with the calculated initial water content (0.069 *wt*. %) using the solubility model of Liu et al. (2005). Both plots show the crystallisation window between the liquidus (952 °C) and glass transition (772 °C) temperatures.

5.3.2 The effect of cooling rate on melt structure and viscosity

Since the low- and high wavenumber areas of the Raman spectra represent vibrations of tetrahedra rings and tetrahedra units with certain amount of non-bridging oxygens, they also can be interpreted as polymerised and less polymerised glasses respectively. The ratio between the areas of the low and high wavenumber regions, or the intensities of the peaks at these zones can be used to check a relative degree of polymerisation and it has been correlated to chemical-based melt structural parameters commonly used (e.g. Di Muro et al., 2006b; Giordano et al.,

2019) such as the number of non-bridging oxygens per tetrahedron (NBO/T; Mysen, 1988) and the structural modifier content (SM; Giordano and Dingwell, 2003), both parametrisations of the stoichiometric degree of polymerisation of a melt. It has been observed that the ratio between the peak intensity in these two regions decreases when glass becomes more depolymerised and *vice versa* (e.g. Beherens et al., 2006; Di Muro et al., 2006b; Mercier et al., 2009; Giordano and Russell, 2018; Giordano et al., 2019). Figure 5.9 shows that both the peak intensity and area ratios between the low and high wavenumber bands and regions increase when cooling rate decreases. They tend to remain at similar low values for cooling rates in the order of $10^0 - 10^1\ °C\ min^{-1}$ or higher and they start detaching towards higher ratio values at cooling rates of $10^{-1}\ °C\ min^{-1}$ and slower. This means that the polymerisation of the melt does not vary greatly at high quench rates, while at slower quench rate the melt becomes considerably more polymerised.

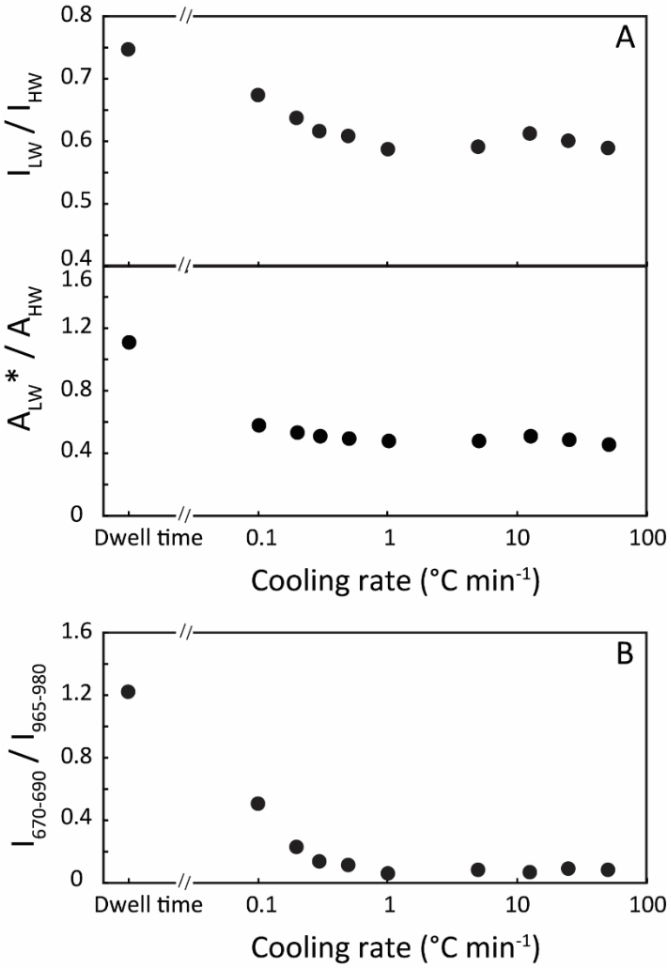

Figure 5.9. Intensity and area ratios between peak band and region at each cooling rate. (A) Peak intensity ration between $460 - 475\ cm^{-1}$ band and $965 - 980\ cm^{-1}$ band (upper diagram) and area ratio between $200 - 600\ cm^{-1}$ of the low wavenumber region and $850 - 1250\ cm^{-1}$ of the high wavenumber region (middle diagram). * Area of LW region was considered only until $600\ cm^{-1}$ to avoid the effect of the growing $670 - 690\ cm^{-1}$ band (Fig. 5.1). (B) Peak intensity ratio between $670 - 690\ cm^{-1}$ band and $965 - 980\ cm^{-1}$ band.

In order to understand these changes in the polymerisation of the melt, the structural changes need to be correlated to crystallisation of nanolites. Figure 5.10 shows deconvolution analyses conducted in the high wavenumber region of the Raman spectra of all the samples subjected to cooling and Figure 5.11 shows the same for the nanolite-rich sample subjected to dwelling at high pressure. No significant change in the different bands associated to the Q^n species related to cooling could be observed (Fig. 5.10), and minor changes in the resolution window of the deconvolution analysis are conceivable. Within the resolution of the deconvolution analysis the contribution of the Fe^{3+} band remains proportionally stable, same holds for the contribution of the T_{2s} band associated to Fe^{2+}, and significant changes occur when compared the overall areas between the low and high wavenumber regions. This indicates that the iron oxidation state of the glass does not vary considerably while decreasing the cooling rate and the main changes occur in the total iron content of the melt.

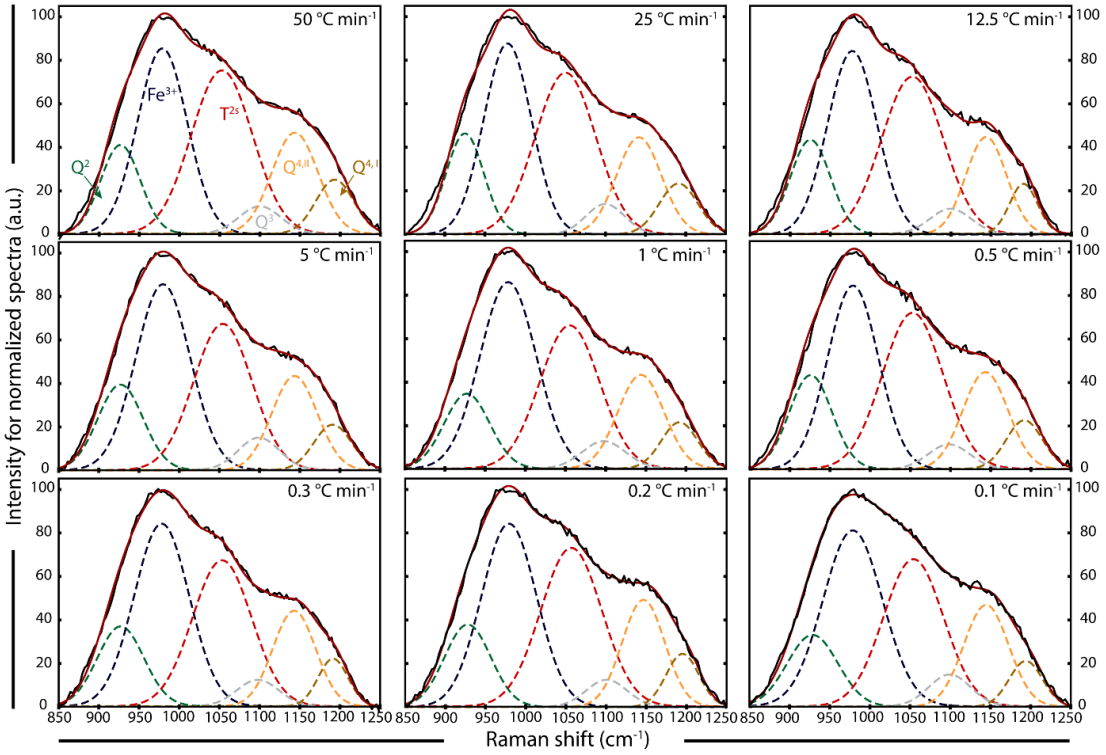

Figure 5.10. Deconvolution of the Long-corrected Raman spectra in the high wavenumber region ($850 - 1250\ cm^{-1}$) at different cooling rates. There is no significant change in the contributions of the different bands except a slight decrease in the Fe^{3+} peak at the slowest cooling rate.

When analysed the correlation between the polymerisation degree and nanolite crystallisation (Fig. 5.12), given by the ratios between the LW and HW areas and the intensities of the nanolite and ferric iron bands (Table 5.2), these two ratios remain at similar values for fast cooling rates and they start increasing at a cooling rate of $0.5\ °C\ min^{-1}$ and slower. This behaviour indicates

that the main polymerisation increase seen for slow cooling rates ($0.1 - 0.5\ °C\ min^{-1}$) is mainly driven by the crystallisation of nanolites, rather than a direct cooling effect in the melt structure. This effect is most likely a result of the re-structuring melt as a response to the chemical changes occurring cause by the uptake of elements, mainly Fe, by the Fe-Ti oxide nanolites nucleation and later growth.

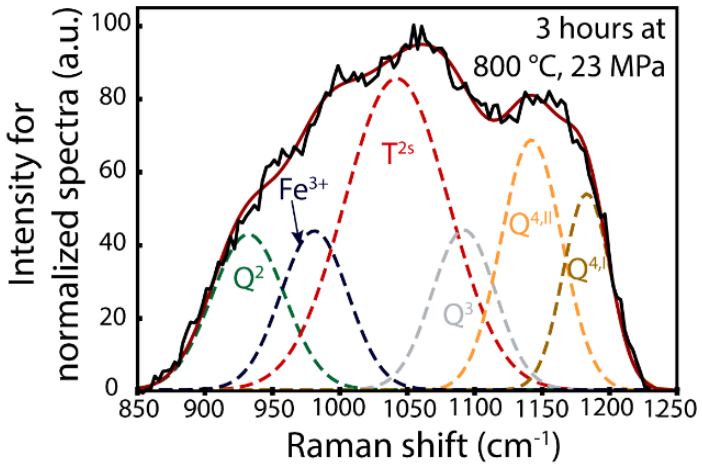

Figure 5.11. Deconvolution of the Long-corrected Raman spectra in the high wavenumber region ($850 - 1250\ cm^{-1}$) for the sample subjected at $800\ °C$, $23\ MPa$ for a dwell time of 3 $hours$ and fast quenched. There is a significant change in the contributions of the different bands respect to the cooling-controlled samples (Fig. 5.10) with a decrease in the Fe^{3+} peak and higher contributions of the other bands.

It has been proposed that the viscosity of a melt is directly related to its degree of polymerisation (e.g. Giordano and Russell, 2018; Giordano et al., 2019). This leads to an increase in the bulk viscosity of a magma when the polymerisation of its silicate melt phase increases, which is compounded in combination with the increase in the crystal load (Fig. 5.6).

Di Genova et al. (2017a) showed that an increase in K_2O content can be directly related to an increase in the melt viscosity. It can be seen that there is relative increase in K_2O at the ring around a Fe-Ti oxide (Fig. 5.4) caused by the uptake of elements from the melt. This allows to infer that the formation of Fe-Ti oxides possibly increases the relative K content and consequently the viscosity of the melt. However, by analysing the resultant melt composition from the thermodynamic modelling, there are changes of up to $\sim 2\ wt.\%$ in SiO_2 (from 75.34 to 77.44 $wt.\%$) between the initial composition and the one at the glass transition temperature. This is accompanied by a reduction of $\sim 2.5\ wt.\%$ in total iron content (from 3.34 to 0.83 $wt.\%$ FeO_T). These two melt chemical variations produce an increase in the melt viscosity.

Table 5.2. Raman spectra parameters. Measured from Long-corrected and baseline subtracted spectra (see Chapter 3 for details).

Sample Name	Cooling rate (°C min^{-1})	$I_{460-475}/I_{965-980}$	$I_{670-690}/I_{965-980}$	A_{LW}/A_{HW}
Kb-nano-03	50	0.59	0.08	0,45
Kb-nano-04	5	0.59	0.08	0.48
Kb-nano-05	25	0.60	0.09	0.49
Kb-nano-06	1	0.59	0.05	0.48
Kb-nano-07	12.5	0.61	0.06	0.51
Kb-nano-08	0.5	0.61	0.11	0.50
Kb-nano-09	0.3	0.62	0.13	0.51
Kb-nano-10	0.1	0.67	0.50	0.58
Kb-nano-11	0.2	0.64	0.22	0.53
Kb4-nano	dwell	0.75	1.22	1.11

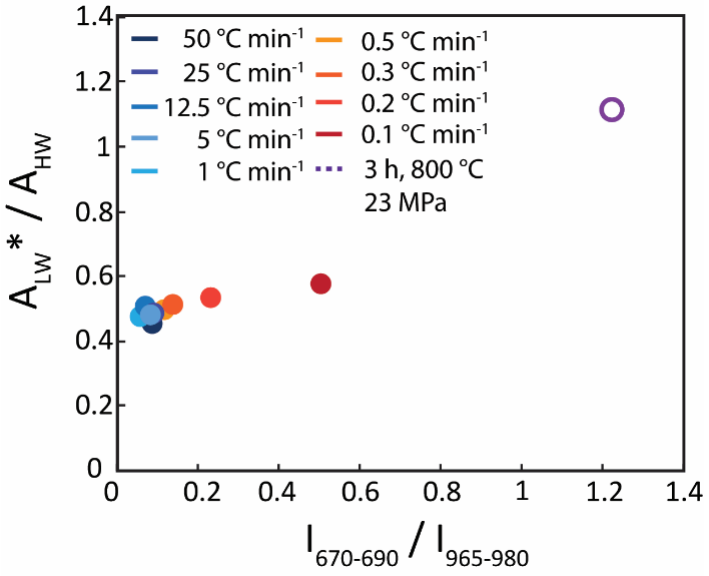

Figure 5.12. Area ratio between $200-600\ cm^{-1}$ of the low wavenumber region and $850-1250\ cm^{-1}$ of the high wavenumber region versus peak intensity ratio between $670-690\ cm^{-1}$ band and $965-980\ cm^{-1}$ band. Area ratio is chosen over intensity ratio in the low wavenumber region for being a better representative of the polymerisation of the melt since it considers a wider range of the spectra.

Additionally, the simultaneous thermal analyses (Fig. 5.5) show that there is a shift of $\sim\Delta 12\ °C$ towards a higher temperature in the glass transition from $772\ °C$ to $784\ °C$ in the sample containing glass and crystals. This peak temperature shift implies changes in the glass and hence melt structure of the sample that can represent a change in the chemical composition of the melt, driven by the chemical uptake from the crystals. A shift towards higher temperature in analyses conducted at the same heating-cooling sequence speaks for an increase in melt

viscosity after crystallisation. This increase in viscosity coincides with the onset of crystallisation inferred from the experiment conducted at the same cooling rate than the STA analysis ($0.5\ °C\ min^{-1}$) shown by the Raman spectra, confirming the correlation between crystallisation of Fe-Ti oxide nanolites and the increase of melt viscosity. This has important consequences for volcanic systems as I discuss in the following section.

5.3.3 Implications for natural volcanic systems

Eruptive products are the results of a great variety of volcanic eruption styles, ranging from mildly effusive to violently explosive, with different hazards related (e.g. Cashman and Scheu, 2015; Gonnermann 2015; Cassidy et al., 2018). While a magma erupted explosively tend to be fragmented and hence fast quenched in air (e.g. $\sim 10^3\ °C\ min^{-1}$ Xu and Zhang 2002; D'Oriano et al., 2014), those that are erupted effusively or are still in the conduit as magma plugs tend to have slower cooling rates, typically in the order of $10^{-3} - 10^1\ °C\ min^{-1}$, where the higher values are for fast cooled lava flows (e.g. Harris et al., 2002; Cashman et al., 2013; Kolzenburg et al., 2017; Thivet et al., 2020). During magma migration towards the surface, magmas pass from reduced to oxidising conditions in air once the (near) surface is reached (e.g. Kolzenburg et al., 2018). The cooling rates ($10^{-1} - 10^1\ °C\ min^{-1}$) and oxidising conditions, as well as the temperature range between the liquidus temperature and the glass transition temperature of the experiments cover a range of conditions relevant for magmas that are erupted and/or emplaced under slow quench rates and oxidising conditions such as lava flows, lava domes and shallow magma plugs. Particularly lava domes and shallow magma plugs represent magmas that can be partially degassed, but that can still contain enough volatiles to build up overpressure and potentially contribute to an explosive eruption (e.g. Diller et al., 2006; Cassidy et al., 2018). The effect of nanolite crystallisation can then be taken into account in terms of the viscosity increase and the effect on magma degassing dynamics.

As magma viscosity clearly plays a central role in controlling the explosivity of a volcanic eruption. The increases of the bulk magma viscosity driven by both the increase of the melt viscosity and by the crystal load during the nanolite growth to be expected during eruption may be relevant in this regard. The increase of bulk magma viscosity has been estimated previously (Di Genova et al., 2017a) to be up to four orders of magnitude (four log units in Pa s) with respect to nanolite-free magma. It has also been suggested (Di Genova et al., 2017a,c) that this viscosity increase driven by nanolite crystallisation could lead to explosive volcanic eruptions. The results of these experiments support this hypothesis, at least for cases of shallow magma

plugs and lava domes that are met by similar slow cooling and high oxidising conditions as explored in this study.

Further, it has recently been shown in Chapter 4 that nanolites have the potential to enhance the transition from an effusive eruption to an explosive behaviour by increasing the bubble number density and accelerating the bubble growth rate in the magma. When a lava dome or a shallow portion of magma in the conduit is in a range of conditions suitable for nanolite crystallisation such as those shown in this study, a perturbation such as heating from an input of magma or decompression triggered by the partial collapse of the lava dome might be able to cause nucleation and grow of pressurised gas bubbles which in combination of a high viscosity might unleash the potential for an explosive eruption.

5.4 Concluding remarks

This chapter has shown that slow magma cooling at low pressures and oxidising conditions can be a determinant factor in order to promote crystal nucleation and growth in highly viscous magmas.

Nanolites start forming at cooling conditions relevant for shallow natural magmas, producing a concomitant increase in melt polymerisation and hence in viscosity. These nanolites are formed in timescales sufficient to produce crystals at high number density in timescales relevant for these shallow magmas such as magma plugs or even during effusive eruptions ($\sim hours$).

Both, the higher degree of melt polymerisation and a higher load of crystals in nanolite-bearing magmas may cause an increase in the magma viscosity and an increase in sites for heterogeneous bubble nucleation in degassing magmas. These effects have the potential to shift a shallow magma into conditions favourable for explosive eruptions pending a triggering mechanism.

6

The coupled effect of microlites and phenocrysts on bubble nucleation, coalescence and outgassing: Insights from degassing of low-water rhyolitic magma

Chapter Summary

Degassing of rhyolitic magma mostly involves water exsolution and can be driven by magma decompression, chemical changes in the silicate melt phase and heating. Exsolved water form gas phase bubbles that are coupled to the magma because of the high viscosity of rhyolitic melt. This process fosters magma ascent and might end up producing a volcanic eruption. Whether the eruption will develop as effusive or explosive depends mainly on the speed of bubble formation and growth, and on whether the exsolved gas phase remains trapped in the magma as isolated bubbles or escapes via outgassing towards the atmosphere or the conduit walls. Both degassing and outgassing are enhanced in the presence of crystalline phases

in the magma. Crystals not only promote bubble formation by heterogeneous nucleation, but also collaborate in the bubble coalescence process, helping bubbles to connect and form a permeable network that allows gas to escape reducing bubble overpressure. Many studies have been carried out trying to understand the individual effect of different crystalline phases at different sizes on heterogeneous nucleation and gas escape. However, no experimental study has been performed so far showing the coupled effect of microlites and phenocrysts of multiple mineral phases in a natural rhyolitic magma. In this chapter, I perform heating induced vesiculation experiments in a multiphase, low-water content and bubble-free natural rhyolite in order to shed light on the role of the nature and size of crystals on degassing of shallow rhyolitic magma. The experiments were conducted at high temperature and isobarically at atmospheric pressure in an optical dilatometer. The results show that mainly microlites have a large influence on bubble nucleation over phenocrysts, whereas phenocrysts enhance bubble coalescence and connectivity more than microlites in this particular case. Among microlites, bubbles seem to nucleate more easily on Fe-Ti oxides than feldspars. The textures are then compared with those produced in a rhyolitic magma with slightly lower viscosities and with lower microlite content, that was subjected to similar conditions and produced less bubble coalescence and connectivity. These findings help to better understand the roles that pre- and syn-eruptive crystalline phases play in the degassing process during magma ascent.

6.1 Samples used and experimental conditions

For these bubble growth experiments, I used samples from the natural vitrophyric rhyolite from Laguna del Maule (LdM) Volcanic Field and I compared the results with those obtained for similar experiments with the natural obsidian from Krafla volcano in Chapter 4. Important differences between these two types of materials should be considered in order to compare the main post-experimental results. The vitrophyric rhyolite from LdM contains $\sim 4.5\ vol.\%$ crystals consisting of syn-eruptive microlites ($\leq 50\ \mu m$) and pre-eruptive phenocrysts ($> 50\ \mu m$; include micro-phenocrysts and phenocrysts) of plagioclase, biotite and Fe-Ti oxides (Fig. 3.1B). This rhyolitic material is iron-poor ($0.83\ wt.\%\ FeO_T$; Table 3.1) with a calculated water content of $\sim 0.10\ wt.\%$ (see Chapter 3 for details). Krafla obsidian is an aphyric ($<< 1\ vol.\%$ Fe-Ti oxide micolites) iron-rich ($3.34\ wt.\%\ FeO_T$; Table 3.1) rhyolite (Fig. 3.1A) from Hrafntinnuhryggur eruption, Krafla volcano in Iceland, with $0.11 - 0.15\ wt.\%$ H_2O (Tuffen and Castro 2009), i.e. with slightly higher water concentration than the LdM vitrophyric rhyolite.

The samples used correspond to cylinders of $\sim 5\ mm$ diameter and $\sim 3\ mm$ length that were placed into the optical dilatometer and then heated at controlled heating rates and kept at final targeted temperatures for dwell times of $8 - 14\ hours$. The heating rates applied were $1 - 50\ °C\ min^{-1}$ to isothermal dwells at $930 - 1100\ °C$. As in chapter 4, the real-time sample area and shape were recorded as they crossed the glass transition. Increases in the recorded sample area were transformed to porosity values according to equations 1 and 2. The experimental products for the two sample types were then analysed (see Chapter 3) and compared.

6.2 Results

During the experiments, the samples expanded during heating with a difference in the onset of expansion. For comparison, the Krafla obsidian started expanding earlier than the LdM vitrophyric rhyolite (Figure 6.1). Both computed tomography and scanning electron microscope imaging reveal that expansion is driven by bubble growth (Fig. 6.2). For the LdM vitrophyric rhyolite samples, those subjected to temperatures higher than $1000\ °C$ porosity increased until a maximum value and then decreased until a final porosity value (Figures 6.3A and 6.4). This behaviour is not dependent of heating rate (Fig. 6.3B), where all samples show stable final porosity within the error associated (±0.02). Since the focus of this chapter is the LdM vitrophyric rhyolite behaviour, for details in the behaviour of the porosity in time for the Krafla obsidian I refer the reader to the Chapter 4, particularly Figure 4.1.

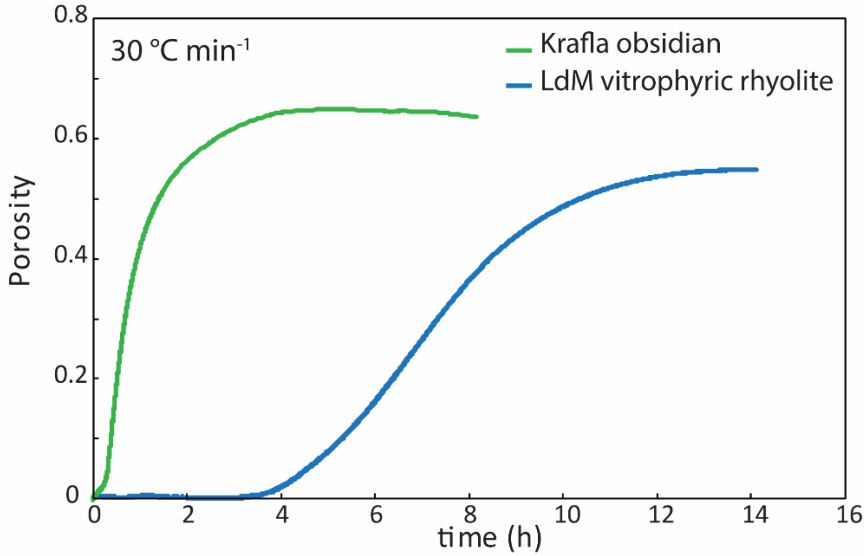

Figure 6.1. Comparison between Krafla obsidian and LdM vitrophyric rhyolite. Both samples were heated at a rate of $30\ °C\ min^{-1}$ until final dwell temperature. The Krafla obsidian was heated up to 1000 °C and the LdM vitrophyric rhyolite up to 993 °C, but both samples are considered as equivalent conditions for comparison only.

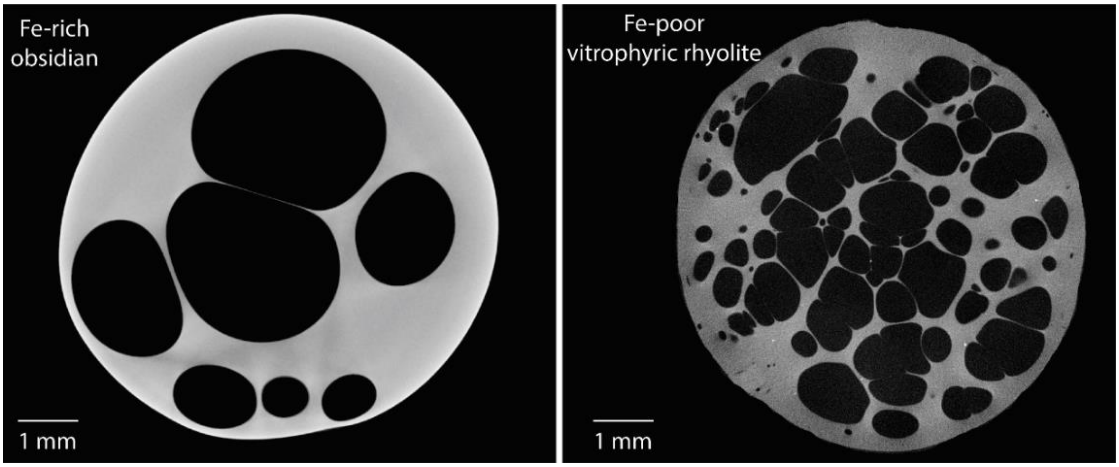

Figure 6.2. X-ray computed tomography image of both types of materials. The vitrophyric rhyolite reached higher bubble number densities and more bubble coalescence.

Table 6.1. Final and maximum porosities for the LdM vitrophyric rhyolite experiments. Error in porosity is values ± 0.02 and in temperature is ± 2 °C.

Final Temperature (°C)	Sample name	Heating Rate (°C min^{-1})	Final Porosity	Max. Porosity
Variable final temperature				
930	LdM-OD-18	30	0.04	0.04
946	LdM-OD-09	30	0.09	0.09
957	LdM-OD-11	30	0.28	0.28
973	LdM-OD-04	30	0.42	0.42
993	LdM-OD-03	30	0.55	0.55
1011	LdM-OD-12	30	0.53	0.59
1022	LdM-OD-05	30	0.53	0.61
1050	LdM-OD-06	30	0.53	0.67
1070	LdM-OD-07	30	0.49	0.68
1102	LdM-OD-17	30	0.39	0.74
Variable heating rate				
989	LdM-OD-14	1	0.54	0.54
986	LdM-OD-16	5	0.56	0.56
985	LdM-OD-15	10	0.58	0.59
993	LdM-OD-03	30	0.55	0.55
991	LdM-OD-13	50	0.57	0.58

The measured crystal number density of microlites for the LdM vitrophyric rhyolite is $5.1\ x\ 10^1\ mm^{-3}$. Phenocrysts number density was estimated between $\sim 10^{-1} - 10^0\ mm^{-3}$. Final porosities vary between $0.04 - 0.55$ for samples without shrinkage and between $0.39 - 0.53$ for samples that experienced shrinkage (Fig. 6.3 and Table 6.1). The later reached maximum porosities between $0.59 - 0.74$ before volume started to decrease. All bubble number densities measured for these samples range between $2.1 - 7.4\ x\ 10^1\ mm^{-3}$. Figure 6.4 shows the link between the maximum porosity and amount of shrinkage with temperature.

Both increase with temperature, which is inversely correlated to the magma viscosity. Additionally, all samples formed a thin dense outer layer with very low bubble content (Fig. 6.2).

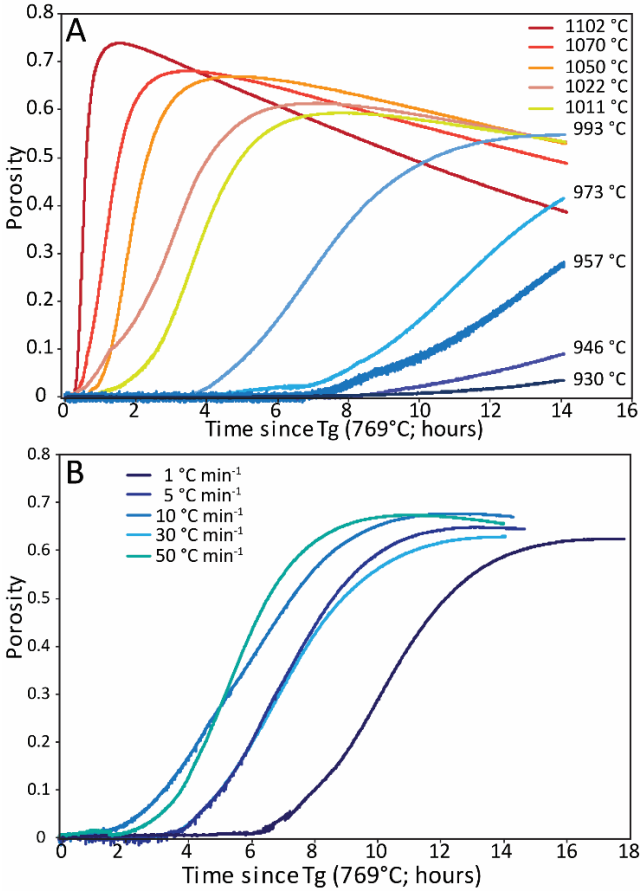

Figure 6.3. Porosity versus time for the LdM vitrophyric rhyolite. (**A**) Experiments conducted at the same heating rate of $30\ °C\ min^{-1}$ and then a dwell time of $14\ hours$ at final different temperatures. (**B**) Experiments conducted at comparable final temperatures between $985 - 993\ °C$ and at different heating rates.

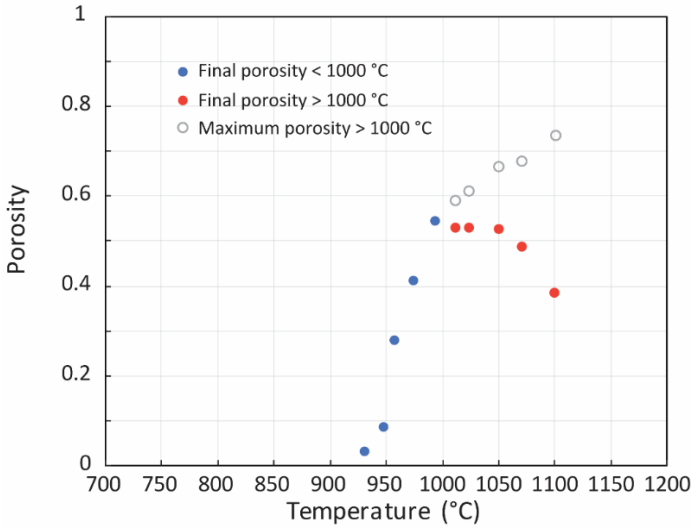

Figure 6.4. Maximum and final porosities for the vitrophiric rhyolite. The difference between maximum and final porosity starts at a porosity value of ~ 0.55 and between lower and higher than 1000 °C. Errors in porosity and temperature and in the symbol diameter.

6.3 Discussion

The low-water concentration induces a high magma viscosity ($10^6 - 10^8\ Pa\ s$) and low water exsolution, allowing to track the role of the different crystalline phases in a scenario where the main textural features are preserved right after happening. This reduces the propensity for bubble shape modifications driven by volume re-equilibration of coalesced bubbles. This reduces the chances to mistake two coalesced bubbles for one individually nucleated with larger growth.

The time lag difference in the onset of bubble growth after crossing the glass transition temperature between the Krafla obsidian and the LdM vitrophyric rhyolite (Fig. 6.1) may be related to the difference in water content and subsequently supersaturation degree and amount of exsolved water, with a contribution of the lower viscosity of the Fe-rich samples (see viscosity discussion below). Although crystals generally promote earlier bubble nucleation and hence bubble growth by shortening the distances between bubbles for water to diffuse (e.g. Gonnermann and Manga 2007), the amount of water exsolved right after crossing the glass transition temperature in the case of LdM is zero up to 900 °C, since it is still in undersaturated conditions ($0.10\ wt.\%$ water concentration against $0.11\ wt.\%$ solubility; Liu et al., 2005). Additionally, its viscosity is higher, causing more resistance to bubble growth. These two effects combined result in delayed bubble growth for LdM compared to the Krafla obsidian which has a higher water content and lower viscosity.

6.3.1 Bubble nucleation on Fe-Ti oxide microlites

As shown by computed tomography analyses in Figure 6.5 for the LdM vitrophyric samples, bubbles are almost systematically associated to Fe-Ti oxides and occasionally to other mineral phases. This is a result of heterogeneous bubble nucleation on the surface of these crystals. Crystals in a magma can reduce the energy barrier for bubble nucleation compared to homogenous nucleation (e.g. Hurwitz and Navon, 1994; Gardner et al., 1999; Gardner and Denis 2004). Studies have shown that heterogeneous bubble nucleation can be enhanced more by Fe-Ti oxides, such as magnetite and hematite, than plagioclase phases (Hurwitz and Navon, 1994; Cluzel et al., 2008). This preferential nucleation on oxides occurs because of an increase in the contact angle between bubbles and the crystals, decreasing the melt wetting on the crystal and then reducing the cost of energy for bubble nucleation given for the surface tension (e.g. Shea 2017).

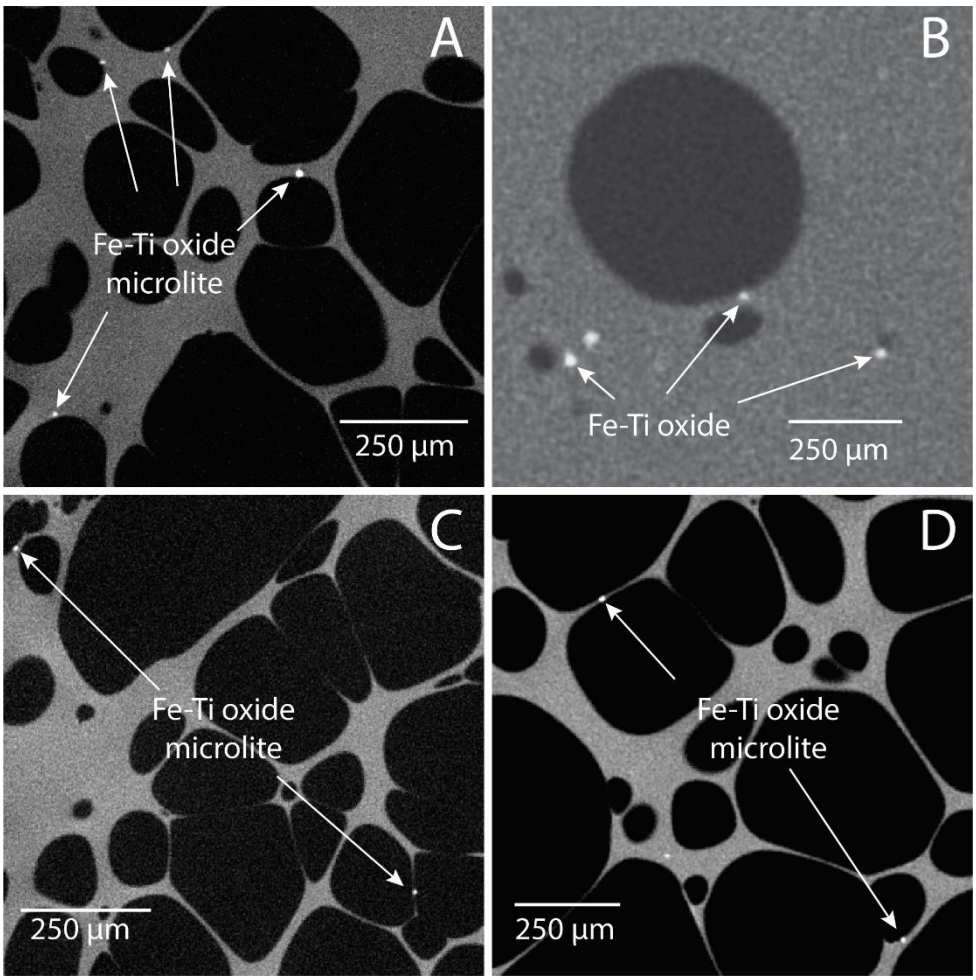

Figure 6.5. Tomography images of the relation between Fe-Ti oxides microlites and gas phase bubbles. (**A**) and (**B**) show the bubble-microlite contact in the samples subjected to 993 $°C$ and 947 $°C$ respectively. (**C)** and (**D**) show this contact and the presence of Fe-Ti oxide microlites in the thin melt films between bubble. Note that even when the crystals are in melt films of $\sim 1\ \mu m$ −thin the bubbles do not coalesce.

It can be observed a similar order of magnitude between the crystal number density of microlites and bubble number density is observed in LdM vitrophyric rhyolite ($N_c = 5.1\ x\ 10^1\ mm^{-3}$ and $N_b = 2.1 - 7.4\ x\ 10^1\ mm^{-3}$ respectively), it can be noticed that they are in the same order of magnitude. Shea (2017) discussed the benefits of using 3D textural analysis instead of 2D analysis using SEM images in order to compared oxides and bubble number densities and get insights on the nature of nucleation (heterogenous versus homogeneous). He showed that 2D textural analysis reduces the likelihood of intersecting a contact point between a microlite and the orders-of-magnitude larger bubble, causing an underestimation of the oxides number density when analysed in the 2D images. In this sense, the lack of ubiquitous contact points between oxides and bubbles from 2D images cannot be

taken as a reason that the oxides were not the nucleation sites of these bubbles. Instead, when analysing the 3D volume acquired with X-ray computed tomography, it can be clearly observed the contact points and the positive correlation between oxides and bubbles (Fig. 6.5). Additionally, no contact between plagioclase microlites and bubbles was observed. From this it is possible to confirm a direct control of the number density of Fe-Ti oxides on the bubble number density and the heterogeneous nature of bubble nucleation in these experiments.

Bubbles are also observed in direct contact with phenocrysts of plagioclase, biotite and Fe-Ti oxides. It is observed groups of bubbles surrounding these phenocrysts (e.g. Fig 6.6B). This may also indicate heterogeneous bubble nucleation on phenocrysts. Some of these bubbles surrounding phenocrysts show high degrees of coalescence, which is inferred by the preserved shape of bubbles showing features of former inter-bubble films (e.g. Fig. 6.6). This observation is discussed in the following section.

6.3.2 Coalescence and outgassing enhanced by phenocryst phases

Previous experiments conducted on microlite-bearing magma (e.g. Oppenheimer et al., 2015; Lindoo et al., 2017; Colombier et al., 2020) showed that microlites have a considerable effect on bubble coalescence and gas percolation, when their abundance is relatively high ($\geq \sim 20\ vol.\%$; Lindoo et al., 2017). This effect is mainly related to space limitation created by the crystals promoting bubble connectivity. However, this effect is not present here due to the low crystallinity of the samples ($\sim 4.5\ vol.\%$).

In this study, the samples do not reach percolation (system-spanning coalescence), but a considerable degree of bubble coalescence (Fig. 6.6A-E), especially when compared to the crystal-poor Krafla obsidian (Fig. 6.6F). Coalescence occurs mostly around phenocrysts with high aspect ratio (Fig. 6.6A-D), in agreement with numerical modelling (e.g Saar et al., 2001; Walsh and Saar, 2008) and previous experiments (Spina et al., 2016; Lindoo et al., 2017), whereas it is not observed associated to microlites (Fig. 6.5). Coalescence occurs associated to phenocrysts of feldspars, biotites and Fe-Ti oxides with indistinguishable influence among the mineral phase. The effect of phenocrysts is to locally promote bubble concentration by heterogenous nucleation, which consequently promotes coalescence due to the smaller distance between bubbles and some degree of deformation due to the presence of larger crystals such as phenocrysts.

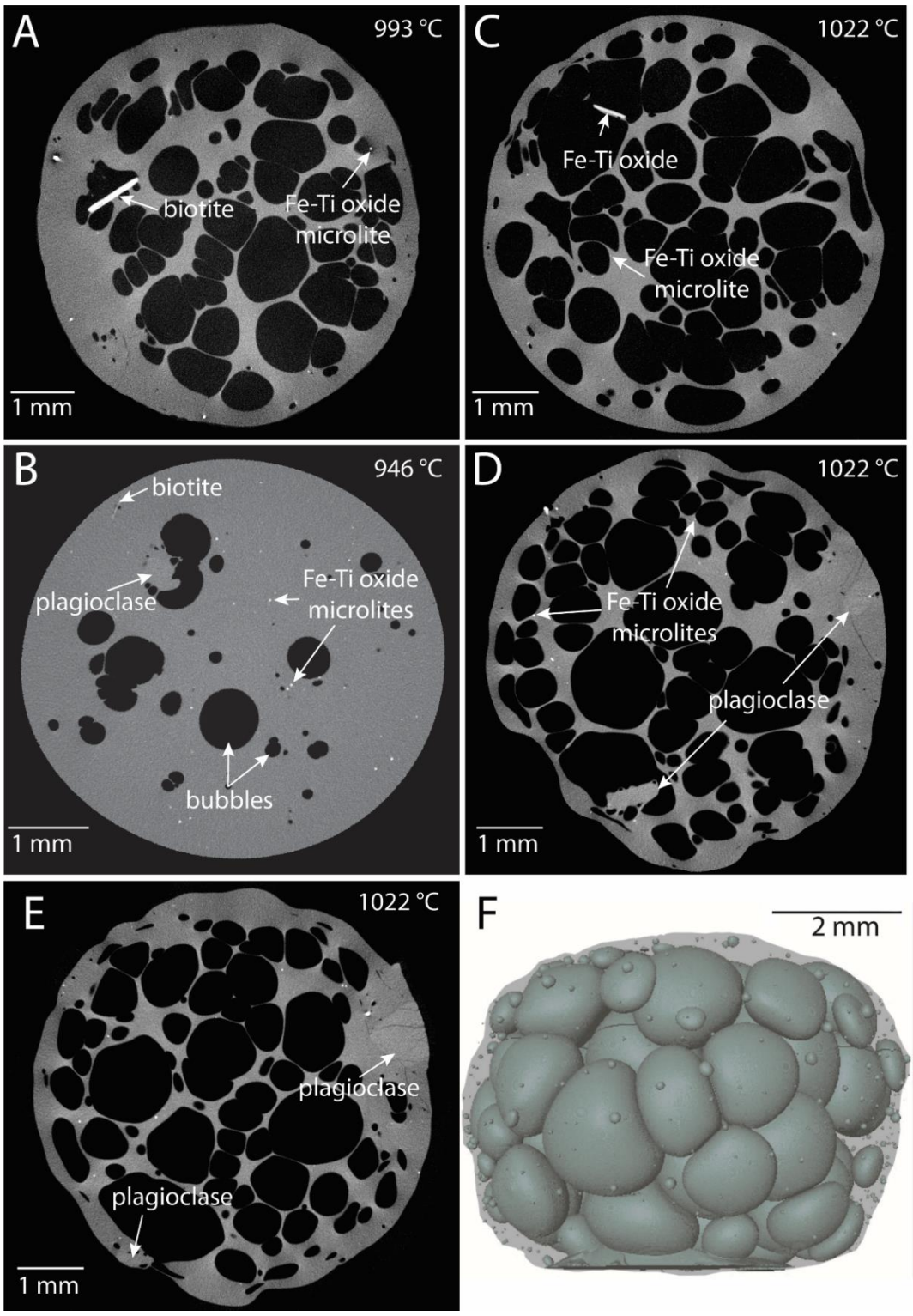

Figure 6.6. Phenocryst-coalescence relationship. This relationship is shown in 2D images of X-ray computed tomography analyses to post-experimental samples. Most of the coalesced bubbles are associated to phenocrysts of every type. (**A**), (**B**) and (**C**) represent experiments at 993 $°C$, 946 $°C$ and 1022 $°C$ respectively. (**D**) and (**E**) represent other regions of the sample subjected to 1022 $°C$. Images are shown in high contrast in order to better distinguish between plagioclase phases and glass. (**F**) computed tomography reconstruction of the higher porosity reached by samples of the Krafla obsidian subjected to 1000 $°C$ (see Chapter 4). Notice that even at high porosities ($\sim$0.6) bubbles do not coalesce, even when bubble start pushing against each other.

Phenocrysts also cause bubbles connection with the exterior of the sample (Fig. 6.6D,E), which leads to gas escape from the dense and impermeable, highly viscous dehydrated melt skin formed at the border of the sample (e.g. von Aulock et al., 2017). Additional thinning of the melt surrounding bubbles at the border of the samples, most likely driven by gas expansion, led the bubbles to reach the exterior allowing gas escape and form remaining flattened bubbles (Fig. 6.7). This last process is inferred from the length and shape of the flattened bubbles coincident with the length of the sample depressions. Outgassing in this case occurs by localised bubble opening at the sample border and not due to the development of a system-spanning connected porous network. However, there can be a small contribution to outgassing from the porous network when bubbles connect to fractures (Fig. 6.6D). The last point may explain the absence of bubbles in the vicinity of the phenocrysts in which fractures developed. All these processes favour outgassing of the magma and are likely responsible for the sample shrinkage observed in experiments conducted at temperatures higher than $1000\ °C$. I propose that phenocrysts, particularly those presenting high aspect ratio, enhance bubble coalescence in a much higher extent than microlites and favour gas escape in low crystallinity magmas.

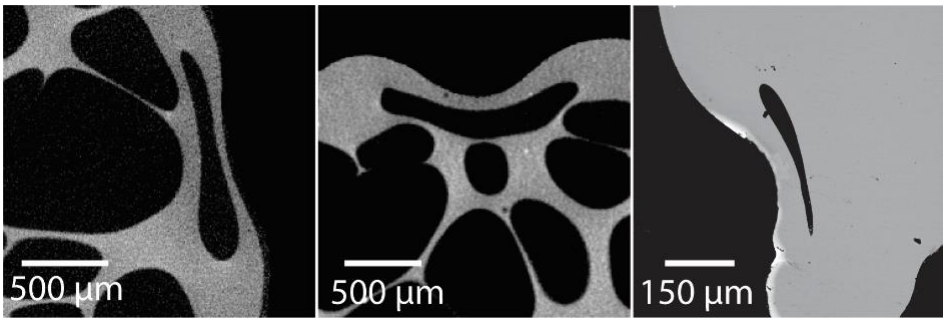

Figure 6.7. Gas escape from bubbles at the border of the samples. The flat shape of the bubbles is an evidence of remaining gas bubble after connection with the atmosphere and subsequently melt healing. Examples in samples subjected to $1022\ °C$. Brighter sample border in last image represents an artifact.

Moreover, outgassing for these samples with low initial water concentration and crystal content occurs at porosities between $0.55 - 0.59$ (Fig. 6.4). From this point, the final porosity reached by every sample decreased while temperature increased, i.e. the extent of outgassing increased accordingly. The porosity at which permeability developed for phenocryst-bearing rhyolitic magmas was found to be between 0.45-0.50 (deGraffenried et al., 2019), with a minimum crystal load of $20\ vol.\%$ (Lindoo et al., 2017; deGraffenried et al., 2019). As mentioned in the previous section, the samples in this study did not reach percolation but only local coalescence and outgassing for bubble connection to the exterior. However, the presence of a considerable amount of microlites such as those in these samples ($\sim 5\ x\ 10^1\ mm^{-3}$) may move a magma closer to reach percolation than magmas with lower amount of microlites (Fig. 6.8). This is based on a porosity and bubble size criteria (Burgisser et al., 2017) and occurs because a high

bubble number density reduces the average bubble size and inter-bubble distances, and then the propensity for bubbles to touch each other (e.g. Gonnermann and Manga, 2007). Considering the correlation between high crystal and bubble number densities, higher number densities of Fe-Ti oxides microlites can produce a higher bubble number density and the potential for a vesiculating magma to cross the percolation threshold at a given porosity increases (Fig. 6.8). However, the observation that abundant oxide microlites are present in the thin inter-bubble films (Fig. 6.5C-D), suggests that bubble coalescence is prevented at least in the timescales of the experiments. Effect that is promoted in earlier stages by phenocrysts.

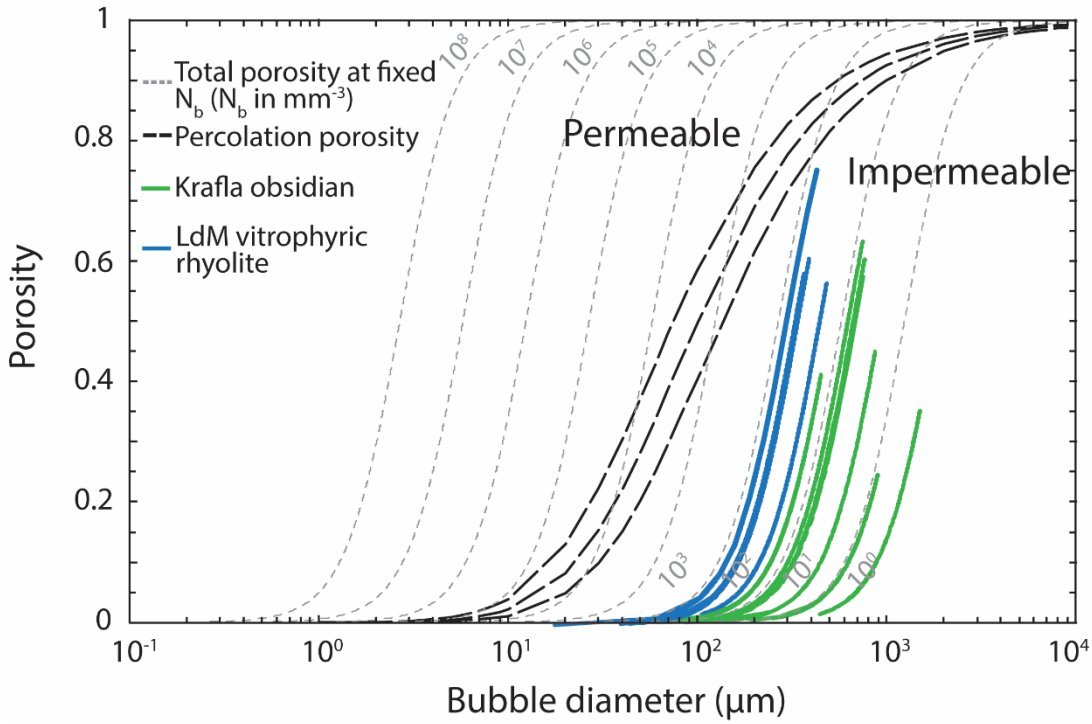

Figure 6.8. Porosity versus bubble diameter calculated for a given bubble number density. Bubble diameter was calculated as $d = 2r$ with r calculated according to equation 3. Bubble number densities used are those measured with computed tomography and scanning electron microscope. Permeable and impermeable fields are plotted according to the size criteria of Burgisser et al. (2017), where thick black dotted lines represent the division field according to the percolation porosity equation therein. Thin grey dotted lines represent the porosity/bubble diameter for a monodisperse bubble distribution at every bubble number density.

6.3.3 Influence of viscosity

Both types of sample differ mainly in their crystal content and the iron concentration in the glass, with a slight difference in the concentration of water. Even though both samples have a rhyolitic composition, these textural and chemical differences induce a lower viscosity

for the Krafla obsidian than for Laguna del Maule rhyolite. Previous studies showed that slight changes in the water concentration of a rhyolitic melt can make great changes in viscosity (e.g. Hess and Dingwell 1996). At atmospheric pressure, a difference of $\Delta 0.05\ wt.\%$ between $0.10 - 0.15\ wt.\%$ H_2O can produce an increase in viscosity of ~ 0.4 log units at temperatures between $900 - 1000\ °C$. However, this viscosity difference given by a lower or higher water content disappears when the two samples are subjected to the same dwell temperature at water supersaturation condition, at which water concentration in the melt is considered to be equivalent for both rhyolitic cases (e.g. Liu et al., 2005). On the other hand, variations in crystal content and iron concentration in both magmas can also produce differences in the magma viscosity.

Iron content was shown to have a significant effect on melt viscosity (e.g. Dingwell and Virgo 1989; Liebske et al., 2003; Bouhifd et al., 2004). Calculated viscosity for the two samples types using Giordano et al. (2008), at temperatures between $900 - 1000°C$ and water concentration equal to its solubility at atmospheric pressure (Liu et al., 2005), vary for up to 0.2 orders of magnitude driven by the difference in composition. A higher viscosity hinders bubble growth and bubble mobility, so the main differences in coalescence and connectivity-driven outgassing between the two sample types are driven by their different crystal content rather than a viscosity effect.

6.3.4 Implications for silica-rich magma reservoirs

Erupted silicic magma commonly contain phenocrysts (also considering micro-phenocrysts) in crystal number densities in the range of $\sim 10^{-4} - 10^{1}\ mm^{-3}$ (e.g. Cashman, 1988; Sparks et al., 1994; Bindeman, 2003; Gualda and Rivers 2006; Cluzel et al., 2008). On the other hand, magnetite microlites are often present in silicic magmas with common abundances between $\sim 10^{0} - 10^{2}\ mm^{-3}$ (Cashman 1988; Gualda and Rivers 2006; Cluzel et al., 2008), but they can reach values as high as $\sim 10^{5} - 10^{6}\ mm^{-3}$ (e.g. Colombier et al., 2017b). The nature and number density of phenocrysts and microlites of our experiments are comparable to those of erupted natural rhyolitic magma.

These experiments also involved heating as the mechanism that drives solubility loss. This allows to compare to natural systems such as shallow magmas emplaced as lava domes, plugs or degassed caps, for which heating-induced vesiculation has been suggested to occur (Lavallée

et al. 2015). However, silica-rich magmas usually have temperatures lower than 1000 °C (e.g. Almeev et al., 2012), for which the most plausible scenario would be the one that happens in the experiments conducted below this temperature. This means that the presence of even low crystal contents (~4.5 %) may promote bubble formation and coalescence in shallow silica-rich magmas during degassing. A scenario with a magma containing a higher number density of Fe-Ti oxide microlites could have two opposite effects. First, it may promote heterogeneous bubble nucleation and growth, both enhancing magma explosivity. On the other hand, the presence of phenocrysts and high microlite number density may promote coalescence and move the magma closer to gas percolation, which may cause a reduction of explosivity.

The final implications of these finding may be for more crystalline systems. For instance, high abundance of phenocrysts may promote localised nucleation and coalescence, allowing large coalesced bubbles associated to phenocrysts to connect each other. This can promote percolation and gas escape at earlier stages (deeper) in the conduit. Microlites may also promote coalescence and outgassing at high crystallinities in more shallow parts of the conduit (e.g. Lindoo et al., 2017). In such a case, the effusion of a lava dome or flow would be promoted over an explosive eruption. Phenocryst contents of ~ 45 vol.% together with a ~35 vol.% microlites have been measured in the dacitic lava dome of the effusive phase of the 1980-1986 eruption of Mt St Helens, USA (e.g. Calder et al., 2015). The same volcano showed increased crystallinities in its 2004-2008 eruption, where initial ~70% crystals increased to 98 vol.% by the end of the eruption, when a complete degassed magma was erupted. This highly crystalline lava domes can also be observed in the cases of the volcanoes Unzen in Japan (~10 vol.% phenocrysts and 20 vol.% microlites), Colima in Mexico (~25 vol.% phenocrysts and 15 vol.% microlites), Anak Krakatau in Indonesia (~40 vol.% phenocrysts and 15 vol.% microlites) and Bezymianny in Rusia (~60 vol.% phenocrysts and 10 vol.% microlites) as shown by Lavallée et al. (2007).

6.4 Concluding remarks

This chapter has shown that the crystal number density of microlites, specifically Fe-Ti oxides, exerts a dominant control on the bubble number density while the role of phenocrysts or other microlite mineral phases on heterogeneous nucleation are more limited. On the other hand, phenocrysts enhance bubble coalescence and connectivity more and earlier than microlites in low-crystalline magmas.

When compared to bubble textures produced in a phenocryst-free rhyolitic magma, the magma with phenocrysts noticeably produced greater bubble coalescence and connectivity and it becomes clear the two mentioned effects.

These findings help to better understand the role that pre- and syn-eruptive crystalline phases may play in the degassing process during magma ascent towards the surface.

7

First insights into slow decompression scenarios for shallow rhyolitic magma

Chapter Summary

Explosive eruptions are the most powerful type of volcanic activity and they have produced devastating effects on population in history. They can result from magma interaction with external water, but in most of the cases they are modulated by the degassing dynamics of the ascending magma in the volcanic conduit. Magmatic fragmentation can occur in rhyolitic systems subjected to decompression during ascent, driven by supersaturation and exsolution of dissolved volatiles that forms gas bubbles. Bubble nucleation and growth in the high viscosity magma can accelerate the magma towards the surface. When bubbles growth isolated or gas escape is not efficient through connected pore networks, gas expansion may build-up overpressure that could eventually overcome the tensile strength of the accelerated magma and produce fragmentation. This chapter experimentally explores vesiculation and fragmentation occurring in shallow rhyolitic magma due to slow decompression. I conducted decompression experiments using a synthesised rhyolitic melt with ~2.1 $wt.\%$ H_2O concentration as starting material. The decompressions were performed at slow rates between $0.0007 - 0.34\ MPa\ s^{-1}$ from $32 - 35\ MPa$ to final pressures between $0.1 - 10\ MPa$. All decompressions were conducted at temperatures relevant for rhyolitic magmas between $775 - 875\ °C$. At these experimental conditions, the samples started from undersaturated to slightly saturated water conditions, producing final porosities φ between $0.07 - 0.87$. The results show that for

complete decompression at $\sim 0.1\ MPa\ s^{-1}$ or faster, shallow rhyolitic magmas between $800 - 875\ °C$ can fragment. Lower temperatures and lower decompression rates result, instead, in low-to-high porosities, but not producing magmatic fragmentation. This gives insights into the conditions favouring magmatic fragmentation in natural cases and the potential explosivity of shallow rhyolitic magmas.

7.1 Samples used and experimental conditions

For these decompression experiments, I used samples from the synthesised material Kb8, which corresponds to a very-low-crystal and -bubble ($<< 1\ vol.\%$, considered here as crystal- and bubble-free) content rhyolitic glass with $2.1 \pm 0.16\ wt.\%$ initial water concentration (see Chapter 3 for details). The initial samples for all experiments are cylinders of $\sim 5\ mm$ diameter and $\sim 3\ mm$ length and free of visible fractures.

The samples were placed into the decompression autoclave in which the pressure was built up by adding pressurised Ar gas, following the procedure in Chapter 3 (Fig. 3.6). A minimum pressure between ~9-12 MPa of Ar was first reached and then temperature was increased by heating the autoclave with the external furnace. The heating rate applied by the furnace was non-linear with an average of $\sim 19\ °C\ min^{-1}$. The gas pressure in the autoclave increased as a result of heating, reaching the targeted experimental pressure. Any excess of pressure over $32 - 35\ MPa$ was released to ensure stable conditions in the system as starting point for the experiments (Fig. 7.1A). Targeted initial P-T conditions for experiments were held for $\sim 5\ minutes$. After dwelling, the decompression was controlled by hand, opening a high precision gas valve that released the pressurised Ar following both linear and non-linear pressure-time paths (Fig. 7.1B-C). Linear decompression (Fig. 7.1B) was applied by releasing the Ar gas to the pulse of a sound timer previously programmed for emitting a sound every $1-10\ s$ used as control points. Between every sound, the amount of gas continuously released was the same and it was precisely monitored ($\Delta P = 0.01\ MPa$) with a manometer and measured by the pressure transducer. On the other hand, non-linear decompression (Fig. 7.1C) was applied by partially opening a controlled amount the gas valve only once, and then left to freely release gas until the final targeted pressure.

After decompression, the samples were rapidly quenched by removing the furnace and applying compressed air to the exterior of the autoclave (Fig. 7.1A). Air was constantly applied

until the temperature of the sample reached 400 °C, which is below the glass transition temperature for the original pre-experimental material and then also for all the vesiculated the samples. This procedure allowed to reach the final quench temperature in ~2 to 3 $minutes$, depending on the experimental temperature. Finally, the samples were left to freely cool down to room temperature (~22 °C) and recovered for analyses. In the cases of samples decompressed until 5 and 10 MPa, the pressure was kept during quench by adding pressurised Ar at every pressure drop resultant from the decreasing temperature. Again, this procedure was followed until the samples reached 400 °C and then the pressure was allowed to decrease according to the decrease of temperature. Finally, at room temperature, the last remaining gas pressure was slowly decreased until atmospheric pressure at unmonitored rates before recovering for analyses.

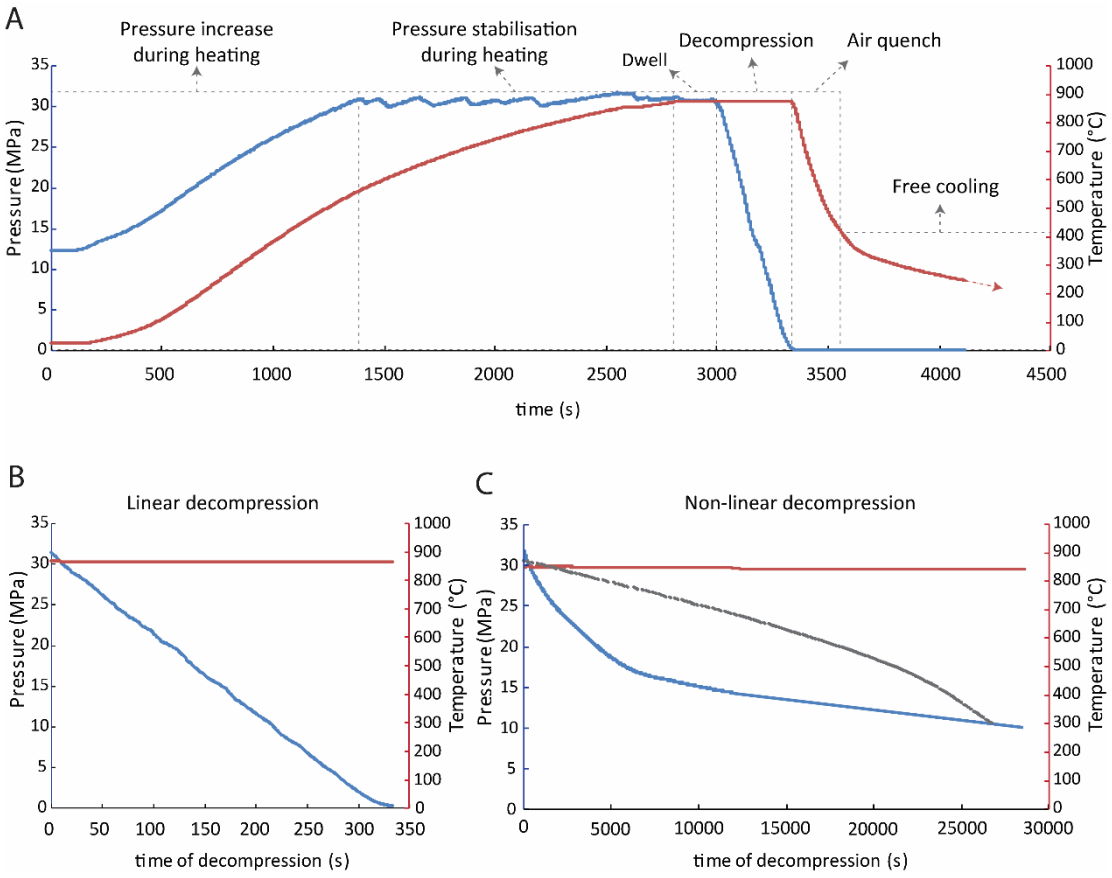

Figure 7.1. Pressure and temperature profiles in decompression experiments. (**A**) Real experimental profile from decompression at ~0.09 $MPa\ s^{-1}$ and 875 °C. Profile starts from pressurised initial conditions at room temperature and includes: heating, dwell, decompression and quench phases. (**B**) Real profile of a linear decompression at ~0.09 $MPa\ s^{-1}$ and 875 °C. (**C**) Real profile of a non-linear decompression at ~0.0007 $MPa\ s^{-1}$ (average decompression) and 850 °C. Grey line represents a real non-linear profile which is not at scale and only referential. This last profile corresponds to a non-linear decompression ~0.06 $MPa\ s^{-1}$ (average decompression) and 850 °C.

7.2 Results

Independently of the decompression rate, all samples showed expansion driven by bubble growth (called vesiculation hereafter) at different extents within the range of experimental conditions. Samples are classified according to two main behaviours: (1) vesiculation and (2) vesiculation + fragmentation, the last one called only fragmentation hereafter. Samples linearly decompressed until atmospheric pressure and at rates of $\sim 0.1\ MPa\ s^{-1}$ or higher show the two behaviours, depending on the experimental temperature (Fig. 7.2). Those samples at temperatures between $800 - 875\ °C$ fragmented during vesiculation, while that sample at $775\ °C$ vesiculated only. Samples linearly and non-linearly decompressed at rates of $\sim 0.06\ MPa\ s^{-1}$ or lower show only vesiculation at different degrees.

Porosities vary between $0.82 - 0.87$ for all fragmented samples (Figs. 7.2D and 7.3) and between $0.07 - 0.85$ for the vesiculated ones (Fig. 7.3 and 7.4). For samples decompressed until 5 or $10\ MPa$, porosities reached between $0.07 - 0.46$ independently of the decompression path, i.e linear or non-linear. Porosity values are proportionally inverse to the decompression rate applied, where low porosities correspond to high decompression rates and high porosities to low decompression rates. Bubble coalescence was observed in samples stopped at intermediate pressures (Fig. 7.4) of 5 and $10\ MPa$ and it was not evident in samples decompressed until atmospheric pressure.

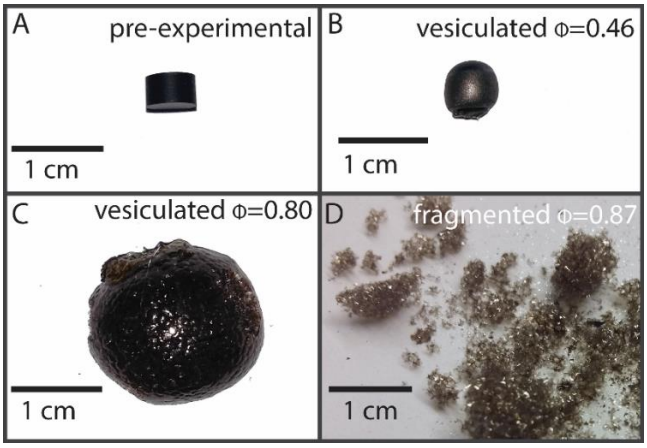

Figure 7.2. Images of a pre-experimental sample and different types of post-experimental samples. (**A**) Shows a cylinder of 5 mm diameter and 3 mm length. (**B**) Shows a vesiculated (porosity 0.46) sample decompressed until 10 MPa at $\sim 0.02\ MPa\ s^{-1}$ and 850 $°C$. (**C**) Shows a highly vesiculated (porosity 0.80) sample decompressed until 0.1 MPa at $\sim 0.02\ MPa\ s^{-1}$ and 850 $°C$. (**D**) Shows a fragmented (porosity 0.87) sample decompressed until 0.1 MPa at $\sim 0.1\ MPa\ s^{-1}$ and 875 $°C$.

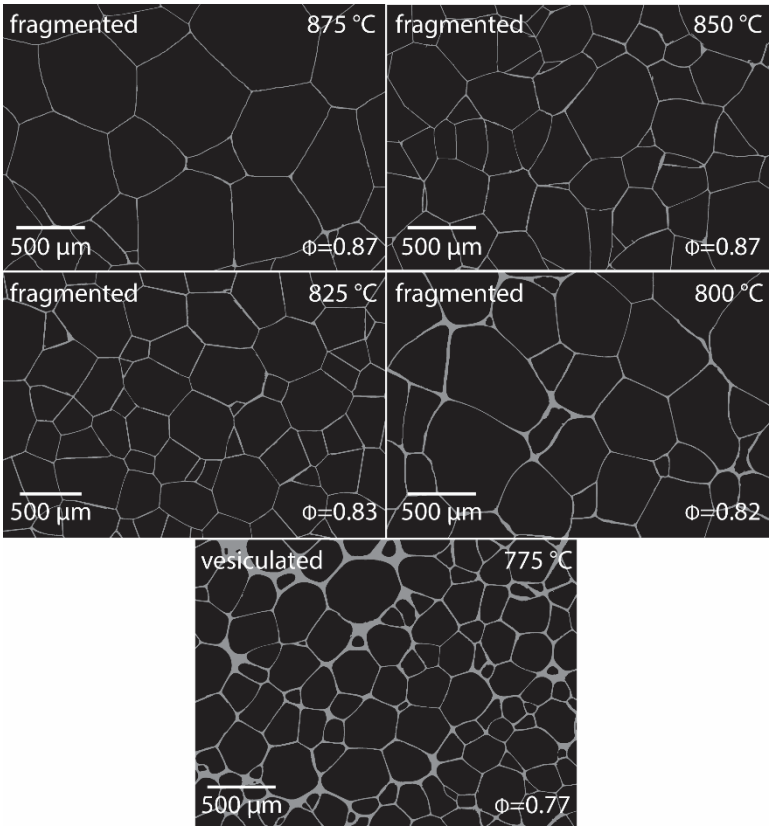

Figure 7.3. Post-experimental SEM images of samples decompressed at ~0.1 $MPa\ s^{-1}$ and different temperatures. Sample at 775 °C vesiculated only. For samples between $800 - 875\ °C$ images correspond to fragments. There is visible increase in the melt fraction and decrease of porosity towards lower temperatures.

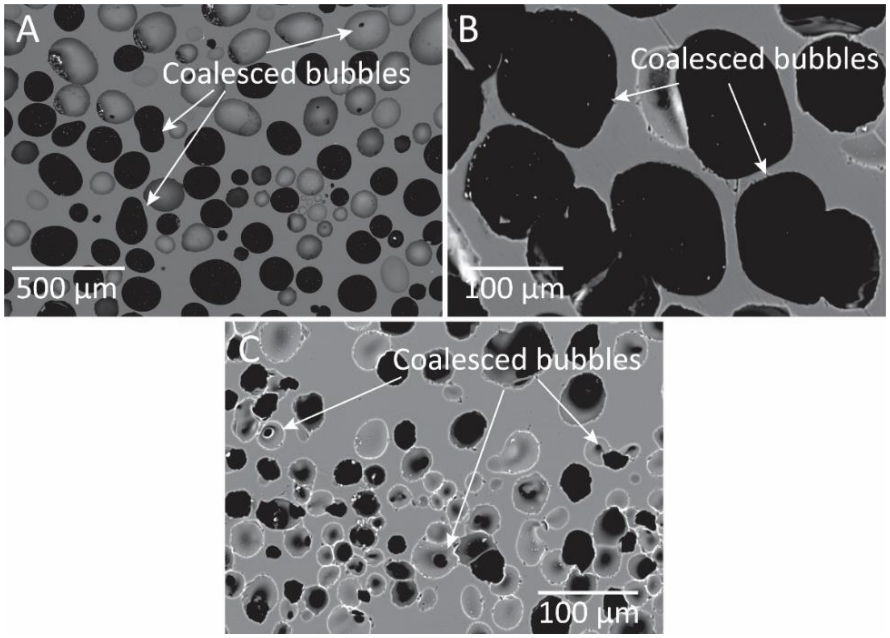

Figure 7.4. SEM images of samples decompressed until intermediate pressures. (**A**) Sample decompressed until $P_f = 10\ MPa$ at ~0.0007 $MPa\ s^{-1}$ ($\phi = 0.42$), (**B**) Sample decompressed until $P_f = 5\ MPa$ at ~0.1 $MPa\ s^{-1}$ ($\phi = 0.52$), (**C**) Sample decompressed until $P_f = 10\ MPa$ at ~0.05 $MPa\ s^{-1}$ ($\phi = 0.33$).

Table 7.1. Data for decompression experiments. Types are the behaviour between fragmented (f) and only vesiculated (v). Linear and non-linear decompressions are represented in Figure 7.1.

Sample	T (°C)	Pi (MPa)	Pf (MPa)	dP/dt (MPa s^{-1})	Porosity	Nb (mm^{-3})	Type
Linear decompression at variable temperature							
Kb8-Dec-01	875	32	0.1	0.0917	0.87	$3.1x10^2$	f
Kb8-Dec-02	850	32	0.1	0.0938	0.87	$7.3x10^2$	f
Kb8-Dec-03	825	33	0.1	0.0949	0.83	$4.8x10^2$	f
Kb8-Dec-04	800	33	0.1	0.0926	0.82	$2.2x10^2$	f
Kb8-Dec-05	775	33	0.1	0.0948	0.77	$7.9x10^2$	v
Linear decompression at variable decompression rate							
Kb8-Dec-02	850	32	0.1	0.0938	0.87	$7.3x10^2$	f
Kb8-Dec-07	850	32	0.1	0.0239	0.80	$1.5x10^3$	v
Kb8-Dec-17	850	32	0.1	0.0497	0.85	$1.2x10^3$	v
Kb8-Dec-18	850	32	0.1	0.0049	0.78	$8.6x10^2$	v
Kb8-Dec-21	850	35	0.1	0.3391	0.82	$1.2x10^3$	f
Non-linear decompression to intermediate pressure							
Kb8-Dec-08	850	32	10	0.0007	0.42	$6.6x10^2$	v
Kb8-Dec-10	850	32	10	0.0194	0.46	$6.2x10^3$	v
Kb8-Dec-11	850	33	10	0.0622	0.07	$3.8x10^2$	v
Linear decompression to intermediate pressure							
Kb8-Dec-01	875	32	0.1	0.0917	0.87	$3.1x10^2$	f
Kb8-Dec-14	875	33	10	0.0494	0.33	$8.6x10^3$	v
Kb8-Dec-15	875	34	10	0.0995	0.09	$5.2x10^2$	v
Kb8-Dec-16	875	33	5	0.0990	0.52	$3.6x10^3$	v

Bubble number densities N_b are in the order of $\sim 10^2\ mm^{-3}$ for fragmented samples and between $10^2 - 10^3\ mm^{-3}$ for only vesiculated ones (Fig. 7.5). Samples decompressed until pressures of 5 and 10 MPa show slightly higher values of bubble number density than those decompressed until atmospheric pressure. Additionally, there is no clear correlation between decompression rate and bubble number density.

Post-experimental samples remain phenocryst-free and only Fe-Ti oxide microlites are sporadically found. These microlites population is not different to that found in the pre-experimental material. However, the whole range of vesiculated post-experimental samples show nanolites crystallised in the inter-bubble groundmass. These nanolites correspond to Fe-Ti oxides, identified by Raman analyses (Fig. 7.6). Nanolites crystallised more in samples with higher degree of vesiculation and less in those with lower degree of vesiculation, revealed by the intensity of the Raman peak and qualitative analyses of SEM images.

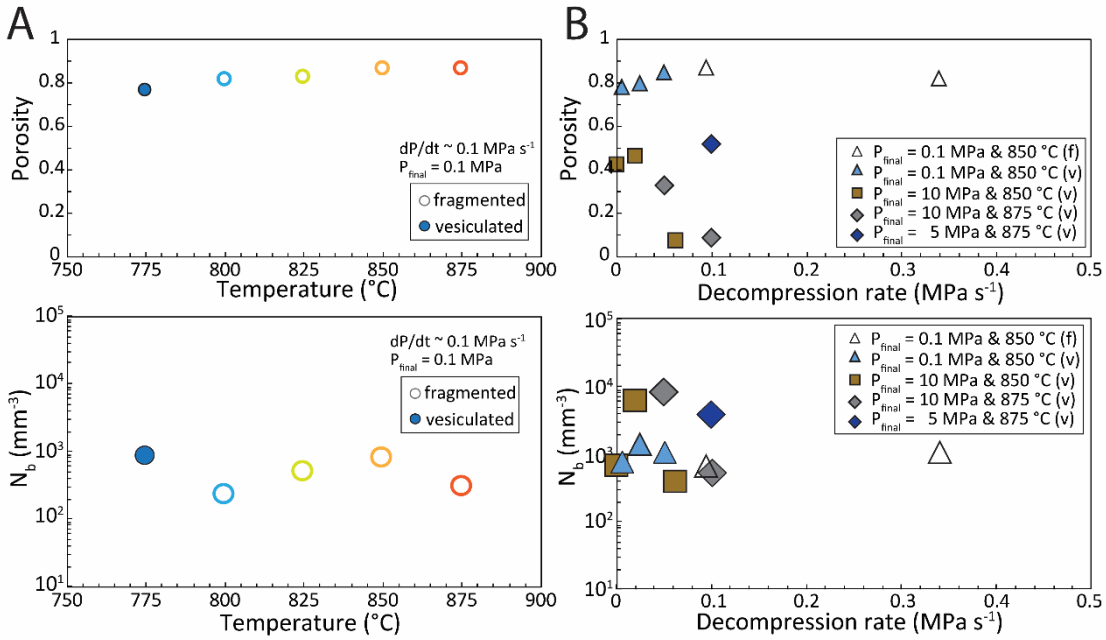

Figure 7.5. Porosity and bubble number density of decompressed samples. (**A**) Samples subjected to $\sim 0.1\ MPa\ s^{-1}$ at different temperatures. Colours represent different temperatures according to those used in other figures for comparison. (**B**) Samples subjected to different decompression rates at 850 °C and 875 °C. Triangles represent samples decompressed until atmospheric pressure. Squares represent samples decompressed until $10\ MPa$ at $850\ ^{\circ}C$ and diamonds represent samples decompressed until $5\ MPa$ (blue) and $10\ MPa$ (grey), both samples at $875\ ^{\circ}C$. Filled symbols represent vesiculated samples and open symbols represent fragmented samples. All errors are lower than symbols size.

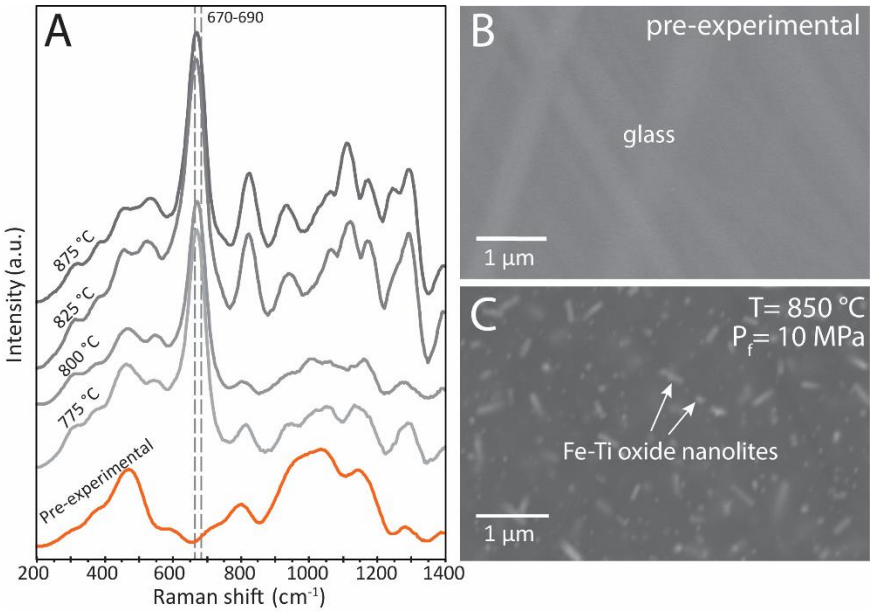

Figure 7.6. Raman spectra and SEM images for pre- and post-experimental samples. (**A**) In orange is the average $(n = 5)$ spectrum for the pre-experimental material Kb8. In grey are the spectra for experiments conducted at decompression rates of $\sim 0.1\ MPa\ s^{-1}$ and at different temperatures between $775 - 875\ ^{\circ}C$. (**B**) SEM image of pre-experimental material. (**C**) SEM images of post-experimental samples decompressed until $10\ MPa$ at $\sim 0.2\ MPa\ s^{-1}$ and $850\ ^{\circ}C$ show $\sim 8\ vol.\%$ nanolites in the groundmass.

7.3 Discussion

Decompression experiments in vesicular silica-rich magmas or magma analogues at magmatic temperatures that managed to fragment samples have only been done using extremely high decompression rates (e.g. $\sim 40\ MPa\ ms^{-1}$, Alidibirov and Dingwell, 1996; $\sim 5 - 23\ MPa\ ms^{-1}$, Martel et al., 2000; 2001; $1 - 100\ GPa\ s^{-1}$, Spieler et al., 2004). In those experiments, the initial samples were already porous before the fast decompression and then overpressurised. The fragmentation process occurred layer-by-layer where the overpressurised pore layer at the upper surface of the sample bursts and triggers the bursting of the next underlying pore layer (e.g. Alidibirov and Dingwell, 2000; Martel et al., 2001; Fowler et al., 2010). On the other hand, magmatic vesiculation experiments managing to produce fragmentation were conducted in natural samples using extremely high heating rates at atmospheric pressure, by placing a room-temperature sample into a pre-heated furnace (Forte and Castro, 2019). In those experiments, bubbles nucleated and grew building-up overpressure that produced expansion of the samples at high rates driving fragmentation. In that case, only calculated decompression rates are given which are between $0.5 - 1.2\ MPa\ s^{-1}$. The experiments conducted in this study are the first ones exploring decompression-driven vesiculation managing to produce magmatic fragmentation using silicate melts in a range of slow decompression rates ($0.0007 - 0.34\ MPa\ s^{-1}$). In the following sections, different aspects of the vesiculation and fragmentation process achieved are discussed in order to better constrain these processes.

7.3.1 Equilibrium and disequilibrium degassing

For all of the experiments, the starting pressure and temperature allowed the magma to be undersaturated or slightly supersaturated in H_2O respectively (Fig. 7.7). Water solubility was calculated using the model of Liu et al. (2005) for every temperature within a range relevant for rhyolitic magmas including the experimental temperatures. Likewise, equilibrium porosity was calculated after Gardner et al. (1999), using the difference between the initial water concentration and the water solubility for each decompression path at every experimental temperature (Fig. 7.8). When decreasing pressure, the magma is subjected to supersaturated conditions and equilibrium phase separation should start to form gas phase bubbles (Fig. 7.8). However, most of the samples vesiculated in non-equilibrium conditions (Fig. 7.9). Where those samples subjected to the lowest decompression rates vesiculated closer to equilibrium

conditions than those subjected to the highest rates. Disequilibrium degassing during magma ascent, and hence decompression, occurs when bubble nucleation has a delayed response to supersaturation conditions. This is driven by the lack of a minimum supersaturation pressure in order to overcome the energy barrier that is provided by the surface tension (e.g. Gonnermann and Manga 2007; 2012). Disequilibrium degassing promotes water exsolution at higher rates than equilibrium conditions after nucleation occurs (Mangan and Sisson, 2000; Shea 2017), producing and accelerated bubble growth that is resisted by the highly viscous melt. This is the main cause of gas overpressurisation and accelerated bubble expansion capable to reach fragmentation (e.g. Massol and Jaupart, 1999; Gonnermann, 2015; Forte and Castro, 2019).

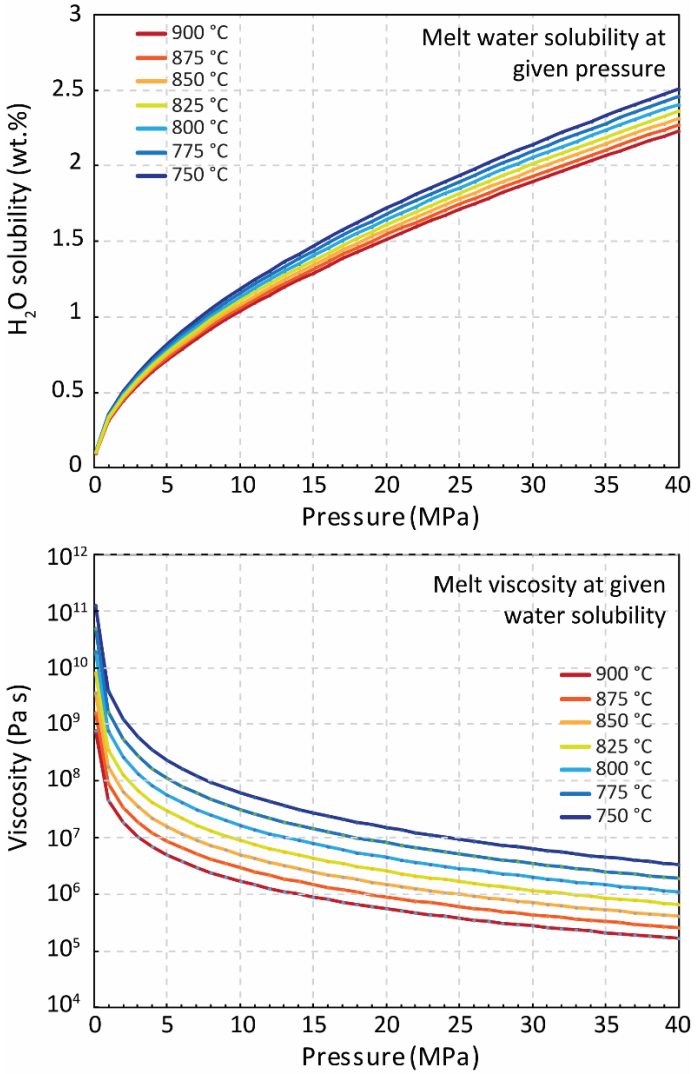

Figure 7.7. Water solubility and melt viscosity for a rhyolitic composition subjected to decompression. Curves are shown at different temperatures. Water solubility is calculated according to Liu et al. (2005) and melt viscosity is calculated using Hess and Dingwell (1996) with the computed water solubility at different pressures. Plots are shown in a temperature range significant for rhyolitic magmas between $T = 750 - 900\ °C$, including the experimental temperature range of $T_{exp} = 775 - 875\ °C$.

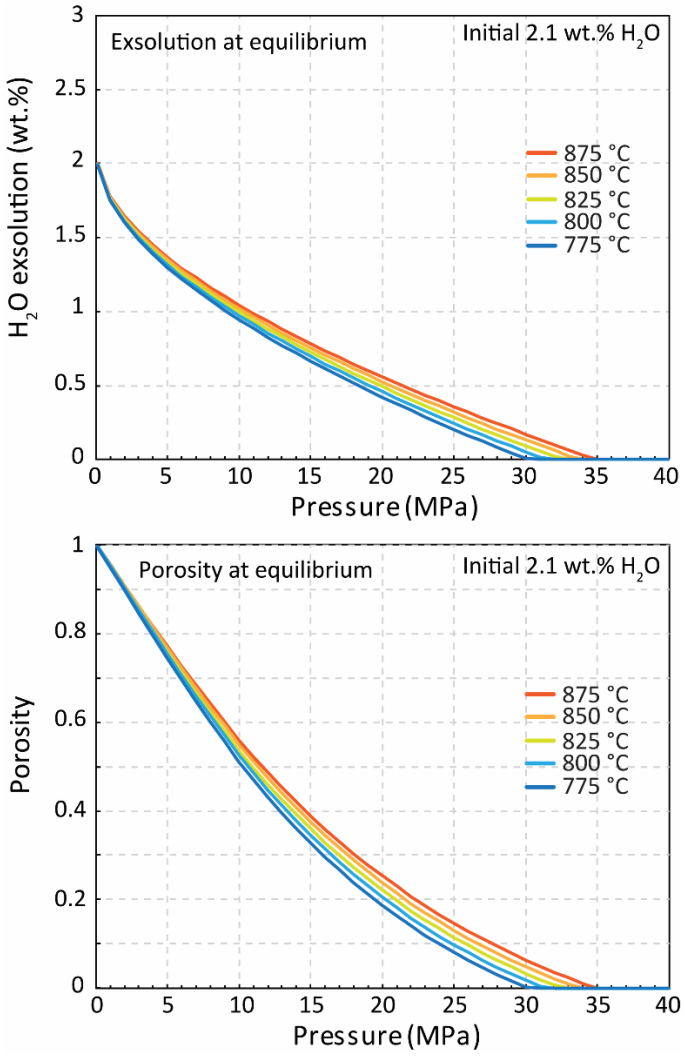

Figure 7.8. Exsolved water and its equilibrium porosity calculated for Kb8 sample. The amount of exsolved water is calculated as the difference between initial water concentration and the water solubility at every P-T condition. Water solubility is calculated according to Liu et al. (2005) and equilibrium porosity is calculated according to Gardner et al. (1999) for a rhyolitic composition using the amount of water exsolved at different pressure for each experimental temperature $T_{exp} = 775 - 875\ °C$.

On the other hand, those samples decompressed at the lowest rates (Fig. 7.9D) reached similar final porosities with slight variations ($\Phi = 0.42 - 0.46$). This suggests that both samples mark the point at equilibrium degassing, within a small variability expected between samples specimens. These equilibrium conditions were reached at a decompression rate of $\sim 0.02\ MPa\ s^{-1}$ or lower in these experiments. These results agree with the equilibrium degassing of volatiles into bubbles suggested to be between $0.025 - 0.25\ MPa\ s^{-1}$ for rhyolitic magma (e.g. Rutherford, 2008). At this decompression rate, water is then able to diffuse into bubbles in equilibrium, while at higher decompression rates degassing occurs mostly in disequilibrium conditions.

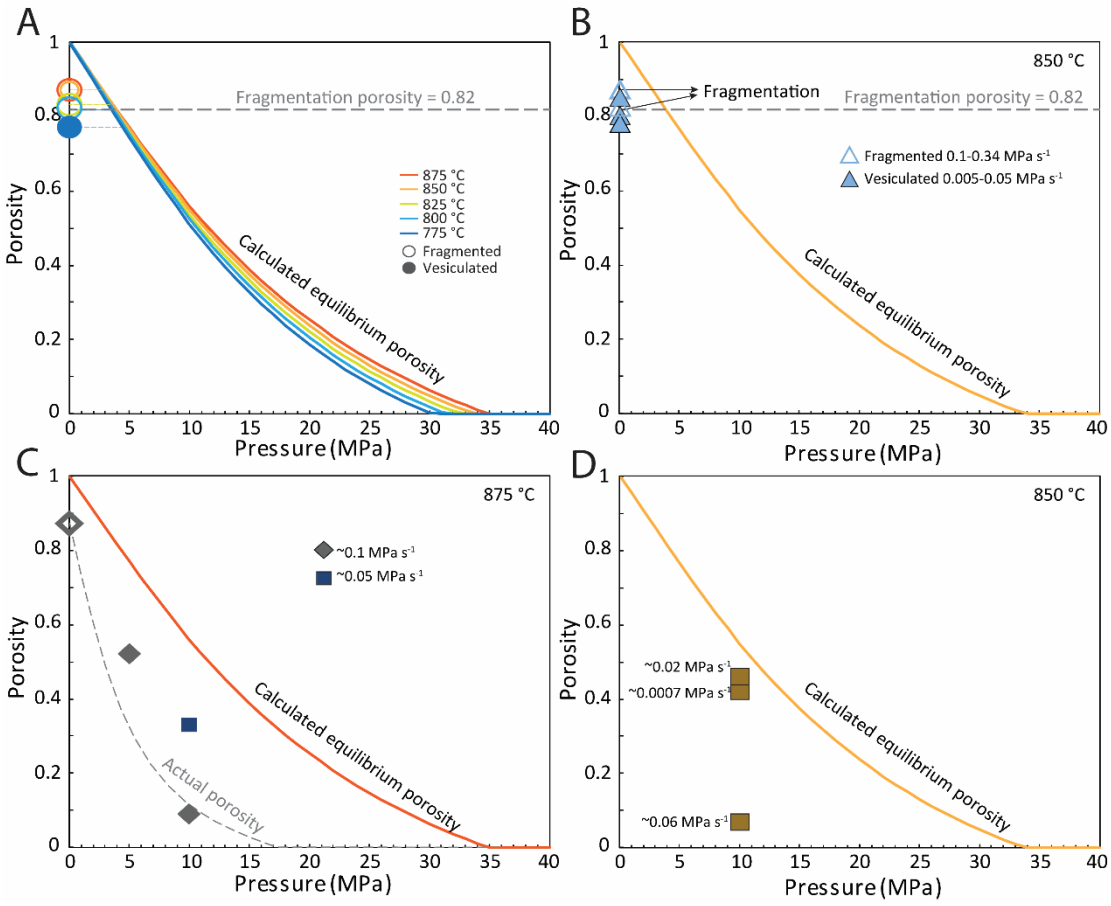

Figure 7.9. Porosities obtained for the difference experimental conditions. (**A**) Samples decompressed at ~0.1 $MPa\ s^{-1}$ and at difference temperatures. Fragmentation porosity represents the lowest porosity at which the shown samples fragmented. (**B**) Samples decompressed at variable decompression rates at $T_{exp} = 850\ °C$. Fragmentation porosity represents the lowest porosity at which the shown samples fragmented for decompression rates of ~0.1 $MPa\ s^{-1}$ or higher. (**C**) Samples decompressed until variable final pressures at ~0.1 $MPa\ s^{-1}$ and at $T_{exp} = 875\ °C$. Actual porosity curve (segmented grey line) was calculated with an exponential fitting of the porosity values representing decompression at ~0.1 $MPa\ s^{-1}$. An extra sample decompressed at ~0.05 $MPa\ s^{-1}$ is shown. (**D**) samples decompressed at variable decompression rates until $P_f = 10\ MPa$ at $T_{exp} = 850\ °C$. Filled symbols represent vesiculated samples and open symbols represent fragmented samples. All errors are lower than symbols size.

7.3.2 Bubble number densities

Bubble number densities (N_b) in the samples remain within a range comprising only two orders of magnitude independently of the temperature (Fig. 7.4) and decompression rate (Fig. 7.5) applied. N_b values in natural pumices have been inferred to be controlled by the decompression rate of ascending magmas (e.g. Toramaru 1995, 2006; Mourtada-Bonnefoi and Laporte 2004). Hamada et al. (2010) showed in decompression experiments how the bubble number density is not significantly affected by the temperature at given decompression rates,

but they vary as the decompression rate applied changes. In this study, the results agree with the independence of the bubble number density with temperature. However, the almost constant N_b values respect to decompression rate can be explained by bubble coalescence happening during bubble growth. The experiments decompressed until pressures higher than atmospheric (Fig. 7.5) show that coalescence already starts occurring at pressures as high as $10\ MPa$. This suggests that at high degrees of vesiculation, the samples may have suffered high degrees of bubble coalescence and they are not likely to preserve texturally the amount of bubbles nucleated. This has been shown as an issue for interpreting N_b data (e.g. Toramaru, 2006). The effect of bubble coalescence becomes more evident when comparing the bubble number density for atmospheric (fragmented) and intermediate (5 or $10\ MPa$; vesiculated) pressures at the same decompression rate (Table 7.1). Those decompressed samples stopped at intermediate pressures show slightly higher values compared to those decompressed until atmospheric pressure.

7.3.3 Bubble nucleation mechanism

The samples were able to vesiculate at all experimental decompression rates and temperatures. This range include final pressures as high as $10\ MPa$, with a total pressure difference of $\sim 22 - 35\ MPa$ between initial and final pressure. Furthermore, the absolute decompression was always equal or lower than $35\ MPa$. Water phase separation by homogeneous bubble nucleation normally requires high supersaturation pressures of at least $\sim 10\ MPa$ and can be greater than $100\ MPa$ (e.g. Mangan and Sisson, 2000; Mourtada-Bonnefoi and Laporte, 1999, 2002; 2004; Hamada et al., 2010; Gonnermann and Gardner, 2013), while heterogeneous nucleation can reduce the supersaturation pressure needed to nucleate bubbles to values normally below $20\ MPa$, that can even reach $\sim 1\ MPa$ (e.g. Gardner et al., 1999; Hurwitz and Navon, 1994; Gardner and Denis 2004). Thus, the decompression between $22 - 35\ MPa$ of these experiments is then likely to exsolve water by means of both homogeneous and heterogeneous bubble nucleation. But considering that the pre-experimental material showed a very low percentage of small bubbles and a scarce microlite content, heterogeneities in the glass are present in some extent. This means that heterogenous bubble nucleation is a more likely scenario for these experiments. I discard, however, the effect of nanolites in heterogeneous nucleation since the pre-experimental glass was proved nanolite-free and the bubble number densities are far below the resultant in pre-experimentally nanolite-bearing samples such as those studied in Chapter 4.

7.3.4 The role of crystals

After experiments, the samples remain mainly microlite- ($<< 1 vol.\%$) and phenocryst-free, but post-experimental samples show nanolites crystallised in the inter-bubble groundmass identified as Fe-Ti oxides by Raman analyses (Fig. 7.6). Since the pre-experimental material is nanolite-free and the peak at the $670 - 690\ cm^{-1}$ band of the Raman spectra becomes higher at samples with relative higher amount of water exsolved, I consider that the nanolite crystallisation responds to dehydration driven by water exsolution and is not greatly affecting bubble nucleation. However, in Chapter 5 it has been shown how nanolite crystallisation increases the viscosity of the magma by depleting the melt from total iron content, reducing Fe^{2+} respect to Fe^{3+}, increasing the relative abundance of SiO_2 and adding a crystal load to the magma. This increase in melt viscosity as a result of nanolite crystallisation in combination to the increase in viscosity driven by dehydration during degassing, may play a role in enhancing the brittle behaviour of the magma during fast vesiculation by moving the response of the melt closer to the glass transition (e.g. Dingwell, 1996).

7.3.5 Implications for shallow silica-rich magmas

A pressure between $32 - 35\ MPa$, such as those as starting conditions for these experiments, is equivalent to depths between $\sim 1.4 - 1.5\ km$, considering a magma density of $2300\ kg\ m^{-3}$. At these conditions, a rhyolitic magma between $800 - 875\ °C$ can contain a dissolved water concentration of $2.1 - 2.2\ wt.\%$ (Liu et al., 2005). In this study, the decompression experiments show that a magma at those conditions of pressure, temperature and concentration of dissolved water is capable to vesiculate up to ~87 vol.%, and in cases of magma ascent rates in the order of $\sim 4\ m\ s^{-1}$ (equivalent to $\sim 0.1\ MPa\ s^{-1}$), this magma has the potential to fragment and consequently produce an explosive eruption. Taking into consideration the dacitic eruption of Mt St Helens 1980, for instance, the explosive ascent rate calculated from mass eruption rate data is between $2 - 3\ m\ s^{-1}$ ($\sim 0.05 - 0.07\ MPa\ s^{-1}$), while the ascent rate was calculated at $\sim 0.08\ m\ s^{-1}$ ($\sim 0.02\ MPa\ s^{-1}$) for the later effusive eruptions (e.g. Rutherford, 2008). Additionally, the calculated decompression rates for the case of the rhyolitic explosive phase of Chaiten's 2008 eruption are $\sim 10\ MPa\ s^{-1}$ (Alfano et al., 2012), which occurred at magma temperatures between $780 - 825\ °C$ (Castro and Dingwell, 2009), i.e. decompression rates two orders of magnitude higher than those explored in this study that were able to fragment, overlapping in the temperature range between $800 - 825\ °C$.

Putting this in perspective, shallow rhyolitic magmas such as those stored at $\sim 2-8\ km$ depth (e.g. Laguna del Maule volcanic field and Krafla volcano) are likely to contain at least $2.3-2.6\ wt.\%$ H_2O dissolved and, more realistically, some percentage of bubbles of already exsolved volatiles (e.g. Wallace et al., 1995). Driven by the limitations of the experimental setup, it was not possible to explore higher initial pressures equivalent to those at $\sim 2\ km$ depth or more, where the amount of water dissolved in the magma is slightly higher. However, it has been shown in this chapter that subtle lower water concentrations are enough to produce high levels of vesicularity and even fragmentation. Moreover, in the case of Krafla volcano, the rhyolitic magma reservoir hit by a well was found to be at temperatures between $850-920\ °C$, with a dissolved water concentration of $\sim 1.8\ wt.\%$ (Elders et al., 2011; Zierenberg et al., 2012). According to the experimental results in this study and results found in other studies (e.g. Forte and Castro, 2019), such a magma meets the conditions necessary to develop either an effusive or explosive eruption, pending a triggering mechanism.

7.4 Concluding remarks

This chapter has given first insights into the vesiculation process of shallow rhyolitic magma through slow decompression experiments with a re-hydrated magma. The results show for the first time that magmatic fragmentation can be achieved by decompression-induced vesiculation at slow decompression rates.

The findings say that disequilibrium degassing plays an important role promoting fragmentation, which is directly related to the decompression rate applied.

The results also indicate that for initial water concentrations and temperatures expected in natural shallow rhyolitic magmas, continuous decompression until atmospheric pressure can result in magma vesiculation as high as $87\ vol.\%$, depending on the decompression rate applied. When the decompression rate reaches values of $\sim 0.1\ MPa\ s^{-1}$ or higher, the vesiculation process can produce magmatic fragmentation.

Compared to natural cases, the decompression rates applied in these experiments are in the range of magma ascent rate of naturally occurring highly explosive and effusive eruptions, where the results give insight into the potential explosivity of shallow rhyolitic magmas such as those found at Laguna del Maule volcanic field in Chile and Krafla volcano in Iceland.

8

Conclusions and outlook

In this thesis I explored the roles of nano- to millimetre sized crystals controlling several aspects of the dynamics of shallow silica-rich magmas. These magmas have produced some of the biggest explosive volcanic eruptions in history and some not erupted yet may have the potential to generate such an outcome. Magmas are subjected to decompression that leads to volatile loss, nucleation and growth of crystals and magma viscosity increases. I investigated these three key aspects that control the degassing dynamics and magma eruptive style from an experimental point of view. This section aims to summarise the main outcomes of this work and provide future lines of investigation.

I tested the influence of the presence of nanolites on gas bubble nucleation and growth dynamics by conducting vesiculation experiments in an optical dilatometer using both a nanolite-bearing and a nanolite-free rhyolitic magma. The results are remarkable, nanolites can dramatically increase the bubble number density ($10^{-1} - 10^{1}\ mm^{-3} \rightarrow 10^{6} - 10^{7}\ mm^{-3}$) and expansion rate in a degassing silicic magma. The increase in bubble number density is inferred to occur promoted by the high crystal number density of nanolites present in the samples. Nanolites showed to be efficient sites for heterogeneous bubble nucleation, compared to results with a nanolite-free magma of the same composition. These high bubble number densities also leaded to high bubble growth rates, mainly promoted by the shorter distances for water to diffuse into bubbles. These high bubble number density values are coincident with the highest bubble number densities reached in nature by some of the most explosive volcanic eruptions. This is an important observation on natural occurring textures, suggesting the possible presence of previously undetected nanolites in those natural magmas that produced highly explosive natural volcanic products.

I then investigated, by performing magma cooling experiments at highly controlled rates in an optical dilatometer, the process of nanolite crystallisation and the melt structure changes during the transition from a crystal-free melt to a nanolite-bearing magma. Nanolites crystallisation in magmas increases melt polymerisation, which has a direct effect increasing melt viscosity. These nanolites, when crystallising, enrich the melt in chemical components that are not uptaken by the forming crystals. In the case of Fe-Ti oxides, these deplete the melt in total iron which is directly related to an increase in melt viscosity too. These experiments were conducted at oxidising conditions and slow cooling rates, which are conditions relevant for shallow natural volcanic systems. Both the higher degree of melt polymerisation and the higher load of crystals due to the formation of nanolites in Fe-rich rhyolites are known to cause increases in magma viscosity.

I third performed heating-induced vesiculation experiments in a multiphase natural rhyolite, that shed light on the different roles played by microlites and phenocrysts on the degassing process of shallow silica-rich magma. I documented how the crystal number density of microlites, particularly Fe-Ti oxide microlites, exerts a dominant control on the bubble number density of the magma promoting heterogeneous bubble nucleation. Simultaneously, phenocrysts or other microlite mineral phases have a more limited effect on bubble nucleation, but specifically phenocrysts enhance bubble coalescence and connectivity in a higher extent and earlier than microlites. This occurs even at the low-crystallinity of the studied magma (~4.5 vol.%). However, compared to bubble textures produced in a phenocryst-free rhyolitic magma, the magma containing phenocrysts noticeably produced greater bubble coalescence and connectivity.

On the other hand, by conducting decompression experiments using a gas-pressurised hot autoclave and a re-hydrated rhyolitic melt, I give first insights into how vesiculation occurs in shallow rhyolitic magma when subjected to slow decompression. I showed, for the first time using silicate melts, that magmatic fragmentation can be achieved by decompression-induced vesiculation at these slow decompression rates. Most of the experiments to date have used decompression rates orders of magnitude higher than those applied in these experiments or they have used extremely high heating rates at atmospheric pressure. Within the context of fragmentation, disequilibrium degassing plays an important role promoting it, which is directly related to the decompression rate applied. The results also indicate that continuous decompression until atmospheric pressure can produce high degrees of magma vesiculation. In these experiments, nanolite crystallisation was observed as a result of vesiculation, most likely

driven by melt dehydration, which is inferred from an increase in nanolite content when the vesiculation degree is higher.

8.1 Implications for volcanic eruptions

The role of nanolites affecting the degassing of magmas during ascent in the conduit has been mostly hypothesised (e.g. Mujin and Nakamura 2014; Di Genova et al., 2017a; Shea, 2017) and their influence on magma properties has started being recognised, producing for instance a viscosity increase (e.g. Di Genova et al., 2017a). This study explored the effect in both the degassing process and influence on viscosity.

Combining the increase in bubble number density and growth rate produced in the presence of nanolites in a degassing magma, it is proposed here that nanolites may play a critical role in enhancing the propensity for eruptions to be explosive. Based on a numerical modelling applied, an ascending nanolite-bearing magma in the conduit can be accelerated towards the surface just by increasing the bubble number density in an extent such as that found in the post-experimental samples. Another effect of the increase in bubble number density, is that it can deepen the fragmentation level of the ascending magma. It is important now to consider the effect on magma viscosity that nanolites produce. Both the increase in the polymerisation degree of the melt and the increase in the crystal load of the magma increase the bulk magma viscosity. High viscosities enhance magma explosivity, thus taken together with the resultant high bubble number density and growth rate, the crystallisation of nanolites in a shallow magma has the potential to shift the behaviour from an eventual effusive eruption style into conditions favourable for an explosive eruption, this pending a triggering mechanism.

Furthermore, the finding of nanolites in the fragmented and vesiculated post-experimental samples subjected to decompression, gives insights into the possible explosivity enhanced by the presence of those crystal. Nanolites were not pre-existing in the melt and their crystallisation is inferred to occur during the decompression-driven melt dehydration. This crystallisation of nanolites may have had an effect increasing magma viscosity promoting fragmentation, especially in combination to the viscosity increase driven by melt dehydration. Nanolites may then play a role enhancing the brittle behaviour of the magma during fast vesiculation by moving the response of the melt closer to its glass transition. The presence of such crystals is important to consider when evaluating the potential explosivity of shallow

rhyolitic magmas, like those found at Laguna del Maule volcanic field in Chile and Krafla volcano in Iceland, for instance.

On the other hand, the coupled effect of microlites and phenocrysts promoting bubble nucleation and coalescence tells about the roles that pre- and syn-eruptive crystalline phases may play in the degassing process of shallow silicic magmas. These roles can have important implications for eruptive style, especially for more crystalline systems. A high abundance of phenocrysts may enhance localised nucleation and coalescence, allowing bubbles to connect each other. Assuming that phenocrysts are mainly crystallised during magma storage in pre-eruptive stages, high amounts of phenocrysts can promote gas percolation and escape deeper in the volcanic conduit. Considering that microlites may also enhance bubble coalescence and magma outgassing at high crystallinities in shallow parts of the conduit (e.g. Lindoo et al., 2017; Colombier et al., 2020), high crystalline silica-rich systems in general may promote the effusion of a lava dome or flow. This has been observed in natural silica-rich magmas, where transitions from initially low-crystallinity explosive products give place to final crystal-rich and highly degassed lava domes.

8.2 Outlook

Here, the effects of nanolites have been investigated mainly for low pressures scenarios and using rhyolitic magma. Further experimental studies investigating the crystallisation conditions of nanolites at higher pressures and using less evolved magma compositions may better constrain the conditions at which nanolites can form. In this study, nanolites have been produced in a magma with low water concentration and during dehydration of a magma with moderately higher water concentration, but the capability of nanolites to form in magmas with high water concentration remains unknown. These further studies may also be useful to understand how nanolites could form during degassing of less viscous magmas and their role promoting basaltic explosivity, for instance. Furthermore, the nanolite crystallisation experiments were conducted in air, which is a known oxidising environment. Conducting such experiments at more reduced conditions in different gas atmospheres would improve our understanding of the role of oxygen fugacity in Fe-Ti oxide nanolites crystallisation and consequent effects on melt structure. Additionally, here it was investigated how Fe-Ti oxide nanolites affect degassing of magma, but how other mineral phases that have been found as nanolites, such as feldspars or pyroxenes (e.g. Mujin and Nakamura, 2014), may influence the degassing dynamics of a magma remains unknown. This could be also addressed by

synthesising different magma compositions at conditions suitable for crystallisation of those phases and conducting vesiculation experiments such as those in this study.

The influence of microlites and phenocrysts is usually studied separately and using synthesised crystal-bearing magmas or magma analogues. The vesiculation experiments conducted in the multiphase vitrophyric rhyolite, allowed to go one step further into the complexity of natural systems. However, the samples used were very low in water concentration and similar experiments using more hydrated samples are necessary to replicate natural systems. Re-hydrating such a material by, for example, long exposure of samples cylinders to P-T conditions of stability of mineral phases and targeted water solubility into sealed capsules, could provide a starting material for conducting vesiculation experiments. These experiments, then, may give better insights into the roles of both types of crystals in the degassing process at conditions closer to natural systems.

These first insight on vesiculation and fragmentation at slow decompression showed that both processes may occur in shallow silica-rich magma. Experiments conducted using samples with different initial water concentrations may help to better establish the conditions at which this magma may fragment or only vesiculate. Also, exploration of fast decompression scenarios and comparison of textures with those generated in this study can help to better understand the processes involved, and also to compare these experiments with past fast-decompression experiments. Textural, chemical, thermal and rheological comparisons of these pre- and post-experimental materials with natural vesicular and non-vesicular ones, such as those extracted through the well from Krafla reservoir in Iceland, may help to better constrain the initial conditions and the propensity for these magmas to generate an eventual eruption. Additionally, in order to map the eruptability of the magma, it is important to know its mobility from storage conditions. Magma infiltration at high temperature through the pre-existing permeable networks of an additional different rock sample may be tested when put together in this same experimental setup. Likewise, re-hydrating another rhyolitic magma with some chemical differences, such as that found in Laguna del Maule volcanic field in Chile, and doing experiments like those in this study using that new material can expand our understanding on the behaviour of silica-rich magmas stored at shallow levels in the crust.

Bibliography

Adams, N.K., Houghton, B.F. and Hildreth, W. 2006a. Abrupt transitions during sustained explosive eruptions: examples from the 1912 eruption of Novarupta, Alaska. Bulletin of Volcanolgy 69, p. 189-206. doi: 10.1007/s00445-006-0067-4

Adams, N.K., Houghton, B.F., Fagents, S.A. and Hildreth, W. 2006b. The transition from explosive to effusive eruptive regime: The example of the 1912 Novarupta eruption, Alaska. GSA Bulletin May/June 2006, v. 118, no. 5/6, p. 620-634. doi: 10.1130/B25768.1

Alfano, F., Bonadonna, C., Volentik, A.C.M., Connor, C.B., Watt, S.F.L., Pyle, D.M. and Connor, L.J. 2011. Tephra stratigraphy and eruptive volume of the May, 2008, Chaitén eruption, Chile. Bull Volcanol 73, p. 613-630. doi: 10.1007/s00445-010-0428-x

Alfano, F., Bonadonna, C. and Gurioli, L. 2012. Insights into eruption dynamics from textural analysis: the case of the May, 2008, Chaitén eruption. Bulletin of Volcanolgy 74, p. 2095-2108. doi: 10.1007/s00445-012-0648-3

Alidibirov, M. and Dingwell, D.B. Magma fragmentation by rapid decompression. Nature 380, 146-148. doi: 10.1038/380146a0

Alidibirov, M. and Dingwell, D.B. 2000. Three fragmentation mechanisms for highly viscous magma under rapid decompression. Journal of Volcanology and Geothermal Research 100, 413-421. doi: 10.1016/S0377-0273(00)00149-9

Almeev, R.R., Bolte, T., Nash, B.P., Holtz, F., Erdmann, M., Cathey, H.E. 2012. High-temperature, low-H2O Silicic Magmas of the Yellowstone Hotspot: an Experimental Study of Rhyolite from the Bruneau–Jarbidge Eruptive Center, Central Snake River Plain, USA. Journal of Petrology 53 (9), 1837-1866. doi: 10.1093/petrology/egs035

Arzilli, F., La Spina, G., Burton, M.R., Polacci, M., Le Gall, N., Hartley, M.E., Di Genova, D., Cai, B., Vo, N.T., Bamber, E.C., Nonni, S., Atwood, R., Llewellin, E.W., Brooker, R.A., Mader, H.M. and Lee, P.D. 2019. Magma fragmentation in highly explosive basaltic eruptions induced by rapid crystallization. Nature Geoscience 12, 1023-1028. doi: 10.1038/s41561-019-0468-6

Ashwell, P.A., Kendrick, J.E., Lavallée, Y., Kennedy, B.M., Hess, K-U., von Aulock, F.W., Wadsworth, F.B., Vasseur, J. and Dingwell, D.B. 2015. Permeability of compacting porous lavas. Journal of Geophysical Research: Solid Earth 120, 1605-1622. doi: 10.1002/2014JB011519

Aspinall, W. and Blong, R. 2015. Volcanic Risk Assessment. *In: The Encyclopedia of Volcanoes (Second Edition*). p. 1215-1231. Doi: 10.1016/B978-0-12-385938-9.00070-5

Bacon, C.R. and Druitt, T.H. 1988. Compositional evolution of the zoned calcalkaline magma chamber of Mount Mazama, Crater Lake, Oregon. Contrib Mineral Petrol 98, p. 224-256. doi: doi.org/10.1007/BF00402114

Barker, S.J., Wilson, C.J.N., Baker, J.A., Millet, M-A., Rotella, M.D., Wright, I.C. and Wysoczanski, R.J. 2013. Geochemistry and Petrogenesis of Silicic Magmas in the Intra-Oceanic Kermadec Arc. Journal of Petrology 54 (2), p. 351-391. doi: 10.1093/petrology/egs071

Barone, G., Mazzoleni, P., Corsaro, R.A., Costagliola, P., Di Benedetto, F., Ciliberto, E., Gimeno, D., Bongiorno, C. and Spinella, C. 2016. Nanoscale surface modification of Mt. Etna volcanic ashes. Geochimica et Cosmochimica Acta 174, p. 70-84. doi: 10.1016/j.gca.2015.11.011

Behrens H., Roux J., Neuville D.R. and Siemann, M. 2006. Quantification of dissolved H2O in silicate glasses using confocal micro-Raman spectroscopy. Chemical Geology 229, 96-112. doi: 10.1016/j.chemgeo.2006.01.014

Bindeman, I.N. 2003. Crystal sizes in evolving silicic magma chambers. Geology 31, 367-370. doi: 10.1130/0091-7613(2003)031<0367:CSIESM>2.0.CO;2

Blower, J. 2001. Factors controlling permeability-porosity relationships in magma. Bulletin of Volcanology 63, 497-504. doi: 10.1007/s004450100172

Blundy, J. and Cashman, K. 2005. Rapid decompression-driven crystallization recorded by melt inclusions from Mount St. Helens volcano. Geology 33 (10), p. 793-796. doi: 10.1130/G21668.1

Bonadonna, C., Cioni, R., Pistolesi, M., Elissondo, M. and Baumann, V. 2015. Sedimentation of long-lasting wind-affected volcanic plumes: the example of the 2011 rhyolitic Cordón Caulle eruption, Chile. Bulletin of Volcanology 77:13. doi: 10.1007/s00445-015-0900-8

Bouhifd, M.A., Richet, P., Besson, P., Roskosz, M. and Ingrin, J. 2004. Redox state, microstructure and viscosity of a partially crystallized basalt melt, Earth and Planetary Science Letters 218, 31.44. doi: 10.1016/s0012-821x(03)00641-1

Burgisser, A., Chevalier, L., Gardner, J.E. and Castro, J.M. 2017. The percolation threshold and permeability evolution of ascending magmas. Earth and Planetary Science Letters 470, 37-47. doi: 10.1016/j.epsl.2017.04.023

Cáceres, F., Castruccio, Á. and Parada, M. A. 2018. Morphology, effusion rates, and petrology of postglacial lavas of Laguna del Maule Volcanic Field, Chilean Andes, and implications for their plumbing system. Geochemistry, Geophysics, Geosystems 19, 4925-4944. doi: 10.1029/2018GC007817

Calder, E.Z., Lavallée, Y., Kendrick, J.E. and Bernstein, M. 2015. Lava Dome Eruptions. *In: The Encyclopedia of Volcanoes (Second Edition)*. p. 343-362. doi: 10.1016/B978-0-12-385938-9.00018-3

Campagnola, S., Romano, C., Mastin, L.G. and Vona, A. 2016. Confort 15 model of conduit dynamics: applications to Pantelleria Green Tuff and Etna 122 BC eruptions. Contributions to Mineralolgy and Petrology 171, 60. doi: 10.1007/s00410-016-1265-5

Carey, S. and Sigurdsson, H. 1985. The May 18, 1980 eruption of Mount St. Helens: 2. Modeling of dynamics of the Plinian phase. Journal of Geophysical Research: Solid Earth 90(B4), 2948-2958. doi: 10.1029/JB090iB04p02948

Carey, R.J., Houghton, B.F. and Thordarson, T. 2009. Abrupt shifts between wet and dry phases of the 1875 eruption of Askja Volcano: Microscopic evidence for macroscopic dynamics. Journal of Volcanology and Geothermal Research 184, p. 256-270. doi: 10.1016/j.jvolgeores.2009.04.003

Carn, S.A., Pallister, J.S., Lara, L., Ewert, J.W., Watt, S., Prata, A.J., Thomas, R.J. and Villarosa, G. 2009. The unexpected awakening of Chaitén volcano, Chile. Eos, Transactions American Geophysical Union 90 (24), 205-206. doi: 10.1029/2009EO240001

Cashman, K.V. 1988. Crystallization of Mount St. Helens 1980–1986 dacite: a quantitative textural approach. Bulletin of Volcanology 50, 194-209. doi: 10.1007/BF01079682

Cashman, K.V. and Sparks, R.S.J. 2013. How volcanoes work: A 25 year perspective. GSA Bulletin 125(5-6), 664-690. doi: 10.1130/B30720.1

Cashman, K.V., Soule, S., Mackey, B., Deligne, N., Deardorff, N. and Dietterich, H., 2013. How lava flows: new insights from applications of lidar technologies to lava flow studies. Geosphere 9, 1664-1680. doi: 10.1130/GES00706.1

Cashman, K.V. and Scheu, B. 2015. Magmatic fragmentation. *In: The Encyclopedia of Volcanoes (Second Edition)*. p. 459-471. doi: 10.1016/B978-0-12-385938-9.00025-0

Cassidy, M., Manga, M., Cashman, K. and Bachmann, O. 2018. Controls on explosive-effusive volcanic eruption styles. Nature Communications 9:2839. doi: 10.1038/s41467-018-05293-3

Castro, J.M. and Dingwell, D.B. 2009. Rapid ascent of rhyolitic magma at Chaitén volcano, Chile. Nature 461, p. 780-783. doi: 10.1038/nature08458

Castro, J.M., Schipper, C.I., Mueller, S.P., Militzer, A.S., Amigo, A., Parejas, C.S. and Jacob, D. 2013. Storage and eruption of near-liquidus rhyolite magma at Cordón Caulle, Chile. Bulletin of Volcanology 75: 702. doi: 10.1007/s00445-013-0702-9

Chang, W.L., Smith, R.B., Farrell, J. and Puskas, C.M. 2010. An extraordinary episode of Yellowstone caldera uplift, 2004–2010, from GPS and InSAR observations. Geophysical Research Letters 37, L23302. doi: 10.1029/2010GL045451

Chevrel, M.O., Cimarelli, C., deBiasi, L., Hanson, J.B., Lavallée, Y., Arzilli, F. and Dingwell, D.B. 2015. Viscosity measurements of crystallizing andesite from Tungurahua volcano (Ecuador). Geochem. Geophys. Geosyst. 16, 870-889. doi: 10.1002/2014GC005661

Cimarelli, C., Costa, A., Mueller, S. and Mader, H.M. 2011. Rheology of magmas with bimodal crystal size and shape distributions: Insights from analog experiments. Geochem. Geophys. Geosyst., 12, Q07024. doi: 10.1029/2011GC003606

Cioni, R., Civetta, L., Marianelli, P., Metrich, N., Santacroce, R. and Sbrana, A. 1995. Compositional Layering and Syn-eruptive Mixing of a Periodically Refilled Shallow Magma Chamber: the AD 79 Plinian Eruption of Vesuvius. Journal of Petrology 36 (3), p. 739-776. doi: 10.1093/petrology/36.3.739

Cioni, R., Bertagnini, A., Andronico, D., Cole, P.D. and Mundula, F. 2011. The 512 AD eruption of Vesuvius: complex dynamics of a small scale subplinian event. Bulletin of Volcanolgy 73, p. 789-810. doi: 10.1007/s00445-011-0454-3

Cluzel, N., Laporte, D., Provost, A. and Kannewischer, I. 2008. Kinetics of heterogeneous bubble nucleation in rhyolitic melts: implications for the number density of bubbles in volcanic conduits and for pumice textures. Contrib Mineral Petrol 156, p. 745-763. doi: 10.1007/s00410-008-0313-1

Cochain, B., Neuville, D.R., Henderson, G.S., McCammon, C.A., Pinet, O. and Richet, P. 2012. Effects of the iron content and redox state on the structure of sodium borosilicate glasses: a Raman, Mössbauer and boron k-edge xanes spectroscopy study, J. Am. Ceram. Soc. 95, 962-971. Doi: 10.1111/j.1551-2916.2011.05020.x

Colombier, M., Wadsworth, F.B., Gurioli, L., Scheu, B., Kueppers, U., Di Muro, A. and Dingwell, D.B. 2017a. The evolution of pore connectivity in volcanic rocks. Earth and Planetary Science Letters 462, p. 99-109. doi: 10.1016/j.epsl.2017.01.011

Colombier, M., Gurioli, L., Druitt, T.H., Shea, T., Boivin, P., Miallier, D. and Cluzel, N. 2017b. Textural evolution of magma during the 9.4-ka trachytic explosive eruption at Kilian Volcano, Chaîne des Puys, France. Bull Volcanol 79:17. doi: 10.1007/s00445-017-1099-7

Colombier, M., Wadsworth, F.B., Scheu, B., Vasseur, J., Dobson, K.J., Cáceres, F., Allabar, A., Marone, F., Schlepütz, C. and Dingwell, D.B. 2020. In situ observation of the percolation threshold in multiphase magma. Bulletin of Volcanology 82:32. doi: 10.1007/s00445-020-1370-1

Coombs, M.L. and Gardner, J.E. 2001. Shallow-storage conditions for the rhyolite of the 1912 eruption at Novarupta, Alaska. Geology 29 (9), p. 775-778. doi: 10.1130/0091-7613(2001)029<0775:SSCFTR>2.0.CO;2

Cordell, D., Unsworth, M.J. and Diaz, D. 2018. Imaging the Laguna del Maule volcanic field, central Chile, using magnetotellurics: Evidence for crustal melt regions laterally-offset from surface vents and Holocene lava flows. Earth and Planetary Science Letters 488, 168-180. doi: 10.1016/j.epsl.2018.01.007

Costa A. 2005. Viscosity of high crystal content melts: dependence on solid fraction. Geophysical Research Letters 32, L22308. doi:10.1029/2005GL024303

D'Oriano, C., Bertagnini, A., Cioni, R. and Pompilio, M. 2014. Identifying recycled ash in basaltic eruptions. Scientific Reports 4, 5851. doi: 10.1038/srep05851

deGraffenried, R.L., Larsen, J.F., Graham, N.A. and Cashman, K.V. 2019. The influence of phenocrysts on degassing in crystal ‐ bearing magmas with rhyolitic groundmass melts. Geophysical Research Letters 46, 5127-5136. doi: 10.1029/2018GL081822

Degruyter, W., Bachmann, O., Burgisser, A. and Manga, M. 2012. The effects of outgassing on the transition between effusive and explosive silicic eruptions. Earth and Planetary Science Letters 349-350, p. 161-170. doi: 10.1016/j.epsl.2012.06.056

Dalou, C., Le Losq, C., Mysen, B.O. and Cody, G.D. 2015. Solubility and solution mechanisms of chlorine and fluorine in aluminosilicate melts at high pressure and high temperature. American Mineralogist 100, 2272-2283. doi: 10.2138/am-2015-5201

Di Genova, D., Kolzenburg, S., Wiesmaier, S., Dallanave, E., Neuville, D. R., Hess, K-U. and Dingwell, D. B. 2017a. A compositional tipping point governing the mobilization and eruption style of rhyolitic magma. Nature 552, p. 235-238. doi:10.1038/nature24488

Di Genova, D., Vasseur, J., Hess, K-U., Neuville, D.R. and Dingwell, D.B. 2017b. Effect of oxygen fugacity on the glass transition, viscosity and structure of silica- and iron-rich magmatic melts. Journal of Non-Crystalline Solids 470, 78-85. doi: /10.1016/j.jnoncrysol.2017.05.013

Di Genova, D., Sicola, S., Romano, C., Vona, A., Fanara, S. and Spina, L. 2017c. Effect of iron and nanolites on Raman spectra of volcanic glasses: A reassessment of existing strategies to estimate the water content. Chemical Geology 475, 76-86. doi: 10.1016/j.chemgeo.2017.10.035

Di Genova, D., Caracciolo, A. and Kolzenburg, S. 2018. Measuring the degree of "nanotilization" of volcanic glasses: Understanding syn-eruptive processes recorded in melt inclusions. Lithos 318-319, 209-218. doi: 10.1016/j.lithos.2018.08.011

Di Muro, A., Villemant, B., Montagnac, G., Scaillet, B. and Reynard, B. 2006a. Quantification of water content and speciation in natural silicic glasses (phonolite, dacite, rhyolite) by confocal microRaman spectrometry. Geochimica et Cosmochimica Acta 70, p. 2868-2884. doi: 10.1016/j.gca.2006.02.016

Di Muro A., Giordano D., Villemant B., Montagnac G., Scaillet B. and Romano C. 2006b. Influence of composition and thermal history of volcanic glasses on water content as determined by micro-Raman spectrometry. Appl. Geochem. 70, 802-812. 10.1016/j.apgeochem.2006.02.009

Di Muro, A., Métrich, N., Mercier, M., Giordano, D., Massare, D. and Montagnac, G. 2009. Micro-Raman determination of iron redox state in dry natural glasses: application to peralkaline rhyolites and basalts. Chemical Geology 259, 78-88. doi: 10.1016/j.chemgeo.2008.08.013

Diller, K., Clarke, A.B., Voight, B. and Neri, A. 2006. Mechanisms of conduit plug formation: Implications for vulcanian explosions. Geophysical Research Letters 33, L20302. doi: 10.1029/2006GL027391

Dingwell, D.B. and Virgo, D. 1987. The effect of oxidation state on the viscosity of melts in the system Na2O-FeO-Fe2O3-SiO2. Geochimica et Cosmochimica Acta 51, 195-205.

Dingwell, D.B. and Webb, S., 1989. Structural Relaxation in Silicate Melts and Non-Newtonian Melt Rheology in Geologic Processes. Physics and Chemistry of Minerals 16, 508-516. doi: 10.1007/BF00197020

Dingwell, D.B. 1996. Volcanic dilemma: flow or blow? Science 273, 1054–1055. doi: 10.1126/science.273.5278.1054

Eichelberger, J.C. and Westrich, H.R. 1981. Magmatic volatiles in explosive rhyolitic eruptions. Geophysical Research Letters 8(7), 757-760. doi: 10.1029/GL008i007p00757

Eichelberger, J.C., Carrigan, C.R., Westrich, H.R. and Price, R.H. 1986. Non-explosive silicic volcanism. Nature 323, 598-602. doi: 10.1038/323598a0

Eichelberger, JC. 1995. Silicic volcanism: Ascent of Viscous Magmas from Crustal Reservoirs. Annu. Rev. Earth Planet. Sci. 23, 41-63. doi: 10.1146/annurev.ea.23.050195.000353

Eichelberger, J.C., Ingolfsson, H.P., Carrigan, C., Lavallee, Y., Tester, J.W. and Markusson, S.H. 2018. Krafla Magma Testbed: Understanding and Using the Magma-Hydrothermal Connection. Geotherm. Resour. Counc. Trans. 42.

Eichelberger, J. 2019. Planning an International Magma Observatory. EOS, 100. doi: 10.1029/2019EO125255

Einarsson, P., 1978. S-wave shadows in the Krafla caldera in NE-Iceland, evidence for a magma chamber in the crust. Bulletin of Volcanology 41, 187-195. doi: 10.1007/BF02597222.

Elders, W.A., Friðleifsson, G.Ó., Zierenberg, R.A., Pope, E.C., Mortensen, A.K., Gudmundsson, A., Lowenstern, J.B., Marks, N.E., Owens, L., Bird, D.K., Reed, M., Olsen, N.J. and Schiffman, P.A. 2011. Origin of a rhyolite that intruded a geothermal well while drilling in a basaltic volcano, at Krafla, Iceland. Geology 39, 231-234. doi: 10.1130/G31393.1

Elders, W.A., Friðleifsson, G.Ó. and Albertsson, A. 2014. Drilling into magma and the implications of the Iceland Deep Drilling Project (IDDP) for high-temperature geothermal systems worldwide. Geothermics 49, 111-118. doi: 10.1016/j.geothermics.2013.05.001

Farquharson, J.I., Wadsworth, F.B., Heap, M.J. and Baud, P. 2017. Time-dependent permeability evolution in compacting volcanic fracture systems and implications for gas overpressure. Journal of Volcanology and Geothermal Research 339, p. 81-97. doi: 10.1016/j.jvolgeores.2017.04.025

Feigl, K.L., Le Mével, H., Ali, S.T., Córdova, L., Andersen, N.L., DeMets, C. and Singer, B.S. 2014. Rapid uplift in Laguna del Maule volcanic field of the Andean Southern Volcanic Zone (Chile) 2007-2012. Geophysical Journal International 196 (2), 885-901. doi: 10.1093/gji/ggt438

Fierstein, J. and Hildreth, W. 1992. The plinian eruptions of 1912 at Novarupta, Katmai National Park, Alaska. Bull Volcanol 54, p.646-684. doi: 10.1007/BF00430778

Forte, P. and Castro, J. M. 2019. H2O-content and temperature limit the explosive potential of rhyolite magma during Plinian eruptions. Earth and Planetary Science Letters 506, p. 157-167. doi: 10.1016/j.epsl.2018.10.041

Fournier, T.J., Pritchard, M.E. and Riddick, S. N. 2010. Duration, magnitude, and frequency of subaerial volcano deformation events: New results from Latin America using InSAR and global synthesis. Geochemistry, Geophysics and Geosystems 11 (1), Q01003, doi: 10.1029/2009GC002558.

Fowler, A.C., Scheu, B., Lee, W.T. and McGuinness, M.J. 2010. A theoretical model of the explosive fragmentation of vesicular magma. Proc. R. Soc. A 466, 731-752. doi: 10.1098/rspa.2009.0382

Frey, F.A., Gerlach, D.C., Hickey, R.L., López-Escobar, L. and Munizaga, F. 1984. Petrogenesis of the Laguna del Maule volcanic complex, Chile (36°S). Contributions to Mineralogy and Petrology 88, 133-149. doi: 10.1007/BF00371418

Friðleifsson, G.O. and Elders, W.A. 2005. The Iceland deep drilling project: a search for deep unconventional geothermal resources: Geothermics 34, 269-285. doi: 10.1016/j.geothermics.2004.11.004

Friðleifsson, G.O., Elders, W.A. and Bignall, G. 2013. A plan for a 5 km-deep borehole at Reykjanes, Iceland, into the root zone of a black smoker on land. Sci. Dril., 16, 73-79. doi: 10.5194/sd-16-73-2013

Fukumi, K., Ogawa, K. and Hayakawa, J. 1992. Intensities of Raman bands in borate glasses. J. Non-Cryst. Solids 151, 217-221. doi: 10.1016/0022-3093(92)90032-F

Furukawa, T., Fox, K.E. and White, W.B. 1981. Raman spectroscopic investigation of the structure of silicate glasses. III. Raman intensities and structural units in sodium silicate glasses. J. Chem. Phys. 75, 3226. doi: 10.1063/1.442472

Gardner, J.E., Hilton, M., Carroll, M.R. 1999. Experimental constraints on degassing of magma: isothermal bubble growth during continuous decompression from high pressure. Earth and Planetary Science Letters 168, 201-218. doi: 10.1016/S0012-821X(99)00051-5

Gardner, J. E. and Denis, M-H. 2004. Heterogeneous bubble nucleation on Fe-Ti oxide crystals in high-silica rhyolitic melts. Geochimica et Cosmochimica Acta 68 (7), p. 3587-3597. doi: 10.1016/j.gca.2004.02.021

Gerst, A., Hort, M., Aster, R.C., Johnson, J.B. and Kyle, P.R. 2013. The first second of volcanic eruptions from the Erebus volcano lava lake, Antarctica—Energies, pressures, seismology, and infrasound. Journal of Geophysical Research: Solid Earth 118, 3318-3340. doi: 10.1002/jgrb.50234

Ghiorso, M.S. and Gualda, G.A.R. 2015. An H2O-CO2 mixed fluid saturation model compatible with rhyolite-MELTS. Contributions to Mineralogy and Petrology 169:53. doi: 10.1007/s00410-015-1141-8

Giachetti, T., Druitt, T.H., Burgisser, A., Arbaret, L. and Galven, C. 2010. Bubble nucleation, growth and coalescence during the 1997 Vulcanian explosions of Soufrière Hills

Volcano, Montserrat. Journal of Volcanology and Geothermal Research 193, p. 215-231. doi: 10.1016/j.jvolgeores.2010.04.001

Giachetti, T., Gonnermann, H. M., Gardner, J. E., Burgisser, A., Hajimirza, S., Earley, T. C., Truong, N. and Toledo, P. 2019. Bubble coalescence and percolation threshold in expanding rhyolitic magma. Geochemistry, Geophysics, Geosystems 20, p. 1054-1074. doi: 10.1029/2018GC008006

Giordano, D. and Dingwell, D.B. 2003. Non-Arrhenian multicomponent melt viscosity: a model. Earth and Planetary Science Letters 208, 337-349. doi: 10.1016/S0012-821X(03)00042-6

Giordano, D. and Russell, J.K. 2018. Towards a structural model for the viscosity of geological melts. Earth and Planetary Science Letters 501, 202-212. doi: 10.1016/j.epsl.2018.08.031

Giordano, D., González-García, D., Russell, J.K., Raneri, S., Bersani, D., Fornasini, L., Di Genova, D., Ferrando, S., Kaliwoda, M., Lottici, P.P., Smit, M., Dingwell, D.B. 2019. A calibrated database of Raman spectra for natural silicate glasses: Implications for modelling melt physical properties. Journal of Raman Spectroscopy 1– 17. doi: 10.1002/jrs.5675

Gualda, G.A.R., Ghiorso, M.S., Lemons, R.V. and Carley T.L. 2012. Rhyolite-MELTS: A modified calibration of MELTS optimized for silica-rich, fluid-bearing magmatic systems. Journal of Petrology 53, 875-890. doi: 10.1093/petrology/egr080

Gonnermann, H.M. and Manga, M. 2007. The Fluid Mechanics Inside a Volcano. Annu. Rev. Fluid Mech. 39:321-356. doi: 10.1146/annurev.fluid.39.050905.110207

Gonnermann, H.M. and Manga, M., 2012. Dynamics of magma ascent in the volcanic conduit. In: Modeling Volcanic Processes: The Physics and Mathematics of Volcanism. Eds. Sarah A. Fagents, Tracy K. P. Gregg, and Rosaly M. C. Cambridge University Press, pp.55-84. doi: 10.1017/CBO9781139021562.004

Gonnermann, H.M. and Gardner, J.E. 2013. Homogeneous bubble nucleation in rhyolitic melt: experiments and nonclassical theory. Geochemistry, Geophysics, Geosystems 14, 1-16. doi: 10.1002/ggge.20281

Gonnermann, H.M. Magma Fragmentation. 2015. Annu. Rev. Earth Planet. Sci. 43, 431-458. doi: 10.1146/annurev-earth-060614-105206

Gonnermann, H.M., Giachetti, T., Fliedner, C., Nguyen, C.T., Houghton, B.F., Crozier, J.A. and Carey, R.J. 2017. Permeability during magma expansion and compaction. Journal of Geophysical Research: Solid Earth 122, 9825-9848. doi: 10.1002/2017JB014783

Gualda, G.A.R. and Rivers, M. 2006. Quantitative 3D petrography using X-ray tomography: application to Bishop Tuff pumice clasts. Journal of Volcanology and Geothermal Research 154, 48-62. doi: 10.1016/j.jvolgeores.2005.09.019

Gurioli, L., Houghton, B.F., Cashman, K.V. and Cioni, R. 2005. Complex changes in eruption dynamics during the 79 AD eruption of Vesuvius. Bull Volcanol 67, p. 144-159. doi: 10.1007/s00445-004-0368-4

Harford, C.L., Sparks, R.S.J. and Fallick, A.E. 2003. Degassing at the Soufriere Hills Volcano, Montserrat, Recorded in Matrix Glass Compositions. Journal of Petrology 44 (8), p. 1503-1523. doi: 10.1093/petrology/44.8.1503

Hamada, M., Laporte, D., Cluzel, N., Koga, K.T. and Kawamoto, T. 2010. Simulating bubble number density of rhyolitic pumices from Plinian eruptions: constraints from fast decompression experiments. Bull Volcanol 72, p. 735-746. doi: 10.1007/s00445-010-0353-z

Harris, A. J., Flynn, L. P., Matıas, O., and Rose, W. I. 2002. The thermal stealth flows of Santiaguito dome, Guatemala: Implications for the cooling and emplacement of dacitic block-lava flows. GSA Bulletin, 114 (5), 533-546.

Heap, M.J., Tuffen, H., Wadsworth, F.B., Reuschlé, T., Castro, J.M. and Schipper, C.I. 2019. The permeability evolution of tuffisites and implications for outgassing through dense rhyolitic magma. Journal of Geophysical Research: Solid Earth 124, 8281-8299. doi: 10.1029/2018JB017035

Hess, K-U. and Dingwell, D.B. 1996. Viscosities of hydrous leucogranitic melts: A non-Arrhenian model. American Mineralogist 81, p. 1297-1300. doi: 10.2138/am-1996-9-1031

Hildreth, W., Godoy, E., Fierstein, J. and Singer, B. 2010. Laguna del Maule Volcanic Field: Eruptive history of a Quaternary basalt-to-rhyolite distributed volcanic field on the Andean rangecrest in central Chile. Servicio Nacional de Geología y Minería, Boletín 63, 145p. Santiago, Chile.

Houghton, B.F. and Gonnermann, H.M. 2008. Basaltic explosive volcanism: constraints from deposits and models. Geochemistry 68, 117-140. doi: 10.1016/j.chemer.2008.04.002

Houghton, B.F., Carey, R.J., Cashman, K.V., Wilson, C.J.N., Hobden, B.J. and Hammer, J.E. 2010. Diverse patterns of ascent, degassing, and eruption of rhyolite magma during the 1.8 ka Taupo eruption, New Zealand: Evidence from clast vesicularity. Journal of Volcanology and Geothermal Research 195, p. 31-47. doi: 10.1016/j.jvolgeores.2010.06.002

Hurwitz, S. and Navon, O. 1994. Bubble nucleation in rhyolitic melts: Experiments at high pressure, temperature, and water content. Earth and Planetary Science Letters 122, p. 267-280. doi: 10.1016/0012-821X(94)90001-9

Iezzi, G., Mollo, S., Ventura, G., Cavallo, A. and Romano, C. 2008. Experimental solidification of anhydrous latitic and trachytic melts at different cooling rates: The role of nucleation kinetics. Chemical Geology 253, 91-101. doi: 10.1016/j.chemgeo.2008.04.008

James, M.R., Lane, S.J. and Houghton, B.F. 2013. Unsteady explosive activity: Strombolian eruptions. In: Modeling Volcanic Processes: The Physics and Mathematics of Volcanism. Eds. Sarah A. Fagents, Tracy K. P. Gregg, and Rosaly M. C. Cambridge University Press, pp.107-129.

Jaupart, C. and Allègre, C.J. 1991. Gas content, eruption rate and instabilities of eruption regime in silicic volcanoes. Earth and Planetary Science Letters 102, 413-429. doi: 10.1016/0012-821X(91)90032-D

Jónasson, K., 1994. Rhyolite volcanism in the Krafla central volcano, northeast Iceland. Bulletin of Volcanology 56, 516-528. doi: 10.1007/BF00302832

Jónasson, K., 2007. Silicic volcanism in Iceland: Composition and distribution within the active volcanic zones. Journal of Geodynamics 43, 101-117. doi: 10.1016/j.jog.2006.09.004

Kendrick, J.E., Lavallée, Y., Varley, N.R., Wadsworth, F.B., Lamb, O.D. and Vasseur, J. 2016. Blowing off steam: tuffisite formation as a regulator for lava dome eruptions. Frontiers in Earth Sciences 4, p. 1-15. doi: 10.3389/feart.2016.00041

Kennedy, B.M., Jellinek, A.M., Russell, J.K., Nichols, A.R.L. and Vigouroux, N. 2010. Time- and temperature-dependent conduit wall porosity: a key control on degassing and explosivity at Tarawera volcano, New Zealand. Earth and Planetary Science Letters 299 (1), 126-137. doi: 10.1016/j.epsl.2010.08.028

Kennedy, B.M., Wadsworth, F.B., Vasseur, J., Schipper, C.I., Jellinek, A.M., von Aulock, F.W., Hess, K., Russell, J.K., Lavallée, Y., Nichols, A.R.L. and Dingwell, D.B. 2016. Surface tension driven processes densify and retain permeability in magma and lava. Earth and Planetary Science Letters 433, p. 116-124. doi: 10.1016/j.epsl.2015.10.031

Kirkpatrick, R.J. 1983. Theory of nucleation in silicate melts. American Mineralogists 68, 66-77.

Klug, C. and Cashman, K.V. 1994. Vesiculation of May 18, 1980, Mount St. Helens magma. Geology 22, p. 468-472. doi: 10.1130/0091-7613(1994)022<0468:VOMMSH>2.3.CO;2

Klug, C., Cashman, K.V. and Bacon, C.R. 2002. Structure and physical characteristics of pumice from the climactic eruption of Mount Mazama (Crater Lake), Oregon. Bull Volcanol 64, p. 486-501. doi: 10.1007/s00445-002-0230-5

Kolzenburg, S., Giordano, D., Thordarson, T., Höskuldsson, A. and Dingwell, D.B., 2017. The rheological evolution of the 2014/2015 eruption at Holuhraun, central Ice-land. Bulletin of Volcanology 79: 45. doi: 10.1007/s00445-017-1128-6

Kolzenburg, S., Di Genova. D., Giordano, D., Hess, K-U. and Dingwell, D.B. 2018. The effect of oxygen fugacity on the rheological evolution of crystallizing basaltic melts. Earth and Planetary Science Letters 487, 21-32. doi: 10.1016/j.epsl.2018.01.023

Kueppers, U., Scheu, B., Spieler, O. and Dingwell, D.B. 2006. Fragmentation efficiency of explosive volcanic eruptions: a study of experimentally generated pyroclasts. Journal of Volcanology and Geothermal Research 153(1-2), 125-135. doi: 10.1016/j.jvolgeores.2005.08.006

Kushnir, A.R.L., Martel, C., Champallier, R. and Arbaret, L. 2017. In situ confirmation of permeability development in shearing bubble-bearing melts and implications for volcanic outgassing. Earth and Planetary Science Letters 458, p. 315-326. doi: 10.1016/j.epsl.2016.10.053

Lanzo, G., Landi, P. and Rotolo, S.G. 2013. Volatiles in pantellerite magmas: A case study of the Green Tuff Plinian eruption (Island of Pantelleria, Italy). Journal of Volcanology and Geothermal Research 262, p. 153-163. doi: 10.1016/j.jvolgeores.2013.06.011

Larsen, J. F. 2008. Heterogeneous bubble nucleation and disequilibrium H2O exsolution in Vesuvius K-phonolite melts. Journal of Volcanology and Geothermal Research 175, p. 278-288. doi: 10.1016/j.jvolgeores.2008.03.015

Lavallée, Y., Hess, K.U., Cordonnier, B. and Dingwell, D.B. 2007. Non-newtonian rheological law for highly crystalline dome lavas. Geology 35 (9), 843-846. doi: 10.1130/G23594A.1

Lavallée, Y., Dingwell, D.B., Johnson, J.B., Cimarelli, C., Hornby, A.J., Kendrick, J.E., von Aulock, F.W., Kennedy, B.M., Andrews, B.J., Wadsworth, F.B., Rhodes, E. and Chinga, G. 2015. Thermal vesiculation during volcanic eruptions. Nature 528, 544-547. doi: 10.1038/nature16153

Le Losq, C., Neuville, D.R., Moretti, R. and Roux, J. 2012. Determination of water content in silicate glasses using Raman spectrometry: implications for the study of explosive volcanism. American Mineralogist 97, 779-790. doi: 10.2138/am.2012.3831

Le Losq, C. and Neuville, D.R. 2017. Molecular structure, configurational entropy and viscosity of silicate melts: Link through the Adam and Gibbs theory of viscous flow. Journal of Non-Crystalline Solids 463, 175-188. doi: 10.1016/j.jnoncrysol.2017.02.010

Le Mével, H., Gregg, P.M. and Feigl, K.L. 2016. Magma injection into a long-lived reservoir to explain geodetically measured uplift: Application to the 2007-2014 unrest episode at Laguna del Maule volcanic field, Chile. Journal of Geophysical Research: Solid Earth 121, 6092-6108. doi: 10.1002/2016JB013066

Lensky, N.G., Lyakhovsky, V. and Navon, O. 2001. Radial variations of melt viscosity around growing bubbles and gas overpressure in vesiculating magmas. Earth and Planetary Science Letters 186, p. 1-6. doi: 10.1016/S0012-821X(01)00227-8

Liebske, C., Beherens., H., Holtz, F. and Lange, R. A. 2003. The influence of pressure and composition on the viscosity of andesitic melts. Geochimica et Cosmochimica Acta 67 (3), p. 473- 485. doi: 10.1016/S0016-7037(02)01139-0

Lindoo, A., Larsen, J.F., Cashman, K.V., Dunn, A.L. and Neill, O.K. 2016. An experimental study of permeability development as a function of crystal-free melt viscosity. Earth and Planetary Science Letters 435, p. 45-54. doi: 10.1016/j.epsl.2015.11.035

Lindoo, A., Larsen, J.F., Cashman, K.V. and Oppenheimer, J. 2017. Crystal controls on permeability development and degassing in basaltic andesite magma. Geology 45 (9), p. 831-834. doi: 10.1130/G39157.1

Liu, Y., Zhang, Y. and Behrens, H. 2005. Solubility of H2O in rhyolitic melts at low pressures and a new empirical model for mixed H2O–CO2 solubility in rhyolitic melts. Journal of Volcanology and Geothermal Research 143, p. 219-235. doi: 10.1016/j.jvolgeores.2004.09.019

Long, D.A. 1977. Raman Spectroscopy. New York, McGraw-Hill, Vol. 2. xiii 276, 16 p.

Mangan, M.T. and Sisson, T.W. 2000. Delayed, disequilibrium degassing in rhyolite magma: decompression experiments and implications for explosive volcanism. Earth and Planetary Science Letters 183, 441-455. doi: 10.1016/S0012-821X(00)00299-5

Mangan, M., Sisson, T. and Hankins, W.B. 2004. Decompression experiments identify kinetic controls on explosive silicic eruptions. Geophysical Research Letters 31, L08605. doi:10.1029/2004GL019509

Martel, C., Dingwell, D.B., Spieler, O., Pichavant, M. and Wilke, M. 2000. Fragmentation of foamed silicic melts: an experimental study. Earth and Planetary Science Letters 178, 47-58. doi: 10.1016/S0012-821X(00)00062-5

Martel, C., Dingwell, D.B., Spieler, O., Pichavant, M. and Wilke, M. 2001. Experimental fragmentation of crystal- and vesicle-bearing silicic melts. Bulletin of Volcanology 63, 398-405. doi: 10.1007/s004450100157

Massol, H. and Jaupart, C. 1999. The generation of gas overpressure in volcanic eruptions. Earth and Planetary Science Letters 166 (1-2), 57- 70. doi: 10.1016/S0012-821X(98)00277-5

Mastin, L. G. 2002. Insights into volcanic conduit flow from an open-source numerical model. Geochemistry, Geophysics, Geosystems 3 (7). doi: 10.1029/2001GC000192

McBirney, A.R. and Murase, T. 1970. Factors governing the formation of pyroclastic rocks. Bulletin Volcanologique 34 (2), p. 372-384. doi: 10.1007/BF02596762

McMillan, P.F. 1984. A Raman spectroscopic study of glasses in the system CaO-MgO-SiO2, American Mineralogist 69, 645-659.

McMillan, P.F., Poe, B.T., Gillet, P.H. and Reynard, B. 1994. A study of SiO2 glass and supercooled liquid to 1950 K via high-temperature Raman spectroscopy. Geochim. Cosmochim. Acta 58 (17), 3653-3664. doi: 10.1016/0016-7037(94)90156-2

Mercier, M., Di Muro, A., Giordano, D., Métrich, N., Lesne, P., Pichavant, M., Scaillet, B., Clocchiatti, R. and Montagnac, G. 2009. Influence of glass polymerisation and oxidation on micro-Raman water analysis in alumino-silicate glasses. Geochim. Cosmochim. Acta 73, 197-217. doi: 10.1016/j.gca.2008.09.030

Miller, C.A., Williams-Jones, G., Fournier, D. and Witter, J. 2017. 3-D gravity inversion and thermodynamic modelling reveal properties of shallow silicic magma reservoir beneath Laguna del Maule, Chile. Earth and Planetary Science Letters 459, 14-27. doi: 10.1016/j.epsl.2016.11.007

Mollo, S., Putirka, K., Iezzi, G. and Scarlato, P. 2009. The control of cooling rate on titanomagnetite composition: implications for a geospeedometry model applicable to alkaline rocks from Mt. Etna volcano. Contrib Mineral Petrol 165, 457-475. doi: 10.1007/s00410-012-0817-6

Mortensen, A.K., Grönvold, K., Gudmundsson, A., Steingrímsson, B.S., Egilson, Þ. 2010 Quenched silicic glass from well K-39 in Krafla, North-Eastern Iceland. In:

Proceedings of the world geothermal congress 2010, Bali, Indonesia, 25-29 April 2010, 1284, pp. 1-6.

Mourtada-Bonnefoi, C.C. and Laporte, D. 1999. Experimental study of homogeneous bubble nucleation in rhyolitic magmas. Geophys. Res. Lett. 26, 3505–3508.

Mourtada-Bonnefoi, C.C. and Laporte, D. 2002. Homogeneous bubble nucleation in rhyolitic magmas: an experimental study of the effect of H2O and CO2. Journal of Geophysical Research: Solid Earth 107: B4. doi: 10.1029/2001JB00290.

Mourtada-Bonnefoi, C.C. and Laporte, D. 2004. Kinetics of bubble nucleation in a rhyolitic melt: an experimental study of the effect of ascent rate. Earth and Planetary Science Letters 218, 521-537. doi: 10.1016/S0012-821X(03)00684-8

Mueller, S., Scheu, B., Spieler, O. and Dingwell, D.B. 2008. Permeability control on magma fragmentation. Geology 36, p.399-402. doi: 10.1130/G24605A.1

Mujin, M. and Nakamura, M. 2014. A nanolite record of eruption style transition. Geology 42 (7), p. 611-614. doi: 10.1130/G35553.1

Mujin, M., Nakamura, M. and Miyake, A. 2017. Eruption style and crystal size distributions: Crystallization of groundmass nanolites in the 2011 Shinmoedake eruption. American Mineralogist 102, p. 2367-2380. doi: 10.2138/am-2017-6052CCBYNCND

Munizaga, F. 1978. Geología del complejo volcánico Laguna del Maule. (BSc dissertation) (non-published). Universidad de Chile, Departamento de Geología. Santiago, Chile, 157 p.

Mysen, B.O., Virgo, D. and Scarfe, C.M. 1980. Relations between anionic structure and viscosity of silicate melts - a Raman spectroscopic study. American Mineralogist 65, 690-710.

Mysen, B.O., Virgo, D. and Kushiro, I. 1981. The structural role of aluminum in silicate melts – a Raman spectroscopic study at 1 atmosphere. American Mineralogist 65, 690-710.

Nakamura, K. 2006. Textures of plagioclase microlite and vesicle within volcanic products of the 1914-1915 eruption of Sakurajima Volcano, Kyushu, Japan. Journal of Mineralogical and Petrological Sciences 101, p. 178-198. doi: 10.2465/jmps.101.178

Neuville, D.R., de Ligny, D. and Henderson, G.S. 2014. Advances in Raman Spectroscopy Applied to Earth and Material Sciences. Reviews in Mineralogy and Geochemistry 78, 509-541. doi: 10.2138/rmg.2013.78.13

Newman, A.V., Stiros, S., Feng, L.J., Psimoulis, P., Moschas, F., Saltogianni, V., Jiang, Y., Papazchos, C., Panagiotopoulos, D., Karagianni, E. and Vamcakaris, D. 2012. Recent geodetic unrest at Santorini Caldera, Greece. Geophysical Research Letters 39, L06309. doi: 10.1029/2012GL051286

Newville, M., Stensitzki, T., Allen, D.B., and Ingargiola, A. 2014. LMFIT: Non-Linear Least-Square Minimization and Curve-Fitting for Python. Zenodo. doi: 10.5281/zenodo.11813

Okumura, S., Nakamura, M., Takeuchi, S., Tsuchiyama, A., Nakano, T. and Uesugi, K. 2009. Magma deformation may induce non-explosive volcanism via degassing through bubble networks. Earth and Planetary Science Letters 281 (3–4), p. 267-274. doi: 10.1016/j.epsl.2009.02.036

Oppenheimer, J., Rust, A. C., Cashman, K. V. and Sandnes B. 2015. Gas migration regimes and outgassing in particle-rich suspensions. Front. Phys. 3:60. doi: 10.3389/fphy.2015.00060

Pallister, J.S., Diefenbach, A., Burton, W., Muñoz, J., Griswold, J., Lara, L. and Valenzuela, C.E. 2013. The Chaitén rhyolite lava dome: Eruption sequence, lava dome volumes, rapid effusion rates and source of the rhyolite magma. Andean Geology 40 (2), 277-294. doi: 10.5027/andgeoV40n2-a06

Papale, P. 1999. Strain-induced magma fragmentation in explosive eruptions. Nature 397,425-428. doi: 10.1038/17109

Pleše, P., Higgins, M. D., Mancini, L., Lanzafame, G., Brun, F., Fife, J. L., Casselman, J. and Baker, D. R. 2018. Dynamic observations of vesiculation reveal the role of silicate crystals in bubble nucleation and growth in andesitic magmas. Lithos 296-299, p. 532-546. doi: 10.1016/j.lithos.2017.11.024

Polacci, M., Papale, P. and Rosi, M. 2001. Textural heterogeneities in pumices from the climactic eruption of Mount Pinatubo, 15 June 1991, and implications for magma ascent dynamics. Bull Volcanol 63, p. 83-97. doi: 10. I007/s004450000123

Polacci, M., Pioli, L. and Rosi, M. 2003. The Plinian phase of the Campanian Ignimbrite eruption (Phlegrean Fields, Italy): evidence from density measurements and textural characterization of pumice. Bull Volcanol 65, p.418–432. doi: 10.1007/s00445-002-0268-4

Prousevitch, A.A., Sahagian, D.L., and Anderson, A.T. 1993. Dynamics of diffusive bubble growth in magmas: isothermal case. Journal of Geophysical Research: Solid Earth, 98 (B12), 22283-22307. doi: 10.1029/93JB02027

Rosi, M., Landi, P., Polacci, M., Di Muro, A. and Zandomeneghi, D. 2004. Role of conduit shear on ascent of the crystal-rich magma feeding the 800-year-B.P. Plinian eruption of Quilotoa Volcano (Ecuador). Bull Volcanol 66, p. 307-321. doi: 10.1007/s00445-003-0312-z

Rotella, M.D., Wilson, C.J.N., Barker, S.J., Cashman, K.V., Houghton, B.F. and Wright, I.C. 2014. Bubble development in explosive silicic eruptions: insights from pyroclast vesicularity textures from Raoul volcano (Kermadec arc). Bull Volcanol 76:826. doi: 10.1007/s00445-014-0826-6

Rotella, M.D., Wilson, C.J.N., Barker, S.J., Schipper, C.I., Wright, I.C. and Wysoczanski, R.J. 2015. Dynamics of deep submarine silicic explosive eruptions in the Kermadec arc, as reflected in pumice vesicularity textures. Journal of Volcanology and Geothermal Research 301, p. 314-332. doi: 10.1016/j.jvolgeores.2015.05.021

Rust, A. C. and Cashman, K. V. 2004. Permeability of vesicular silicic magma: inertial and hysteresis effects. Earth and Planetary Science Letters 228, p. 93-107. doi: 10.1016/j.epsl.2004.09.025

Rutherford, M.J. and Devine, J.D. 1996. Preeruption Pressure-Temperature Conditions and Volatiles in the 1991 Dacitic Magma of Mount Pinatubo. In: Newhall, C.G., Punongbayan, R.S. (eds.). 1996. Fire and Mud. Eruptions and Lahars of Mount Pinatubo, Philippines. University of Washington Press, Seattle, pp. 751-766.

Rutherford, M.J. 2008. Magma ascent rates. Reviews in Mineralogy and Geochemistry 69, 241-271. doi: 10.2138/rmg.2008.69.7

Ryan, A. G., Russell, J. K., Hess, K.-U., Phillion, A. B. and Dingwell, D. B. 2015. Vesiculation in rhyolite at low H2O contents: A thermodynamic model. Geochemistry, Geophysics, Geosystems 16, p. 4292-4310. doi: 10.1002/2015GC006024

Ryan, A.G., Russell, J.K., Heap, M.J., Kolzenburg, S., Vona, A. and Kushnir, A.R.L. 2019. Strain‐dependent rheology of silicate melt foams: Importance for outgassing of silicic lavas. Journal of Geophysical Research: Solid Earth 124, 8167-8186. doi: 10.1029/2019JB018099

Saar, M.O., Manga, M., Cashman, K.V., and Fremouw, S. 2001. Numerical models of the onset of yield strength in crystal-melt suspensions. Earth and Planetary Science Letters 187, 367-379. doi: 10.1016/S0012-821X(01)00289 -8.

Sæmundsson, K. 2008. Geological map of Krafla: Reykjavik, National Power Company (Landsvikjun) and Iceland GeoSurvey (ISOR), scale 1: 25,000.

Scheu, B., Spieler, O. and Dingwell, D.B. 2006. Dynamics of explosive volcanism at Unzen volcano: an experimental contribution. Bulletin of Volcanology 69, 175-187. doi: 10.1007/s00445-006-0066-5

Scheu, B., Kueppers, U., Mueller, S., Spieler, O. and Dingwell, D.B. 2008. Experimental volcanology on eruptive products of Unzen volcano. Journal of Volcanology and Geothermal Research 175 (1-2), 110-119. doi: 10.1016/j.jvolgeores.2008.03.023

Schipper, C.I., Castro, J.M., Tuffen, H., James, M.R. and How, P. 2013. Shallow vent architecture during hybrid explosive–effusive activity at Cordón Caulle (Chile, 2011–12): evidence from direct observations and pyroclast textures. Journal of Volcanology and Geothermal Research 262, 25-37. doi: 10.1016/j.jvolgeores.2013.06.005

Schlinger, C. M., Rosenbaum, J. G., Veblen, D. R., 1988. Fe-oxide microcrystals in welded tuff from southern Nevada: Origin of remanence carriers by precipitation in volcanic glass. Geology 16 (6), p. 556-559. doi: 10.1130/0091-7613(1988)016<0556:FOMIWT>2.3.CO;2

Seifert, F., Mysen, B. and Virgo, D. 1982. Three-dimensional network structure of quenched melts (glass) in the systems SiO2-NaAlO2, SiO2-CaAl2O4 and SiO2-MgAl2O4. American Mineralogist 67, 696-717.

Self, S. and Rampino, M.R. 1981. The 1883 eruption of Krakatau. Nature 294, 699-704. doi: 10.1038/294699a0

Sharp, T.G., Stevenson, R.J. and Dingwell, D.B. 1996. Microlites and “nanolites” in rhyolitic glass: microstructural and chemical characterization. Bulletin of Volcanology 57, p. 631-640. doi: 10.1007/s004450050116

Shea, T., Houghton, B.F., Gurioli, L., Cashman, K.V., Hammer, J.E. and Hobden, B.J. 2010a. Textural studies of vesicles in volcanic rocks: An integrated methodology. Journal of Volcanology and Geothermal Research 190, p. 271-289. doi: 10.1016/j.jvolgeores.2009.12.003

Shea, T., Gurioli, L., Larsen, J.F., Houghton, B.F., Hammer, J.E. and Cashman, K.V. 2010b. Linking experimental and natural vesicle textures in Vesuvius 79AD white pumice. Journal of Volcanology and Geothermal Research 192, p. 69-84. doi: 10.1016/j.jvolgeores.2010.02.013

Shea, T., Gurioli, L. and Houghton, B.F. 2012.Transitions between fall phases and pyroclastic density currents during the AD 79 eruption at Vesuvius: building a transient conduit model from the textural and volatile record. Bull Volcanol 74, p. 2363-2381. doi: 10.1007/s00445-012-0668-z

Shea, T. 2017. Bubble nucleation in magmas: A dominantly heterogeneous process? Journal of Volcanology and Geothermal Research 343, p. 155-170. doi: 10.1016/j.jvolgeores.2017.06.025

Sigurdsson, H. and Sparks, R.S.J. 1981. Petrology of Rhyolitic and Mixed Magma Ejecta from the 1875 Eruption of Askja, Iceland. Journal of Petrology 22 (Part l), p. 41-84. doi: 10.1093/petrology/22.1.41

Singer, B.S., Hildreth, W. and Vincze, Y. 2000. 40Ar/39Ar evidence for early deglaciation of the central Chilean Andes. Geophysical Research Letters 27, 1663-1666. doi: 10.1029/1999GL011065

Sparks, R.S.J. 1978. The dynamics of bubble formation and growth in magmas: a review and analysis. Journal of Volcanology and Geothermal Research 3, p. 1-37. doi: 10.1016/0377-0273(78)90002-1

Sparks, R.S.J., Wilson, L. and Sigurdsson, H. 1981. The pyroclastic deposits of the 1875 eruption of Askja, Iceland. Philosophical Transactions of the Royal Society of London. Series A, Mathematical and Physical Sciences 299 (1447), 241-273. doi: 10.1098/rsta.1981.0023

Sparks, R.S.J., Barclay, J., Jaupart, C., Mader, H.M. and Phillips, J.C. 1994. Physical aspects of magma degassing I. Experimental and theoretical constraints on vesiculation. Rev Mineral 30, 413-445.

Spieler, O., Kennedy, B., Kueppers, U., Dingwell, D.B., Scheu, B. and Taddeucci, J. 2004. The fragmentation threshold of pyroclastic rocks. Earth Planetary Science Letters 226 (1-2), 139-148. doi: 10.1016/j.epsl.2004.07.016

Spina, L., Cimarelli, C., Scheu, B., Di Genova, D., and Dingwell, D.B. 2016. On the slow decompressive response of volatile-and crystal-bearing magmas: An analogue experimental investigation. Earth and Planetary Science Letters 433, 44-53. doi: 10.1016/j.epsl.2015.10.029

Stabile, P., Giuli, G., Cicconi, M.R., Paris, E., Trapananti, A. and Behrens, H. 2017. The effect of oxygen fugacity and Na/(Na+K) ratio on iron speciation in pantelleritic glasses. Journal of Non-Crystalline Solids 478 65-74. doi: 10.1016/j.jnoncrysol.2017.09.051

Stewart, A-M. and Castro, J.M. 2016. P–T–X evolution of the 1280 AD Quilotoa dacite. Journal of Volcanology and Geothermal Research 313, p. 29-43. doi: 10.1016/j.jvolgeores.2015.11.024

Stokes, S., Lowe, D.J. and Froggatt, P.C. 1992. Discriminant function analysis and correlation of Late Quaternary rhyolitic tephra deposits from Taupo and Okataina volcanoes, New Zealand, using glass shard major element composition. Quaternary International 13-14, p. 103-117. doi: 10.1016/1040-6182(92)90016-U

Suzuki, Y. and Nakada, S. 2002. Vesiculation and magma ascent process in the Usu 200 eruption, inferred from texture and size distribution of bubble. Bulletin of the Volcanological Society of Japan 47, p. 675-688 (in Japanese with English abstract). doi: 10.18940/kazan.47.5_675

Teplow, W., Marsh, B., Hulen, J., Spielman, P., Kaleeikinin, M., Fitch, D. and Rickard, W. 2009. Dacite Melt at the Puna geothermal venture well field, big Island of Hawaii. Geotherm. Resour. Counc. Trans. 33, 989-994.

Thivet, S., Gurioli, L., Di Muro, A., Derrien, A., Ferrazzini, V., Gouhier, M., Coppola, D., Galle, B. and Arellano, S. 2020. Evidences of plug pressurization enhancing magma fragmentation during the September 2016 basaltic eruption at Piton de la Fournaise (La Réunion Island, France). Geochemistry Geophysics Geosystems 21, e2019GC008611. doi: 10.1029/2019GC008611

Toramaru, A. 1995. Numerical study of nucleation and growth of bubbles in viscous magmas. Journal of Geophysical Research: Solid Earth 100, 1913-1931. doi: 10.1029/94JB02775

Toramaru, A. 2006. BND (bubble number density) decompression rate meter for explosive volcanic eruptions. Journal of Volcanology and Geothermal Research 154, 303-316. doi: 10.1016/j.jvolgeores.2006.03.027

Tuffen, H., Dingwell, D.B. and Pinkerton, H. 2003. Repeated fracture and healing of silicic magma generate flow banding and earthquakes? Geology 31 (12), 1089-1092. doi: 10.1130/G19777.1

Tuffen, H. and Castro, J.M. 2009. The emplacement of an obsidian dyke through thin ice: Hrafntinnuhryggur, Krafla Iceland. Journal of Volcanology and Geothermal Research 185, p. 352-366. doi: 10.1016/j.jvolgeores.2008.10.021

Tuffen, H., James, M.R., Castro, J.M. and Schipper, C.I. 2013. Exceptional mobility of an advancing rhyolitic obsidian flow at Cordón Caulle volcano in Chile. Nature communications, 4, 2709. doi: 10.1038/ncomms3709

Vetere, F., Iezzi, V., Behrens, H., Cavallo, A., Misiti, V., Dietrich, M., Knipping, J., Ventura, G. and Mollo, S. 2013. Chemical Geology 354, 233-242. doi: 10.1016/j.chemgeo.2013.06.007

von Aulock, F.W., Kennedy, B.M., Maksimenko, A., Wadsworth, F.B. and Lavallée, Y. 2017 Outgassing from Open and Closed Magma Foams. Front. Earth Sci. 5:46. doi: 10.3389/feart.2017.0004

Wadsworth, F.B., Vasseur, J., Scheu, B., Kendrick, J.E., Lavallée, Y. and Dingwell, D.B. 2016. Universal scaling of fluid permeability during volcanic welding and sed-iment diagenesis. Geology 44, p. 219-222. doi: 10.1130/G37559.1

Walsh, S.D., and Saar, M.O. 2008. Magma yield stress and permeability: Insights from multiphase percolation theory. Journal of Volcanology and Geothermal Research 177, 1011-1019. doi: 10.1016/j.jvolgeores.2008.07.009

Wallace, P.J., Anderson, A.T.Jr. and Davis, A.M. 1995. Quantification of pre-eruptive exsolved gas contents in silicic magmas. Nature 377, 612-616. doi: 10.1038/377612a0

Wallace, P.J., Plank, T., Edmond, M. and Hauri, E.H. 2015. Volatiles in Magmas. *In: The Encyclopedia of Volcanoes (Second Edition)*. p. 163-183. doi: 10.1016/B978-0-12-385938-9.00007-9

Warshaw, C.M. and Smith, R.L. 1988. Pyroxenes and fayalites in the Bandelier Tuff, New Mexico: Temperatures and comparison with other rhyolites. American Mineralogist 73, 1025-1037.

Watt, S.F., Pyle, D.M., Mather, T.A., Martin, R.S. and Matthews, N.E. 2009. Fallout and distribution of volcanic ash over Argentina following the May 2008 explosive eruption of Chaitén, Chile. Journal of Geophysical Research: Solid Earth 114 (B04207). doi: 10.1029/2008JB006219

Webb, S.L. and Dingwell, D.B. 1990. Non-Newtonian rheology of igneous melts at high stresses and strain rates: experimental results for rhyolite, andesite, basalt and nephelinite. Journal of Geophysical Research 95 (B10), 15695-15701. doi: 10.1029/JB095iB10p15695

Wespestad, C.E., Thurber, C.H., Andersen, N.L., Singer, B.S., Cardona, C., Zeng, X., Bennington, N.L., Keranen, K., Peterson, D.E., Cordell, D., Unsworth, M., Miller, C., Williams-Jones, G. 2019. Magma reservoir below Laguna del Maule volcanic field, Chile, imaged with surface-wave tomography. Journal of Geophysical Research: Solid Earth 124, 2858-2872. doi: 10.1029/2018JB016485

Williams, S.N. and Self, S. 1983. The October 1902 plinian eruption of Santa Maria volcano, Guatemala. Journal of Volcanology and Geothermal Research 16 (1-2), 33-56. doi: 10.1016/0377-0273(83)90083-5

Xu, Z. and Zhang, Y. 2002. Quench rates in air, water, and liquid nitrogen, and inference of temperature in volcanic eruption columns. Earth and Planetary Science Letters 200, 315-330. doi: 10.1016/S0012-821X(02)00656-8

Zellmer, G.F., Sakamoto, N., Hwang, S-L., Matsuda, N., Iizuka, Y., Moebis, A. and Yurimoto, H. 2016. Inferring the Effects of Compositional Boundary Layerson Crystal Nucleation, Growth Textures, and Mineral Chemistry in Natural Volcanic Tephras through Submicron-Resolution Imaging. Front. Earth Sci. 4:88. doi: 10.3389/feart.2016.00088

Zierenberg, R.A., Schiffman, P., Barfod, G.H., Lesher, C.E., Marks, N.E., Lowenstern, J.B., Mortensen, A.K., Pope, E.C., Fridleifsson, G.Ó. and Elders, W.A. 2012. Composition and origin of rhyolite melt intersected by drilling in the Krafla geothermal field, Iceland. Contributions to Mineralogy and Petrology 165, 327-347. doi: 10.1007/s00410-012-0811-z

Zhang, Y. 1999. H2O in rhyolitic glasses and melts: measurement, speciation, solubility, and diffusion. Reviews of Geophysics 37 (4), 493-516. doi: 10.1029/1999RG900012

Zhang, Y. and Ni, H. 2010. Diffusion of H, C, and O Components in Silicate Melts. Reviews in Mineralogy and Geochemistry 72, 171-225. doi:10.2138/rmg.2010.72.5